



HZDR



**Study of the Static and Dynamic Magnetization
across the First Order Phase Transition in FeRh
Thin Films**

DISSERTATION

zur Erlangung des akademischen Grades

Doctor of Philosophy

(Ph. D.)

vorgelegt der Fakultät

Mathematik und Naturwissenschaften
der Technische Universität Dresden

Von Alireza Heidarian

geboren am 20.01.1981 in Kermanshah, Iran

Supervisor: Prof. Dr. Jürgen Faßbender

Dresden, 2015

GUTACHTER:

Prof. Dr. Jürgen Faßbender

Prof. Dr. Thomas Thomson

Eingereicht am: 10.11.2015

Tag der Verteidigung: 22.01.2016

This dissertation is dedicated to my brilliant and
outrageously loving and supportive wife,
Mahda

Abstract

The equiatomic FeRh alloy undergoes a first-order phase transition from an antiferromagnetic (AFM) to a ferromagnetic (FM) state at about 370 K with a small thermal hysteresis of about 10 K around the phase transition. The transition is accompanied by a unit cell volume expansion about 1% in the c lattice parameter. During the transition the new phase nucleates in the matrix of the original phase by reaching the critical temperature followed by a growth in size upon increasing temperature further. Therefore, to understand the transition process with more details, it is desirable to investigate the nucleation and growth of both phases within the first order phase transition.

In the present thesis the main focus is on the growth of FeRh thin films by means of Molecular Beam Epitaxy (MBE) technique and characterization of the magnetic and structural properties. To develop an understanding of the phase transformation in FeRh thin films the ways in which one can tune it were investigated. The following aspects concerning the FeRh system have been examined here: 1) influence of annealing temperature on the magnetic and structural response, 2) effect of film thickness on the first-order phase transition temperature as well as the saturation magnetization, 3) influence of chemical composition on the magnetic properties and 4) magnetic field-induced phase transition.

To get insight to details of the transition process the magnetization dynamic has been addressed by performing Ferromagnetic resonance (FMR) experiment across the phase transition. FMR measurements determined the existence of two areas with different magnetic properties inside the film. A huge temperature difference for the beginning of the phase transition in comparison with the static magnetization measurement was observed for the equiatomic FeRh thin film prepared by MBE.

Tuning of the AFM to FM phase transition in the FeRh thin film by means of low-energy/low fluence Ne^+ ion irradiation was studied. Ion irradiation technique offers a quantitative control of the degree of chemical disorder by adjusting the ion fluence applied, while the penetration depth of the disordered phase can be adjusted by the ion-energy. The main results of ion irradiation are the shifting of the phase transition temperature to lower temperature and irradiation with 3×10^{14} ion/cm² leads to the disappearance the AFM phase completely.

Contents

| | |
|---|-----------|
| Abstract | i |
| 1 Introduction and Motivation | 1 |
| 1.1 Magnetic phase transition in the FeRh alloy | 1 |
| 1.1.1 Origin of the magnetic phase transition | 5 |
| 1.2 Tuning the FeRh phase transition | 9 |
| 1.2.1 Growth condition dependence | 9 |
| 1.2.2 Effect of strain | 11 |
| 1.2.3 Influence of chemical disordering | 13 |
| 1.2.4 Chemical composition dependence | 15 |
| 1.2.5 Effect of applied magnetic field | 18 |
| 1.3 Application potential | 21 |
| 1.3.1 Heat Assisted Magnetic Recording | 21 |
| Bibliography | 25 |
| 2 Experimental Techniques | 33 |
| 2.1 Thin film growth techniques | 33 |
| 2.1.1 Molecular Beam Epitaxy | 33 |
| 2.1.2 Sputtering | 37 |
| 2.2 Preparation of FeRh thin films | 37 |
| 2.3 Ion irradiation | 39 |
| 2.4 Compositional Characterization | 42 |
| 2.4.1 Rutherford Backscattering Spectrometry | 42 |
| 2.4.2 Auger Electron Spectroscopy | 43 |
| 2.5 Structural Characterization | 45 |
| 2.5.1 X-ray diffraction | 45 |

| | | |
|---------------------------------|--|------------|
| 2.5.2 | X-ray Reflectivity | 46 |
| 2.6 | Magnetic characterization | 48 |
| 2.6.1 | SQUID-magnetometer | 48 |
| 2.6.2 | Ferromagnetic Resonance | 51 |
| Bibliography | | 57 |
| 3 Results and discussion | | 61 |
| 3.1 | FeRh phase transition | 61 |
| 3.1.1 | Influence of annealing temperature | 61 |
| 3.1.2 | Thickness-dependence | 66 |
| 3.1.3 | Effect of chemical composition | 72 |
| 3.1.4 | Magnetic field dependence | 75 |
| 3.2 | Ferromagnetic resonance | 77 |
| 3.2.1 | FMR study of FeRh thin film | 79 |
| 3.2.2 | Influence of thickness | 87 |
| 3.2.3 | Comparison of the growth techniques | 90 |
| 3.3 | Ion irradiation | 94 |
| 3.3.1 | Sample preparation and characterization | 94 |
| 3.3.2 | Tailoring the magnetism of FeRh thin films | 95 |
| 3.3.3 | Effect of post irradiation annealing | 101 |
| Bibliography | | 105 |
| 4 Summary and outlook | | 109 |
| Publications | | 113 |
| Acknowledgments | | 115 |

Chapter 1

Introduction and Motivation

FeRh was first reported in 1938 by M. Fallot [1] who showed that this alloy, with the B2(CsCl-type) cubic structure at near-equiatomic compositions, undergoes an abrupt first-order phase transition at approximately 370 K [1, 2, 3, 4, 5]. After that, many attempts were made in order to understand the temperature-induced metamagnetic transition and the magnetic properties of ordered FeRh system. In this chapter, the magnetic properties of FeRh alloy are first described. Then the effective parameters on the first order phase transition are introduced and finally it will be highlighted why FeRh thin films are scientifically interesting as well as an outstanding candidate for heat-assisted magnetic recording (HAMR).

1.1 Magnetic phase transition in the FeRh alloy

This section describes the general features related to the AFM to FM phase transitions in FeRh thin films and it is followed by an overview of the magnetic and structural properties of the FeRh transformation. This is followed by a description of thin film forms of FeRh and the anomalous features which may appear in these systems. After that the origin of the magnetic phase transition will be discussed. In section 1.2 particular attention will be given to describe factors which may modify the FeRh phase transition properties and finally in section 1.3 an application of FeRh alloy will be introduced. The FeRh unit cell has a chemically-ordered CsCl-type (α') phase in which the Fe atoms sits at the corners of the cubic unit cell while Rh sits in the central location (see Fig. 1.1).

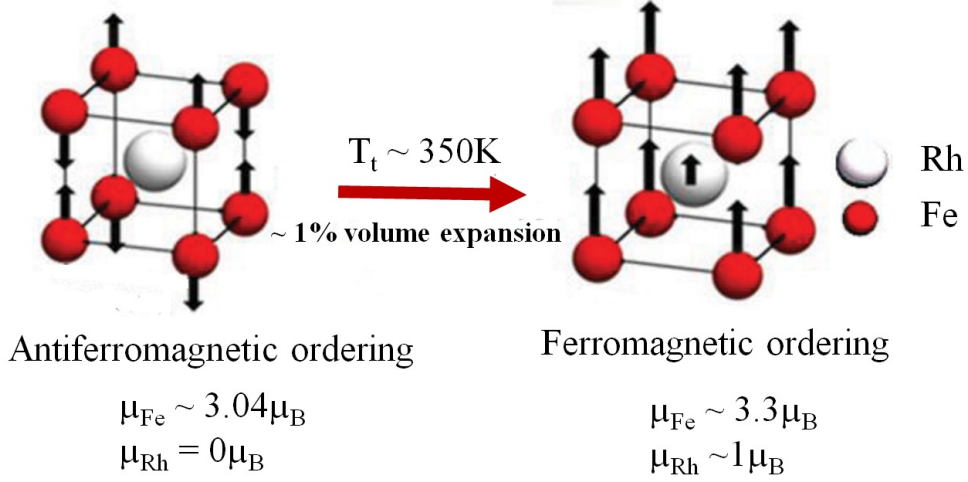


Figure 1.1: *Spin configurations of FeRh: (a) Type-II AFM, (b) FM* [6].

Since the original work of Fallot, several reports have shown that FeRh alloy undergoes a first-order magnetic transition from AF to FM order, with increasing temperature [3, 4, 5]; as the temperature is further increased to a temperature above the Curie temperature (T_C) the FeRh system undergoes a second-order, FM-PM transition [7, 8]. Fig. 1.2 shows the magnetic transition from AF to FM and FM to PM order for FeRh system. By increasing temperature, the AFM-FM transformation is indicated by an abrupt increase in the magnetization from 0 to 1100 emu/cm^3 ($H_{\text{app}} = 5 \text{ kOe}$) at $T_{tr} \sim 350 \text{ K}$ while the FM-PM transition is indicated by a slow decrease in the magnetization from 1100 emu/cm^3 to 0 at $T_C \sim 700 \text{ K}$ [3]. The AFM-FM transformation FeRh alloy is accompanied by a thermal hysteresis loop of approximately 10 K, upon cooling from the FM phase, in the vicinity of the transition [7, 9], and correlated with expansion in the unit cell [10, 11].

Further, element specific studies of the magnetic moments associated with the Fe and Rh atoms have shown that in the FM state both Fe and Rh atoms have a magnetic moment while in the AFM there is a magnetic moment of $0 \mu_B$ per Rh atom [5, 12, 13]. The antiferromagnetic ordering is type-II (see Fig. 1.1); in this configuration the coupling of both the intra- and inter-plane moments are antiferromagnetic. The simultaneous to magnetic transformation volume expansion of the unit cell is signaled by a shift in the Bragg reflections of the XRD pattern to lower 2θ values corresponds to an increase of the unit cell lattice parameter

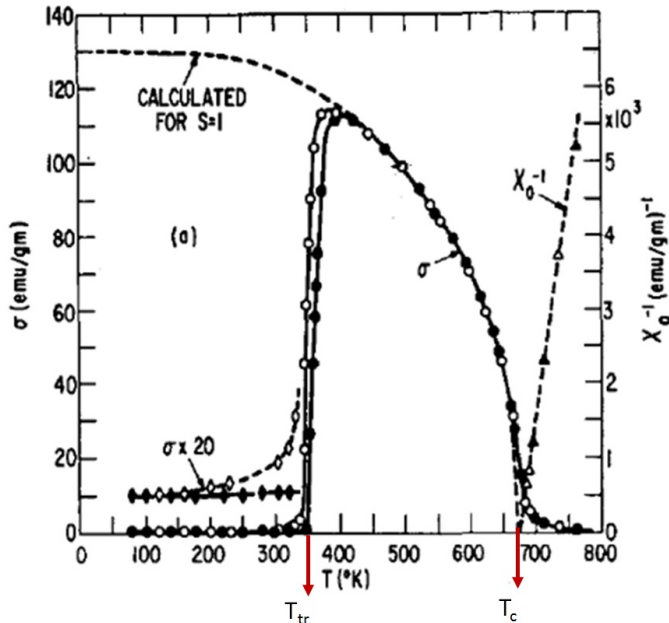


Figure 1.2: First- and second-order magnetic phase transitions from AFM to FM order at T_{tr} and FM to PM order at T_c for FeRh alloy ($H_{app} = 5$ kOe) [3].

values. Fig. 1.1 shows the magnetic structure of AFM and FM phases of FeRh unit cell which the lattice parameter changes from 0.2980 to 0.2998 nm as the unit cell volume expands about 1% at the critical transition temperature.

Thin films of FeRh display magnetic and structural features which are consistent with bulk FeRh (i.e. an AFM-FM transformation with an accompanying lattice expansion), upon heating. But, the mismatch between epitaxial film and substrate creates an anisotropic strain which leads to significant variations in the transition properties of FeRh thin films, relative to bulk FeRh [14, 15, 16]. Specifically, it may result in a structural transformation which is constrained in the in-plane (lateral) direction, relative to the isotropic expansion of bulk FeRh [17, 18, 19]. The unit cell expansion helps to stabilize the FM phase. Moreover, FeRh thin films often display a remnant FM phase in the AF regime. The location and origin of the residual FM phase has not been understood completely, however, R. Fan, et al have attributed the retained FM layer to compositional, fluctuations or strain at the film interfaces [14]. After observing the first and second order phase transitions many attempts have been made in order to un-

derstand the temperature-induced metamagnetic transition and the magnetic properties of FeRh system [7, 20, 21, 22]. The element specific studies of the magnetic moments associated with the Fe and Rh atoms have shown that FeRh in the FM state has a magnetic moment of $3.04 \mu_B$ per Fe atom and $\sim 1 \mu_B$ per Rh atom [6]. At room temperature, in the AFM state, FeRh has zero net magnetic moment; the magnetic moments associated with the Fe atoms are antiferromagnetically ordered with magnetic moments of $\pm 3.3 \mu_B$ per Fe atom while there is a magnetic moment of $0 \mu_B$ per Rh atom. Moruzzi et al. [12] showed that the ground state of equiatomic FeRh - AFM or FM - strongly depends on the unit cell structure. Fig. 1.3(a) shows the magnetic moment of FeRh in the AFM and FM phase as a function of lattice parameters. The average energy difference per atom between the FM and AFM phase is shown in Fig. 1.3(b) and as is visible it decreases by increasing the lattice constant. The energy difference changes sign at about 3.096 \AA . Generally, the FeRh film lattice constant is about 3.0 \AA in AFM phase that is ground state in this system. Small changes of the external parameters, such as magnetic field, pressure or temperature, can lead to the phase transition of FeRh from AFM to FM [23]. The DFT calculations show a strong hybridization between Fe and Rh atoms in the FeRh system in the FM state. The influence of this hybridization is inducing Rh moment by Fe atoms.

It has been established that in the FM phase Fe-Rh and in the AFM phase Fe-Fe interaction depend on the unit cell volume variation. Therefore, the Fe-Fe interaction in the AFM state has main role on the magnetic phase transition of FeRh system. This interaction can be changed by extrinsic parameters such as: volume (lattice constant), strain etc. Due to the small energy difference between AFM and FM phase the first order phase transition and consequently, the magnetic properties of the FeRh thin films can be strongly affected by changing the extrinsic parameters.

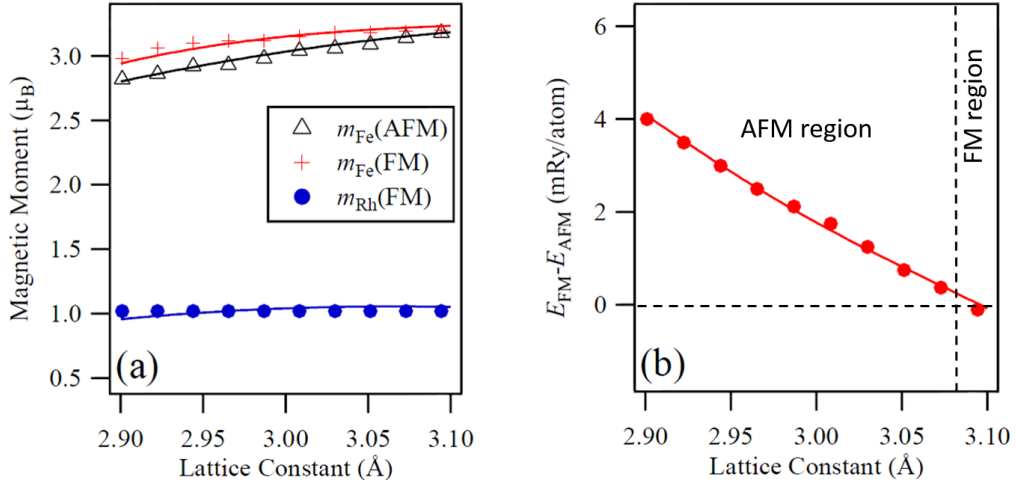


Figure 1.3: (a) Magnetic moment and (b) the energy difference between FM and AFM as a function of lattice constant [24]. The results obtained by using DFT calculation [12].

1.1.1 Origin of the magnetic phase transition

In a thermodynamic system, the basic parameters contain macroscopic properties, such as Gibbs free energy (G), pressure (P), temperature (T) and enthalpy (H). The thermodynamic theory is discussed here by using reference [25]. The transformation from one thermodynamic system to another system is defined by phase transition. The Gibbs free energy of a system is given as a function of temperature and pressure:

$$G(T, P) = U + PV - TS \quad (1.1)$$

U is the internal energy of the system (J), P is the pressure of the system (N/m^2), V is the volume of the system (m^3), T is the temperature of the system (K) and S is the entropy of the system (J/K). Note, that the entropy term in Equation 1.1 is the total entropy arising from magnetic contributions, electronic contributions and lattice vibrations. The stability of the system can be determined by the Gibbs free energy (G) at a constant temperature and pressure. The phase stability and equilibrium conditions are expressed in the context of

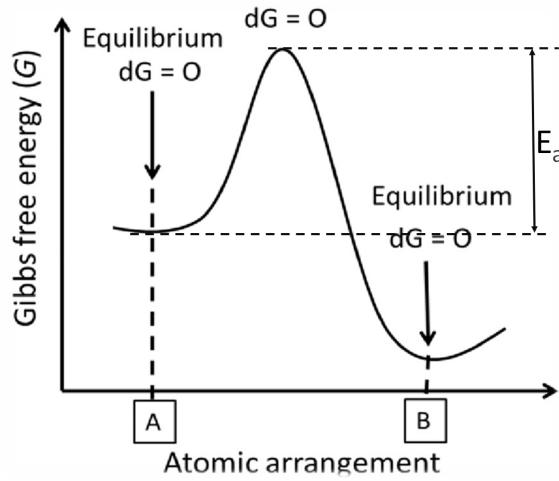


Figure 1.4: Image shows the relative stability of a system transfers from state A to state B. The minimum of the free energy function is stable regions at which the system is at equilibrium. Figure adapted from [25].

minima and maxima of the Gibb's free energy function in mathematical terms:

$$dG = 0 \quad (1.2)$$

By varying some parameters in the system such as temperature or pressure the random motion of the atoms can provide enough energy for the system to transfer from a stable state to a metastable state. In this case, the first derivative of the free energy function described in Equation 1.1 can defined the relative stability of a system. The representative plot of a free energy function is shown in Fig. 1.4 graphically. Configuration A is a metastable equilibrium at a local minima in the free energy. Configuration B has the lowest free energy so that by small changes in the arrangement of atoms to a first approximation produces G does not change. Thermodynamically, any phase transition that leads to decrease in Gibbs free energy is possible. Therefore, a necessary condition for phase transition is:

$$\Delta G = G_2 - G_1 < 0 \quad (1.3)$$

Where, G_1 and G_2 are the free energies of the initial and final states, respectively. For a phase transition to proceed the transforming phase it is necessary to

overcome an initial energy barrier, ie. activation energy (E_a), that is the energy separating two equilibrium states (Fig. 1.4). The thermally activated state can be provide through the random thermal motion of the atoms in a system. For a phase transition the energy barrier is vital parameter to predict the overall transformation properties in a system.

In magnetic materials systems, additional energy terms could be added to the Equation 1.1 such as applied magnetic field due to the existence of additional contributions. Change in G in a magnetic material system during the phase transformation is given by [26]:

$$dG = -SdT + VdP - MdH \quad (1.4)$$

Where M is the magnetization of the system (Am^{-1}) and H is the external applied magnetic field (T). The first-order magnetic transitions display a discontinuity in magnetization (M) at the phase transition temperature add to a discontinuity in volume and entropy.

In general, first-order phase transition is not a single step process. It typically proceeds through the nucleation and growth of a product phase from an initial phase. Characteristically nucleation defines the formation of a thermodynamic phase which is separate from the initial phase. Nucleation can proceed either when nuclei form randomly throughout the system or nuclei form at the interfaces or at defects. Growth of a secondary phase can occur simultaneously during phase nucleation or after the nucleation process is completed.

For the FeRh system first proposed explanation of the magnetic phase transition was made in the context of an exchange inversion theory [27]. In this theory, it is suggested that the thermal expansion of the FeRh crystal lattice causes a change in the sign of the Fe-Fe interaction, subsequently, driving the AFM-FM transformation. This theory has been disproved based on inconsistencies between the total entropy of the transformation and the change in the lattice entropy of the transformation [20]. Other theories suggest that electronic differences in the density of states- which is the concentration of energy levels within the valence band -as the primary driving force for the transformation [21]. A more recently proposed theory suggests that the emergence of a magnetic moment on the Rh moment plays a key role in the stabilization of the

FM phase. Specifically, Gruner et al. suggested that the transformation may be driven by competing magnetic states of the Rh atom, which is known to have 0 or $\sim 1 \mu_B$ (dependent on the magnetic order of the system) [28]. Thermal analysis studies have been useful in experimentally validating the results shown by Ricodeau and Meville [20]. In particular, Cooke et al [22] measured the specific heat, associated with the AFM-FM transformation, in 200 nm thick $\text{Fe}_{0.98}\text{Rh}_{0.02}$ films grown on IBAD MgO by incorporating thermocouples onto the FeRh film surface. Despite the thickness of this film the FeRh system is still compressively strained by the substrate [29]. From these measurements, Cooke et al. determined that magnetic fluctuations likely play the largest role driving the AFM-FM transformation. While electronic contributions provide a smaller contribution and lattice vibrations which stabilize the AF phase relative to the FM phase [22].

Moreover, the idea that magnetic fluctuations are the primary driving factor for the transformation is consistent with time resolved XRD and magneto optical Kerr microscopy (MOKE) experiments. As a result, lattice expansion occurs after than the onset of FM in the AFM-FM transformation. Alternatively, X-ray magnetic circular dichroism (XMCD) measurements have recently indicated that both antiferromagnetic and ferromagnetic states can coexist in the 50 nm single-crystalline FeRh thin films on MgO(100) [30]. Photoemission electron microscopy (PEEM) measurements also confirm the coexistence of both AF and FM phase in 90 nm single-crystalline FeRh thin fillm on MgO with a 2.5 nm Al capping layer [31]. The PEEM measurements also reveal that ferromagnetic domain nucleation and formation can be tuning by temperature. Moreover, vibrating sample magnetometry (VSM) measurement for in plane and out-of-plane magnetic hysteresis loops of a 150 nm single-crystalline FeRh thin film on MgO(100) show stress-induced magnetic anisotropy in FeRh thin films during first-order phase transition [32]. Additionally, ^{57}Fe conversion electron mös-bauer spectroscopy (CEMS) measurements of single-crystalline FeRh thin film on MgO additionally indicate an Fe spin reorientation from out-of-plane to in-plane or inverse during the first-order phase transition which is characterized by the stress introduced at the FeRh/substrate interface [33].

1.2 Tuning the FeRh phase transition

It has been known in FeRh systems that the first-order magnetic phase transition is very sensitive to variations in material combination [20, 14, 15], FeRh composition [8], applied magnetic field and strain [34, 35]. The following section describes modifications in the magnetic phase transition of bulk and thin film of FeRh samples, specifically: growth condition (Section 1.2.1), strain and pressure (Section 1.2.2), chemical disordering (Section 1.2.3), chemical composition (stoichiometry) (Section 1.2.4), and magnetic field (Section 1.2.5).

1.2.1 Growth condition dependence

The general overview of the effect of film growth conditions on the FeRh magnetic and structural phase transition properties is discussed in this section. Lommel in 1966 studied three separate methods for FeRh thin film deposition: 1) sputter deposition; 2) codeposition of Fe from an alumina crucible and Rh from the electron gun source; and 3) alternate Fe and Rh layer deposition by electron beam melting [14]. Lommel confirmed that FeRh grown by the deposition of alternating layers of Fe and Rh shows a broad AFM-FM transition. A broad thermal hysteresis also was observed accompanied by phase transition; the other deposition methods (1) and (2) displayed slight or no indication of a magnetic phase transition. The as grown sample does not have CsCl-type structure-order unit cell [36].

In addition to Lommel's results, it has been established that other parameters such as annealing temperature [15] and film growth atmosphere [13], are essential factors which can effect the sharpness of the magnetic AFM-FM transformation, chemical-order, and accompanying. In this report, Lommel showed that annealing in a O₂ atmosphere improves the phase transition while annealing in dry H₂ atmosphere creates only a partial phase transition [13]. In order to produce CsCl-type structure-order in FeRh system and abruptness of the AFM-FM transition, annealing at higher than 600 °C temperature is necessary [37]. The influence of annealing temperature on the phase transition temperature for a FeRh thin film with 150 nm thickness grown in vacuum on (001)-MgO substrate is shown in Fig. 1.5. In general annealing at ($T > 600^{\circ}\text{C}$) creates a

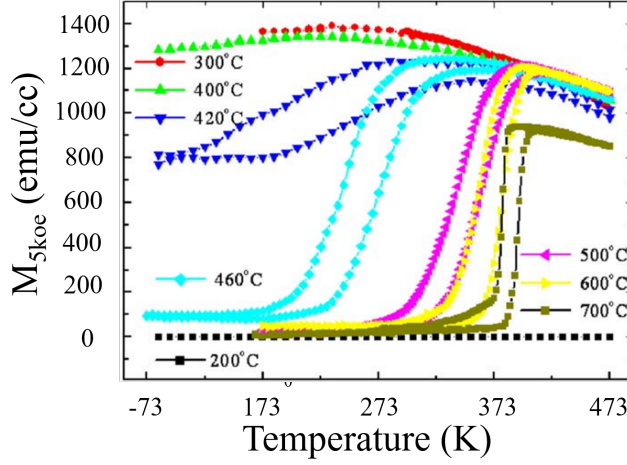


Figure 1.5: Magnetization as a function of temperature of FeRh thin films grown on (001)-MgO. Thin Films were annealed at varied temperatures from 200 °C -700 °C. Abrupt AFM-FM transition take places at $T > 600^{\circ}\text{C}$ [38].

abrupt AFM-FM transition; by reducing the annealing temperature the phase transition becomes broader and also shifts to a lower T_{tr} and finally disappears. For the sample that was annealed at low temperature ($T < 400^{\circ}\text{C}$) because of formation of fcc unit cell structure and a poor chemical-ordering, T_{tr} disappears [38]. Fig. 1.6 shows that for an FeRh thin film grown on (001)-MgO substrate by increasing film thickness over 10 nm or reducing growth temperature the coverage ratio increases. The amount of adsorbed material can be introduced as surface coverage i.e. the fraction of occupied/available sites. Due to the difference between surface energy of the FeRh and MgO layers for samples with thickness (< 10 nm), discrete islands are formed which coalesce for samples with larger thicknesses [39]. In comparison, deposition of FeRh onto a substrate at $T \sim 400^{\circ}\text{C}$ (growth temperature) has a higher degree of chemical-ordering and an abrupt AFM-FM phase transition with respect to the FeRh thin film which was deposited at room temperature [41]. On the other hand, density of the film at high annealing temperatures or low surface coverage may also affect the cohesion of the film layer. Additionally, in this thesis the influence of FeRh thin film thickness on the AFM-FM phase T_{tr} will be systematically investigated specifically for equiatomic FeRh thin films with thickness below 10 nm which has been considered as the critical thickness.

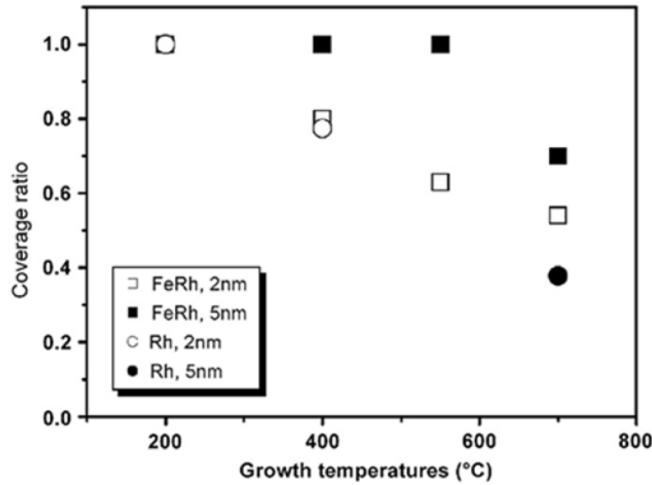


Figure 1.6: *FeRh* and *Rh* film coverage ratio on an (001)-*MgO* substrate as a function of growth temperatures [39]. The coverage ratio defines as the fraction of occupied/available sites.

1.2.2 Effect of strain

The influence of strain on the magnetostructural response in *FeRh* thin films has been investigated before and after delamination [35]. In this research, it is established that strain made by epitaxial growth of *FeRh* thin film can adjust the phase transition temperature.

There are two typical methods to adjust strain in a thin film. First growing the films on substrates with different degrees of lattice mismatch and second to grow films with different thicknesses on the substrate. Comparing the effect of strain induced from grown thin films on *MgO* and *Al₂O₃* substrates reveals that: although the *Al₂O₃* substrates strain is equivalent in magnitude to the strain from *MgO*, makes an opposite shift in the direction of T_{tr} . Opposing to the results reported for bulk pressure studies on *FeRh* samples [40]. For example, the deposition of *FeRh* thin films of varied thicknesses to *MgO* substrate induce a compressive strain which leads to reduction of T_{tr} (see Fig. 1.7(a)). Conversely, *FeRh* films grown epitaxially on *Al₂O₃* substrates show an increase of the transition temperature (Fig. 1.7 (b)) [42]. In *FeRh* thin films, surface strain is supposed to support stabilization of a retained ferromagnetic phase

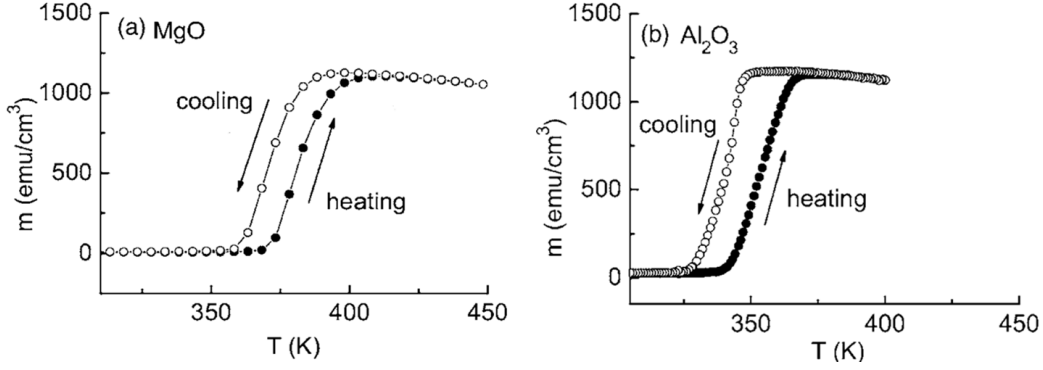


Figure 1.7: Temperature-dependant magnetization behavior of 110 nm thick FeRh films grown on: (a) MgO (001) substrate and (b) Al₂O₃ (0001) substrate [42].

below the magnetic phase transition temperature [13]. It has been reported by Loving et al. that by preparing FeRh thin films with thicknesses below 10 nm, the topography of the surface displays forming of separated islands morphology. This is depicted in Fig. 1.8(a) [43]. The magnetization as a function of temperature for ultrathin FeRh film of thickness 10 nm is shown in Fig. 1.8(b). The phase transition temperature is about 250 K for 10 nm thick FeRh film.

Fig. 1.8(b) shows that for 10 nm film the cooling branch is considerably broader than of the FeRh films with more thickness as shown in Fig. 1.7, which cause to an overall decrease in the sharpness of the phase transition and increase in the thermal hysteresis (ΔT_{tr}) about 100 K of the sample. On the other hand, a large residual magnetization of ~ 855 emu/cm³ observed in the 10 nm thick film in comparison with a small residual magnetism observed in the thick film. The crystallographic alignment of the nano-islands in FeRh thin films have key role in this unusual properties of nano-islands magnetic and structural character. It includes a gradient of lattice constants according to a non-magnetic shell encircled by a ferromagnetic core. In general, these studies determine the effect of strain on the magnetic and structural properties of FeRh thin films.

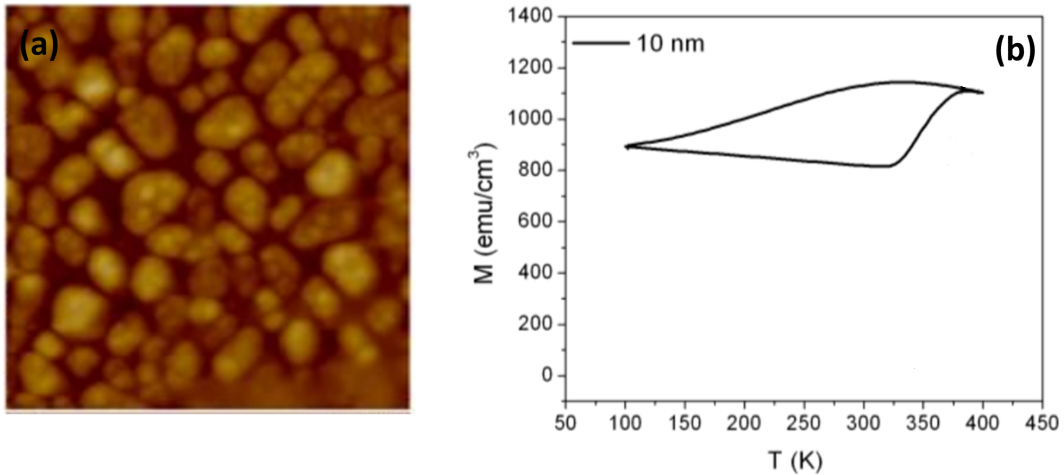


Figure 1.8: *Magnetic and structural properties of ultrathin FeRh films: (a) $1 \times 1 \mu\text{m}$ AFM image of the surface of a FeRh thin film with 10 nm thickness shows a discontinuous island like morphology; (b) Magnetization as a function for temperature of an ultrathin FeRh film of thickness 10 nm thick FeRh film [43].*

1.2.3 Influence of chemical disordering

Binary metallic alloys consisting of a 3d ferromagnetic metal and a non - ferromagnetic alloying element, such as FeAl, FeV and FeRh may show magnetic properties that depend strongly on the degree of their chemical order. In such alloys, varying the degree of chemical order can be a lever to modify the magnetic behavior [44]. In particular, the chemically disordered state, where the atomic site occupancies have been randomized, is metastable.

A good model system to study the disorder induced magnetic phenomena is Fe_xAl_{1-x} with composition around $x=0.6$. In $Fe_{60}Al_{40}$ alloys, the chemically ordered simple cubic B2 (CsCl) phase is paramagnetic while the chemically disordered A2 phase is ferromagnetic. The chemically ordered B2 phase consists of alternating planes of pure Fe and planes consisting of Al and the remaining Fe atoms. As it is shown in Fig. 1.9 the FeAl thin films on the chemically ordered phase is nearly in paramagnetic phase (left), and ferromagnetic on the disordered, A2 phase (right). In this structure the number of nearest neighbor (n-ns) for each atom is 8. In the chemically ordered structure in the pure-Fe planes have on average 1.6 Fe n-ns, and those the Fe atoms in the Al-rich planes have 8 n-ns of Fe with an average of 2.67 Fe-Fe nearest neighbor. In the disorder

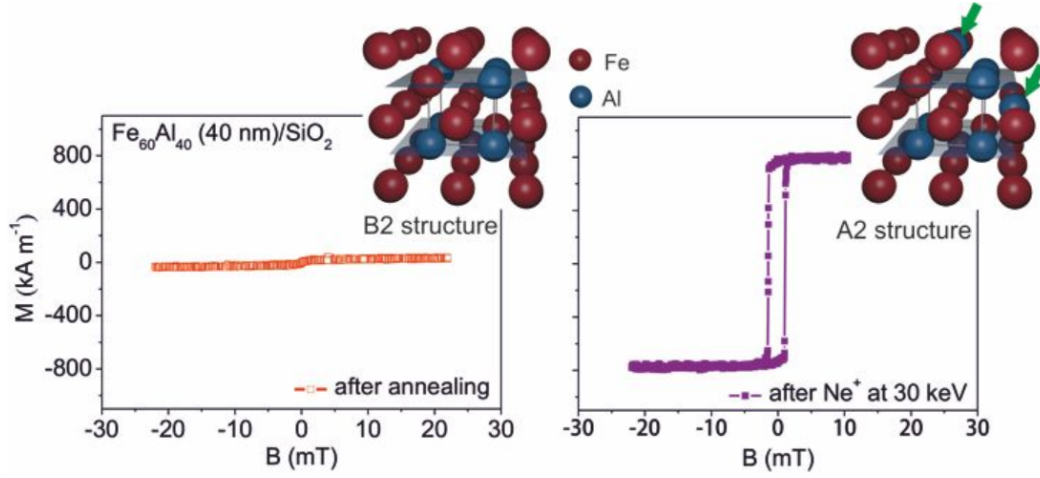


Figure 1.9: *The low saturation magnetization observed on the chemically ordered phase Fe-Al thin films (left), and ferromagnetic observed on the disordered, A2 phase (right) [45].*

structure whereas the Fe and Al atoms are randomly arranged, the number of Fe-Fe nearest neighbor changes to 4.8. This increase in the number of Fe-Fe nearest neighbor is vital for inducing ferromagnetism [46].

On the other hand, chemically ordered (B2 or CsCl-type) FeRh alloys at equi-atomic composition exhibit an antiferromagnetic (AFM) to ferromagnetic (FM) phase transition at around 370 K. Therefore, similar to the FeAl system, chemical disorder introduced into FeRh thin films could lead to an increasing ferromagnetic signal at low temperatures. The chemically ordered state usually occurs in thermal equilibrium, the metastable disordered state can be achieved by ion irradiation which will be discussed in chapter 3.

1.2.4 Chemical composition dependence

An interesting property of FeRh alloys is that the phase transition temperature (T_{tr}) can be modified by changing the chemical composition [40]. Specifically, the magnetic and structural phase transition in the FeRh alloys only take place in the narrow range of $-2 \leq x \leq 2$ at percentage for compounds with the general formula $\text{Fe}_{50-x}\text{Rh}_{50+x}$ [47, 48]. As it is shown in Fig. 1.10 this narrow range of compositions is considered as the α' -FeRh region in the phase diagram. The phase diagram depicted that outside of the α' -FeRh composition region the crystallographic of the FeRh system varies from the chemically ordered CsCl-type phase and does not display a magnetic and structural phase transition. In the equiatomic FeRh system, slight differences in the amount of Fe or Rh content cause a shift of T_{tr} . For the $\text{Fe}_{50-x}\text{Rh}_{50+x}$ binary systems, by adding Rh concentration phase transition shifts towards higher temperature (see Fig. 1.11) [49, 36].

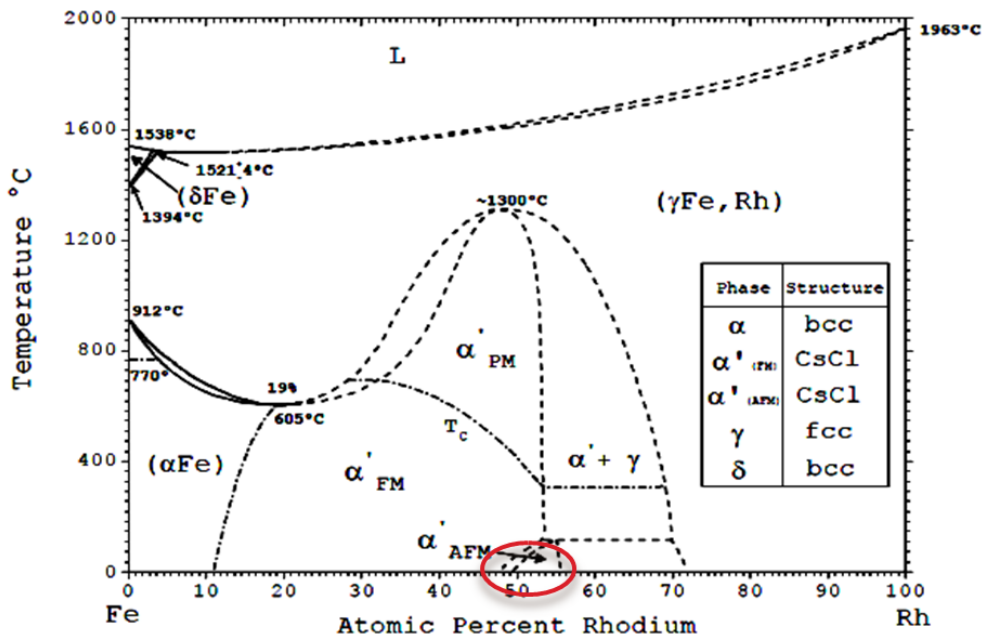


Figure 1.10: FeRh phase diagram. The α' -FeRh region ($48 \leq \text{Fe at.}\% \leq 52$) corresponds to the composition necessary for the magnetic and structural phase transition to occur. Outside of this region, FeRh with varied magnetic- and crystallographic order exists [47].

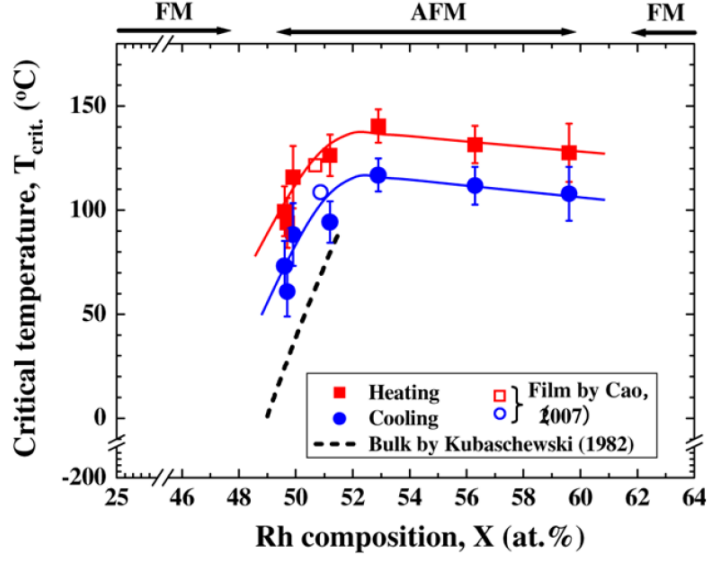


Figure 1.11: Dependence of the AFM-FM transition temperature of $Fe_{50-x}Rh_{50+x}$ with varying Rh content [36].

Moreover, Rh-rich FeRh samples display a decreasing M_s correlated with the $M(T)$ transformation, relative to $M_s \sim 1100 \text{ emu/cm}^3$ reported in bulk FeRh [49].

Using FeRh system sensitivity to the stoichiometry variation, phase transition temperature can be adjusted by substitutional doping into the FeRh structure. It has been shown that phase transition temperature for FeRh bulk sample is increasing by doping with Pt [8, 18], Ir [8], Ru and Os [50]. On the other hand it decreases by doping with either Pd [8, 50]. The variations of T_{tr} by doping for $FeRhM_x$ where $M = \text{Pd, Ru, Pt, Os and Ir}$, while $x = 0.083$ is shown in table. 1.1.

Table 1.1: Phase transition of $FeRhM_x$, while $x = 0.083$ [50].

| FeRhM | $T_{tr}(K)$ |
|-------|-------------|
| Pd | 203 |
| Os | 403 |
| Pt | 443 |
| Ru | 463 |
| Ir | 533 |

It has been reported for ternary systems of FeRh that Pt-doped FeRh thin films exhibit similar property to Pt-doped bulk FeRh. It is proposed that FeRh thin films display a similar behavior to bulk systems with substitutional doping [18]. Note that in the FM phase the magnetic moment is strongly depend on the stoichiometry, as it is depicted in Fig 1.12. The magnetic moment of Fe-rich and Rh-rich FeRh were measured by Shirane et al [52] and Hofer et al. [53], respectively. Fig. 1.13 shows T_{AFM-FM} as a function of atomic concentration of Rh. The FeRh thin film by Rh concentration more than 63% is paramagnetic in the entire measurement temperature range. The origin and physical mechanism underlying the FeRh magnetic phase transition is currently a topic of debate in the scientific community. Many studies have attempted to determine if changes in the magnetism drive the structural transformation or vice versa, however, to date, the mechanism of the transformation is not completely understood. Although the magnetic moment of Fe-rich FeRh alloys at room temperature does not change significantly, T_{AFM-FM} decreases dramatically with increasing the content of Fe percent above 50%. Thereby, there is no first-order phase transition, and the Fe-rich FeRh alloys become a FM material [52]. Moreover, for Rh-rich FeRh system the average magnetic moment at room temperature decreases with increasing concentration of Rh from 50% up to 63%.

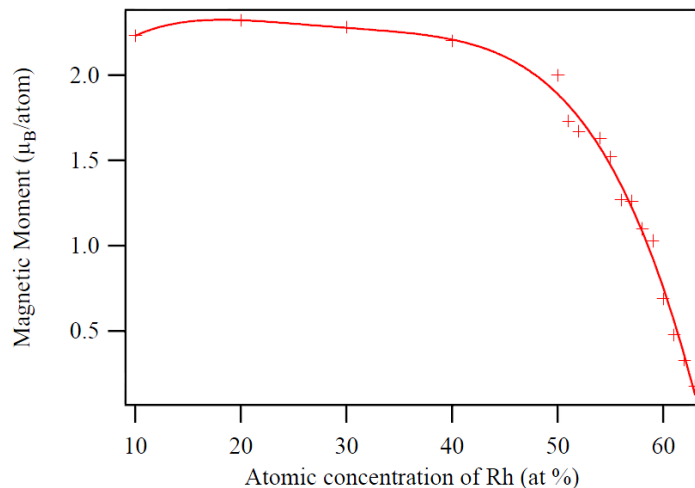


Figure 1.12: Measured average magnetic moment per atom of FeRh as a function of the atomic concentration of Rh at room temperature [24], [52], [53].

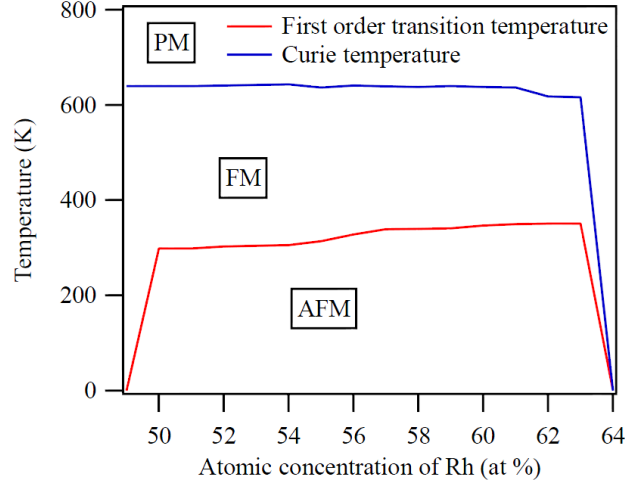


Figure 1.13: Magnetic transition temperature of Rh-rich FeRh alloy as a function of the atomic concentration of Rh at room temperature [24], [53]. The red line is the first-order magnetic phase transition temperature from AFM to FM, and the blue line is the T_C which is also the second order magnetic phase transition temperature from FM to PM. When Rh is more than 64%, FeRh alloy becomes a paramagnet, in this manner the first-order and the second-order magnetic phase transition is absent and the transition temperature decreases to zero .

1.2.5 Effect of applied magnetic field

This section discusses the effect of an applied magnetic field on the magnetic phase transition in FeRh systems. It has been shown that increasing the applied magnetic field leads to reduce the onset of the transition temperature, while retaining the shape of the hysteresis, by approximately -0.8 K/kOe in both bulk [8] and thin film forms of FeRh [34, 35].

Moreover, it has been shown that the magnetic phase transformation can be driven by the application of an applied magnetic field in the vicinity of T_{tr} .

The field-driven transition is attribute by $M(H_{app})$ loop opening, which increases with increasing temperatures until the FeRh system has completely transformed into the FM phase. Fig. 1.14 shows the influence of the applied magnetic field on the T_{tr} . The measurements at $T = 340$ K and $T = 355$ K show difference between magnetization with increasing and decreasing applied magnetic field. While at $T = 380$ K the FeRh system is completely in FM phase and consequently no $M(H_{app})$ opening is observed [54].

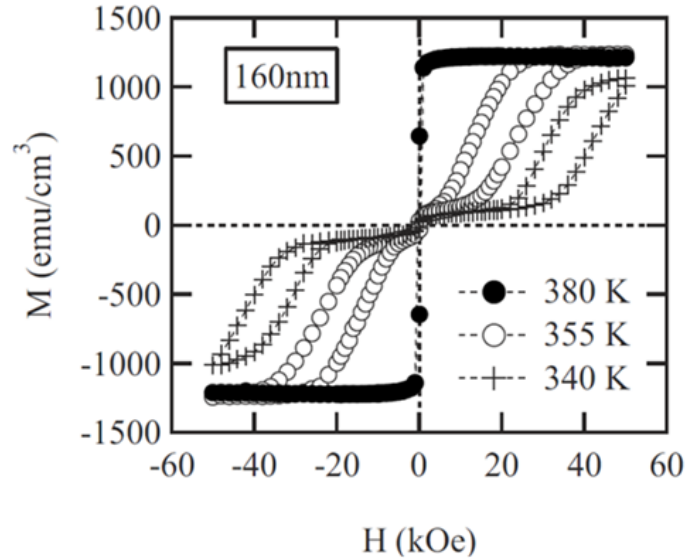


Figure 1.14: $M(H_{app})$ loops of a 160 nm FeRh thin film grown on (001)-MgO substrate at different temperatures near the AFM-FM phase transformation temperature [54].

Since the first-order magnetic phase transition is sensitive to the applied magnetic field also it is interesting to study the effect of field direction. Fig. 1.15 shows the temperature dependence of magnetization for FeRh thin film under an applied magnetic field of 15 kOe in the direction of both parallel and perpendicular to film plane. A sharp increase in magnetization above 393 K during heating in both directions shows the onset of the AFM-FM phase transition in FeRh thin film. At around 413 K, the magnetization gets saturation which is about 1370 emu/cc in perpendicular direction. During cooling the onset of the FM-AFM phase transition occurs at temperature 403 K in parallel direction and below 418 K in perpendicular direction [55].

It is visible that the transition temperature in parallel direction is lower than in perpendicular direction in both heating and cooling processes. This is likely due to the appearance of the self-demagnetization field while the magnetization is perpendicular to the film which tends to retain the formation of the FM phase. Fig. 1.16 illustrates the magnetization curves of FeRh thin film measured at 413 K during heating with different applied magnetic field ranges from 2.5 to 15 kOe. The opening in hysteresis loops observed becomes larger with increasing applied magnetic field from 5 to 15 kOe which indicates a reversible first order

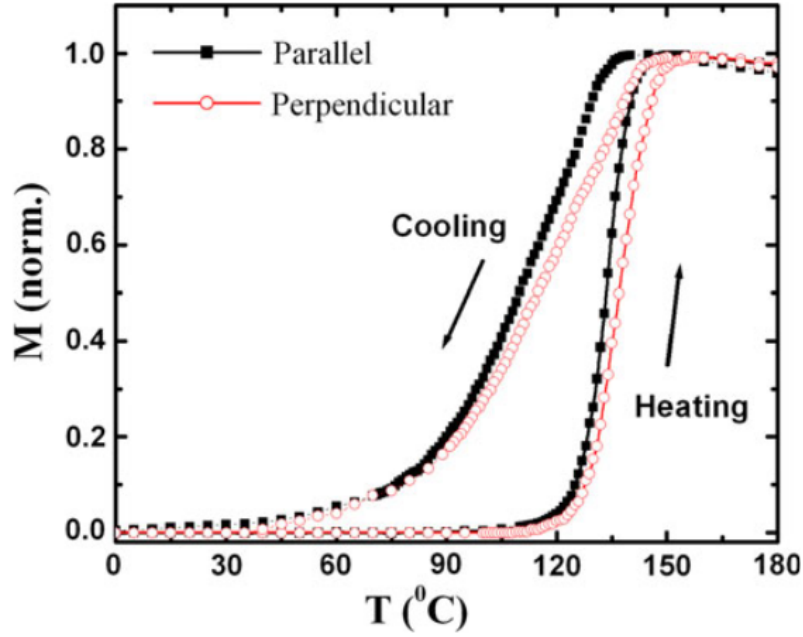


Figure 1.15: Temperature dependence of magnetization curves for FeRh film with an applied magnetic field of 15 kOe in the direction of both parallel and perpendicular to film plane [55].

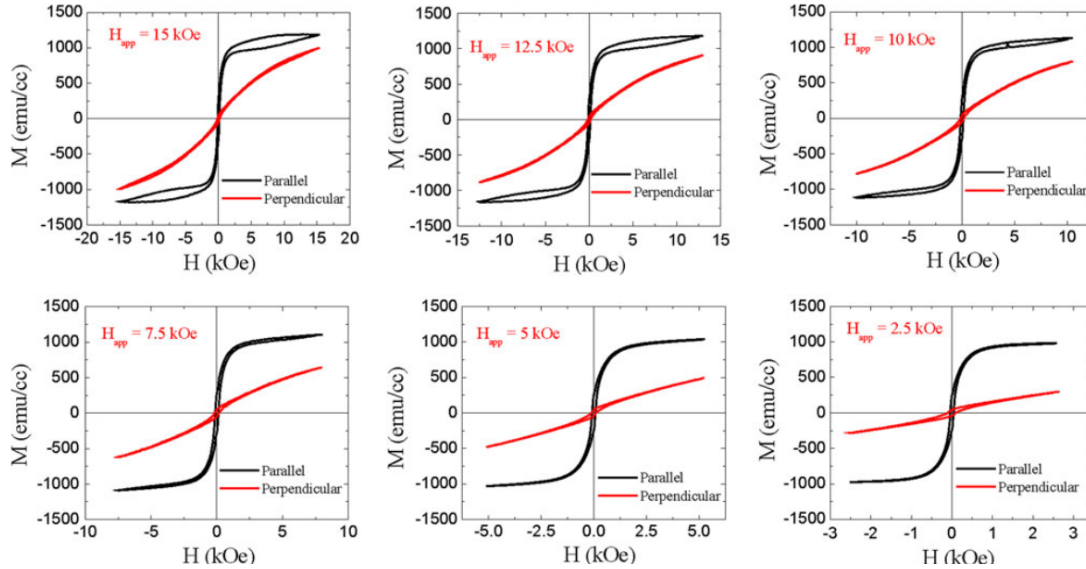


Figure 1.16: M-H loops of FeRh film measured with different applied magnetic field range from 2.5 to 15 kOe at 413 K during heating [55].

AFM to FM phase transition in FeRh system [55]. The origin of this opening will be discussed in the chapter 3.

1.3 Application potential

1.3.1 Heat Assisted Magnetic Recording

After introducing the first disk drive in 1956, magnetic disk storage is one of the most important modern data storage technologies [56]. The fast progress of magnetic hard disks during these years is the consequence of many new technological invention [57], including giant magnetoresistance (GMR) [58] and tunnelling magnetoresistance (TMR) [59]. Although the semiconductor random-access memory is faster than magnetic disk storage for data access, in magnetic disk storage the power is not needed to store the data. Due to the high request to increase capacity of data storage at reducing cost per gigabyte (GB), needs an enormously increasing hard disks storage areal density (GB/in^2). Continually reducing the magnetic grain size is vital to get higher areal density with appropriate signal-to-noise ratio (SNR) of the readback signal [60]. Because of the superparamagnetic limit, the reduction of the grain size leads to the reduction of the thermal stability [61]. In this case the direction of the magnetic grains are arbitrary. This problem can be avoided if the energy barrier to reversal is much greater than the thermal energy $k_B T$, which is the product of Boltzmann constant k_B and the temperature T . On the other hand superparamagnetic effect occurs while thermal energy overcome the switching energy barrier: $K_u V$ Where K_u is the uniaxial anisotropy constant and V is the magnetic grain volume. The stability ratio $K_u V/k_B T$ higher than 35 guarantees to maintain constant media signal to noise ratio [62]. The instability can be improved by increasing the uniaxial anisotropy constant, which is used in perpendicular recording [63]. But the uniaxial anisotropy constant must be continually increased if the grain size continually reduced. The grain size distribution and anisotropy constant should be optimized, otherwise at a point, the maximum magnetic field applied by the hard disk drive will not be able to change the magnetization direction of grains. It has been demonstrated that Heat-assisted magnetic recording (HAMR) is a novel method to develop the storage density continually

[64]. HAMR functions by very rapidly heating the high anisotropy magnetic recording medium to considerably decrease the coercivity during the writing procedure. After writing, in order to thermal stability of the recorded data the system should directly cool down. In HAMR, optical power of a semiconductor laser could be employed as a rapid heat source [65]. The ultrafast phase transition from AFM to FM in FeRh thin film can be generated with femtosecond optical pulses [66]. The problem is that the coercivity for perpendicular magnetic recording medium can be considerably decreased while temperature increases up to near the Curie temperature. In this condition waste of heating cause high power consumption.

A system including one FeRh layer along with a layer of FePt can be a solution for these problems [67]. In particular FePt alloy has high anisotropy ($K_u=7 \times 10^7$ erg/cm³) which is vital for a good thermal stability of storage media. While FeRh system is a good candidate for a magnetic underlayer because of an first-order AFM to FM phase transition slightly above room temperature [68]. As mentioned already the FeRh T_{tr} can simply be tuned by doping an impurity, i.e., doping Pd and Ir can decrease and increase T_{tr} , respectively [69]. For the writing process by heating the FeRh alloy as a soft ferromagnetic system above the phase transition temperature where is in FM phase, extra magnetic field induced through the FePt layer. In the FePt-FeRh system, the interaction of hard phase with high coercivity and the soft phase with high saturation field leads to decrease the total coercivity of the system respect to the individual coercivity of each FeRh and FePt layers. [70]. When the semiconductor laser switch off system cool down to room temperature (after writing) and FeRh system transfers to AFM state, while FePt anisotropy supports the thermal stability of the data storage. The scheme of a high density HAMR hard disk drive is shown on Fig. 1.17. The device involves two main parts: an FeRh/FePt bi-layer system as data storage medium and an integrated read/write head, which has three functions: heating, writing, and reading. In this system a TMR or GMR sensor is used for reading.

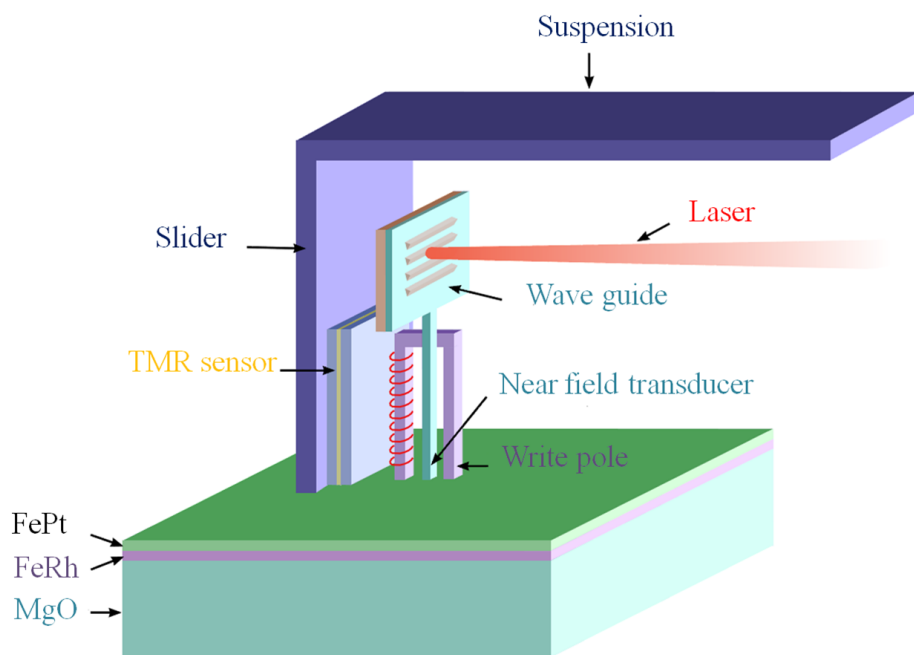


Figure 1.17: Schematic drawing of a heat-assisted magnetic recording setup based on a medium comprising an FeRh/FePt bi-layer system [24].

Bibliography

- [1] M. Fallot, D. L. Alliges and L. Metaux, *Annales de Physique*, **10**, 291-332, (1938).
- [2] M. Fallot, R. Hocart, “On the Appearance of Ferromagnetism upon Elevation of the Temperature of Iron and Rhodium“, *Review of Scientific Instruments*, **8**, 498-500, (1939).
- [3] J. S. Kouvel, and C. C. Hartelius, “Anomalous Magnetic Moments and Transformations in the Ordered Alloy FeRh“, *Journal of Applied Physics*, **33**, 1343-1344, (1962).
- [4] F. D. Muldower, “Crystallographic Study of an Iron-Rhodium Alloy“, *Comptes Rendus de l’Academie des Sciences*, **252**, 1347, (1962).
- [5] G. Shirane, C. W. C , P.A. Flinn, and R. Nathans, “Hyperfine Fields and Magnetic Moments in FeRh System“, *Journal of Applied Physics*, **34**, 044-1045, (1963).
- [6] R. Barua “Pathways for tailoring the magnetostructural response of FeRh-based systems“, PhD thesis. Northeastern University, (2014).
- [7] A. I. Zakharov, A. M. Kadomtseva, R. Z. Levitin and E. G. Ponyatovskii, “Magnetic and Magnetoelastic Properties of a Metamagnetic Fe-Rh Alloy“, *Journal of Experimental and Theoretical Physics*, **46**, 1348-1353, (1964).
- [8] J. S. Kouvel, “Unusual Nature of the Abrupt Magnetic Transition in FeRh and Its Pseudobinary Variants“, *Journal of Applied Physics*, **37**, 1257-1259, (1966).
- [9] J. U. Thiele, S. Maat, J. L. Robertson and E. E. Fullerton, “Magnetic and structural properties of FePt-FeRh exchange spring films for thermally

- assisted magnetic recording media“, IEEE Transactions on Magnetics, **40**, 2537-2542, (2004).
- [10] M. R. Ibarra and P. A. Algarabel, “Giant Volume Magnetostriction in the FeRh Alloy“, Physical Review B, **50**, 4196-4199, (1994).
- [11] L. Zsoldos, “Lattice Parameter Change of FeRh Alloys due to Antiferromagnetic-Ferromagnetic Transformation“, physica status solidi (b), **20**, K25-K28, (1967).
- [12] V. L. Moruzzi and P. M. Marcus. “Antiferromagnetic-ferromagnetic transition in FeRh“, Physical Review B, **46**, 2864-2873, (1992).
- [13] C. Stamm, J.-U. Thiele, T. Kachel, I. Radu, P. Ramm, M. Kosuth, J. Minar, H. Ebert, H. A. Dürr, W. Eberhardt, and C. H. Back, “Antiferromagnetic-ferromagnetic phase transition in FeRh probed by x-ray magnetic circular dichroism“, Physical Review B, **77**, 184401, (2008).
- [14] R. Fan, C. J. Kinane, T. R. Charlton, R. Dorner, M. Ali, M. A. deVries, R. M. D. Brydson, C. H. Marrows, B. J. Hickey, D. A. Arena, B. K. Tanner, G. Nisbet and S. Langridge, “Ferromagnetism at the interfaces of antiferromagnetic FeRh epilayers“, Physical Review B, **82**, 184418, (2010).
- [15] Y. Ding, D. A. Arena, J. Dvorak, M. Ali, C. J. Kinane, C. H. Marrows, B. J. Hickey and L. H. Lewis, “Bulk and near-surface magnetic properties of FeRh thin films“, Journal of Applied Physics, **103**, 07B515, (2008).
- [16] C. Baldasseroni, C. Bordel, A. X. Gray, A. M. Kaiser, F. Kronast, J. Herrero-Albillos, C. M. Schneider, C. S. Fadley and F. Hellman, “Temperature-driven nucleation of ferromagnetic domains in FeRh thin films“, Applied Physics Letters, **100**, 262401-262405, (2012).
- [17] W. Lu, B. Yan and T. Suzuki, “Magnetic phase transition and magneto-optical properties in epitaxial (FeRh)_{0.95} Pt_{0.05} (001) single-crystal thin film“, Scripta Materialia, **61**, 851-854, (2009).
- [18] W. Lu, N. T. Nam and T. Suzuki, Effect of Pt Doping on the Structure, “Magnetic, and Magneto-Optical Properties of Ordered FeRh-Pt Thin Films“, Magnetics, IEEE Transactions on, **45**, 2716-2719, (2009).

- [19] J. W. Kim, , P. J. Ryan, Y. Ding, L. H. Lewis, M. Ali, C. J. Kinane, B. J. Hickey, C. H. Marrows and D. A. Arena, “Surface influenced magnetostructural transition in FeRh films, Applied Physics Letters“, **95**, 222515, (2009).
- [20] M. J. Richardson, , D. Melville and J. A. Ricodeau, “Specific heat measurements on an FeRh alloy“, Physics Letters A, **46**, 153-154, (1973).
- [21] P. Tu, , A. J. Heeger, J. S. Kouvel and J. B. Comly, “Mechanism for the First- Order Magnetic Transition in the FeRh System“, Journal of Applied Physics, **40**, 1368-1369, (1969).
- [22] D. W. Cooke, F. Hellman, C. Baldasseroni, C. Bordel, S. Moyerman and E. E. Fullerton, “Thermodynamic Measurements of Fe-Rh Alloys“, Physical Review Letters, **109**, 255901, (2012).
- [23] L. M. Sandratskii and P. Mavropoulos. “Magnetic excitations and femtomagnetism of FeRh: A first-principles study“, Physical Review B, **83**,174408, (2011).
- [24] X. Zhou, “Temperature-Induced Metamagnetic Transition and Domain Structures of Single-Crystalline FeRh Thin Films on MgO(100)“, PhD Thesis, University of Koln, (2013).
- [25] D. A. Porter, and K. E. Easterling, “ Phase Transformation in Metals and Alloys “, Third ed, Van Nostrand Reinhold Berkshire, (1983).
- [26] J. M. D. Coey, “Magnetism and magnetic materials“, Cambridge University Press, (2010).
- [27] Kittel, C., “Model of exchange-inversion magnetization“, Physical Review, **120**, 335, (1960).
- [28] M. E. Gruner, E. Hoffmann and P. Entel, “Instability of the rhodium magnetic moment as the origin of the metamagnetic phase transition in alpha-FeRh“, Physical Review B, **67**, 1368-1369, (2003).

- [29] D. W. Cooke, F. Hellman, J. R. Groves, B. M. Clemens, S. Moyerman and E. E. Fullerton, "Calorimetry of epitaxial thin films, Review of Scientific Instruments", **82**, 023908-023904, (2011).
- [30] Y. Ding, D. A. Arena, J. Dvorak, M. Ali, C. J. Kinane, C. H. Marrows, B. J. Hickey and L. H. Lewis, "Bulk and near-surface magnetic properties of FeRh thin films", Journal of Applied Physics, **103**, 07B515, (2008).
- [31] J. M. Lommel, "Role of oxygen in obtaining complete magnetic first order transitions in FeRh films", Journal of Applied Physics, **40**, 1466-1467, (1969).
- [32] E. Brück and et al, "Developments in magnetocaloric refrigeration", Journal of Physics D: Applied Physics, **38**, R381, (2005).
- [33] M. K. Chattopadhyay, S. B. Roy, A. K. Nigam, K. J. S. Sokhey and P. Chaddah, "Metastability and giant relaxation across the ferromagnetic to antiferromagnetic transition in $\text{Ce}(\text{Fe}_{0.96}\text{Ru}_{0.04})_2$ ", Physical Review B, **68**, 174404, (2003).
- [34] Maat, S., J. U. Thiele and E. E. Fullerton, "Temperature and field hysteresis of the antiferromagnetic-to-ferromagnetic phase transition in epitaxial FeRh films", Physical Review B, **72**, 214432, (2005).
- [35] A. C. Hsiao, L. H. Lewis, K. Kang and A. R. Moodenbaugh, "Magnetism and metastability of melt-spun $\text{Pd}_{40}(\text{Fe,Ni})_{40}\text{P}_{40}$ metallic glass", Journal of Applied Physics, **99**, 08F117, (2006).
- [36] S. Inoue, H. Y. Y. Ko and T. Suzuki, "Magnetic Properties of Single-Crystalline FeRh Alloy Thin Films", IEEE Transactions on Magnetics, **44**, 2875-2878, (2008).
- [37] M. A. d. Vries, M. Loving, A. P. Mihai, L. H. Lewis, D. Heiman and C. H. Marrows, "Hall-effect characterization of the metamagnetic transition in FeRh", New Journal of Physics, **15**, 013008, (2013).
- [38] J. Cao, N. T. Nam, S. Inoue, H. Y. Y. Ko, N. N. Phuoc and T. Suzuki, "Magnetization behaviors for FeRh single crystal thin films", Journal of Applied Physics, **103**, 07F501, (2008).

-
- [39] J. P. Ayoub, C. Roucau, M.J.Casanove, “Structure and chemical order in FeRh nanolayers epitaxially grown on MgO(0 01)“, *Journal of Crystal Growth*, **314**, 336, (2010).
- [40] A. I. Zakharov, A. M. Kadomtseva, R. Z. Levitin and E. G. Ponyatovskii, “Magnetic and Magnetoelastic Properties of a Metamagnetic Fe-Rh Alloy“, *Journal of Experimental and Theoretical Physics*, **46**, 1348-1353, (1964).
- [41] W. Lu, , P. Huang, K. Li and B. Yan, “Effect of substrate temperature on the crystallographic structure and first-order magnetic phase transition of FeRh thin films“, *Journal of Materials Research*, 1-5, (2013).
- [42] S. Maat, J. U. Thiele and E. E. Fullerton, “Temperature and field hysteresis of the antiferromagnetic-to-ferromagnetic phase transition in epitaxial FeRh films“, *Physical Review B*, **72**, 214432-214435, (2005).
- [43] M. Loving, F. Jimenez-Villacorta, B. Kaeswurm, D. A. Arena, C. H. Marrows and L. H. Lewis, “Structural evidence for stabilized ferromagnetism in epitaxial FeRh nanoislands“, *Journal of Physics D: Applied Physics*, **46**, 162002, (2013).
- [44] E. Menendez, M.O. Liedke, J. Fassbender, T. Gemming, A. Weber, L.J. Heyderman, K.V. Rao, S.C. Deevi, S. Surinach, M.D. Baro, J. Sort, J. Nogues, *Small*, **5**, 229, (2009).
- [45] Available in: <https://www.hzdr.de/db/Cms?pOid=29538>.
- [46] R. Bali, S. Wintz and et al, “Printing Nearly-Discrete Magnetic Patterns Using Chemical Disorder Induced Ferromagnetism“, *Nano Lett*, **14**, 435-441, (2014).
- [47] L. J. Swartzendruber, “The FeRh (Iron-Rhodium) system“, *Bulletin of Alloy Phase Diagrams*, **5**, 456-462, (1984).
- [48] N. Duman, M. V. Akdeniz and A. O. Mekhrabov, “Magnetic monitoring approach to nanocrystallization kinetics in Fe-based bulk amorphous alloy“, *Intermetallics*, **43**, 152-161, (2013).

- [49] J. VanDriel, R. Coehoorn, G. J. Strijkers, E. Brack and F. R. deBoer, *Journal of Applied Physics*, **85**, 1026-1036, (1999).
- [50] P. H. L. Walter, "Exchange Inversion in Ternary Modifications of Iron Rhodium", *Journal of Applied Physics*, **35**, 938-939, (1964).
- [51] K. Kamenev, Z. Arnolda, J. Kamarada and N. V. Baranovb, "Pressure induced antiferromagnetism in $(\text{Fe}_{1-x}\text{Ni}_x)_{49}\text{Rh}_{51}$ alloys", *Journal of Alloys and Compounds*, **252**, 5680-5682, (1997).
- [52] G. Shirane, R. Nathans, and C. W. Chen, "Magnetic moments and unpaired spin densities in the Fe-Rh alloys", *Physical Review*, **134**, A1547-1553, (1964).
- [53] P. E. M. Hofer and P. E. Cucka. "Magnetic Properties of Rh-rich FeRh alloy", *Journal of Physics and Chemistry*, **27**, 1552-1555, (1966).
- [54] I. Suzuki, T. Koike, M. Itoh, T. Taniyama and T. Sato, "Stability of ferromagnetic state of epitaxially grown ordered FeRh thin films", *Journal of Applied Physics*, **105**, 1-3, (2009).
- [55] L. Wei, W. Yuxin, Y. Biao, and S. Takao, "Magnetic properties and first-order magnetic phase transition in single crystal FeRh thin film" , *J. Mater. Sci*, **45**, 4919-4923, (2010).
- [56] E. Grochowski and R. D. Halem. "Technological impact of magnetic hard disk drives on storage systems", *IBM Systems Journal*, **42**, 338-346, (2003).
- [57] E. Grochowski and R. F. Hoyt. "Future trends in hard disk drives", *IEEE Transactions on Magnetics*, **32**, 1850-1854, (1996).
- [58] M. N. Baibich, J. M. Broto, A. Fert, F. N. Van Dau, F. Petroff, P. Etienne, G. Creuzet, A. Friederich, and J. Chazelas. "Giant magnetoresistance of (001)Fe/(001)Cr magnetic superlattices", *Physical Review Letters*, **61**, 2472-2475, (1988).
- [59] S. S. P. Parkin, C. Kaiser, A. Panchula, P. M. Rice, B. Hughes, M. Samant, and S.-H. Yang. "Giant tunnelling magnetoresistance at room temperature with MgO(100) tunnel barriers", *Nature Materials*, **3**, 862-867, (2004).

-
- [60] M. F. Doerner, K. Tang, T. Arnoldussen, H. Zeng, M. F. Toney, and D. Weller, "Microstructure and thermal stability of advanced longitudinal media", *IEEE Transactions on Magnetics*, **36**, 43-47, (2000).
- [61] D.A. Thompson and J.S. Best. "The future of magnetic data storage technology", *IBM Journal of Research and Development*, **44**, 311-322, (2000).
- [62] D. Weller and Andreas Moser. "Thermal effect limits in ultrahigh-density magnetic recording", *IEEE Transactions on Magnetics*, **35**, 3544-3549, (1999).
- [63] S. N. Piramanayagam. "Perpendicular recording media for hard disk drives", *Journal of Applied Physics*, **102**, 011301, (2007).
- [64] M.H. Kryder, E.C. Gage, T.W. McDaniel, W.A. Challener, R.E. Rottmayer, G. Ju, Y.-T. Hsia, and M.F. Erden. "Heat assisted magnetic recording", *Proceedings of the IEEE*, **96**, 1810-1835, (2008).
- [65] W. A. Challener, Chubing Peng, A. V. Itagi, D. Karns, W. Peng, Y. Peng, X. Yang, X. Zhu, N. J. Gokemeijer, Y. T. Hsia, G. Ju, R. E. Rottmayer, M. A. Seigler, and E. C. Gage. "Heat-assisted magnetic recording by a near-field transducer with efficient optical energy transfer", *Nature Photonics*, **3**, 220-224, (2009).
- [66] I. Suzuki, T. Koike, M. Itoh, T. Taniyama and T. Sato, "Stability of ferromagnetic state of epitaxially grown ordered FeRh thin films", *Journal of Applied Physics*, **105**, 1-3, (2009).
- [67] J. U. Thiele, S. Maat, and E. E. Fullerton. "FeRh/FePt exchange spring films for thermally assisted magnetic recording media", *Applied Physics Letters*, **82**, 2859-2861, (2003).
- [68] J. S. Kouvel, and C. C. Hartelius. "Anomalous magnetic moments and transformations in the ordered alloy FeRh", *Journal of Applied Physics*, **33**, 1340-1344, (1962).
- [69] J. S. Kouvel, "Unusual nature of the abrupt magnetic transition in FeRh and its pseudobinary variants", *Journal of Applied Physics*, **37**, 1257-1258, (1966).

- [70] M. P. N. Annaorazov, S. A. Tyurin, A. L. Asatryan, K. A. and Dovletov, A. Kh., “Anomalously high entropy change in FeRh alloy“, *Journal of Applied Physics*, **79**, 1689-1695, (1996).

Chapter 2

Experimental Techniques

In this chapter, the experimental setups which were employed to obtain the presented results are explained. The techniques used to prepare FeRh thin films in this work are based on Ultra-High Vacuum (UHV). Two kinds of system were used for preparation of samples: (i) Molecular Beam Epitaxy (MBE) and (ii) Sputtering methods. The variety of measurements such as Rutherford Backscattering Spectrometry (RBS), X-ray diffraction (XRD), Auger Electron Spectroscopy (AES), Superconducting Quantum Interference Device (SQUID-MPMS), Transmission Electron Microscopy (TEM), Magneto-optical Kerr effect (MOKE) and Ferromagnetic Resonance (FMR) were used to study magnetic and structural properties of samples. The process of preparing samples by MBE was done at Helmholtz Zentrum Dresden Rosendorf while sputtered samples have been prepared at the University of Manchester in the group of Prof. T. Thomson. The combination of these approaches can help understanding the magnetic and structural properties of FeRh samples prepared with different systems.

2.1 Thin film growth techniques

2.1.1 Molecular Beam Epitaxy

There is a wide variety of methods to prepare thin films. One of the most established techniques is molecular beam epitaxy (MBE). MBE setups are UHV machines with the base pressure below 5×10^{-10} mbar. MBE is a procedure for the fabrication of ultra clean samples with atomic precision. The concept of MBE can be applied to different material systems like metals, semiconductors

and insulators and it is used for fundamental research as well as for industrial applications. The advantage of MBE is a low growth rate of ~ 1 monolayer (lattice plane) per second, low growth temperature, smooth growth surface with steps of atomic height and large flat terraces, precise control of surface composition and morphology. A sketch and photo of our MBE system (ALDI) is shown in Fig. 2.1 and Fig. 2.2. To achieve a high degree of sample purity, the growth chamber (GC) is evacuated to ultra-high vacuum (UHV, 5×10^{-10} mbar). For a typical GC with a diameter of approximately 1 meter a pressure in the 10^{-5} mbar range is needed to ensure that the mean free path of the evaporated materials is larger than the distance between effusion cells and sample, so that the material can reach the sample without being affected by residual gas molecules. The UHV guarantees that almost no residual gas molecules condense on the substrate surface and are unintentionally combined in the crystal during the growth process. The growth process in MBE is usually an epitaxial process, i.e. the grown structure implements the crystal phase of the substrate. A typical MBE GC is equipped with Knudsen cells, a manipulator which hosts the samples holder and heater, sources of molecular beams, shutters to close the molecular beams, a quadrupole mass analyzer to monitor specific background gas species, and a monitoring system like quartz crystal microbalance (QCM) to control the thickness during the growing process.

MBE system involves four chambers: load-lock, cross chamber (using to avoid of sending contaminations to growth chamber), transfer chamber and growth chamber, which are separated from each other by gate valves. The load-lock chamber is equipped with a heating lamp for the degassing of the substrates and a turbo pump, which provides a pressure down to 1×10^{-8} mbar. Since the load lock is often more contaminated as compare to the other chambers, it has higher pressure. While the pressures in the cross and transfer chambers is generated with a turbo pump, can reach below 10^{-10} mbar. The sketch of growth chamber that is shown in Fig. 2.3(a) and its photo in Fig. 2.3(b) is equipped with an e-beam evaporator, 4 Knudsen cells, a large turbo pump, a titanium sublimation pump and manipulator. The e-beam evaporator used for evaporation of high melting point elements, consists of 4 crucibles typically holding Pt, Rh, Cr and Ni for thin film deposition. On the other hand, Fe, Cu, Ni and Ag elements could be evaporated from Knudsen cells. The Knudsen cells have an angle of

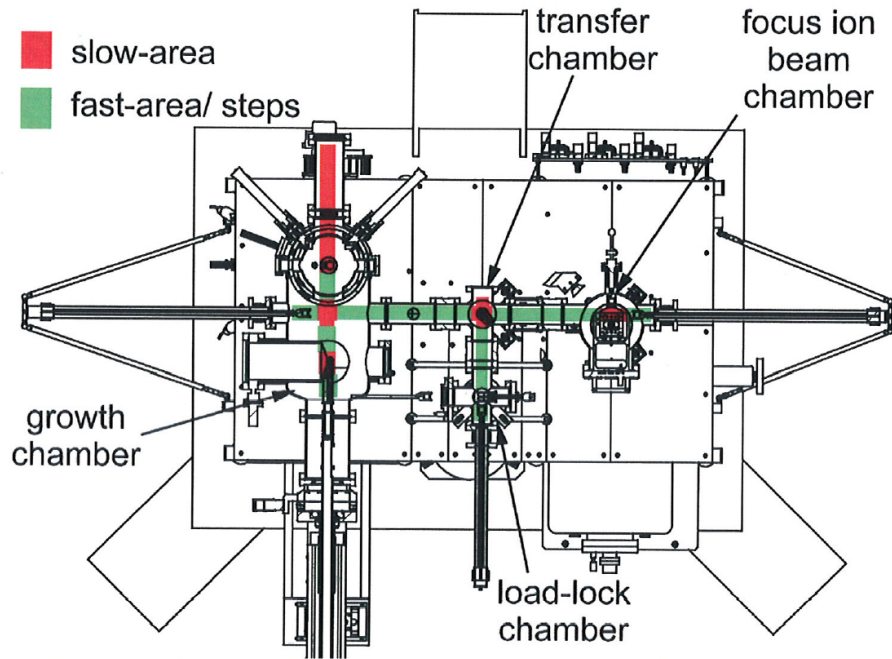


Figure 2.1: (a) Sketch of the MBE setup [1].

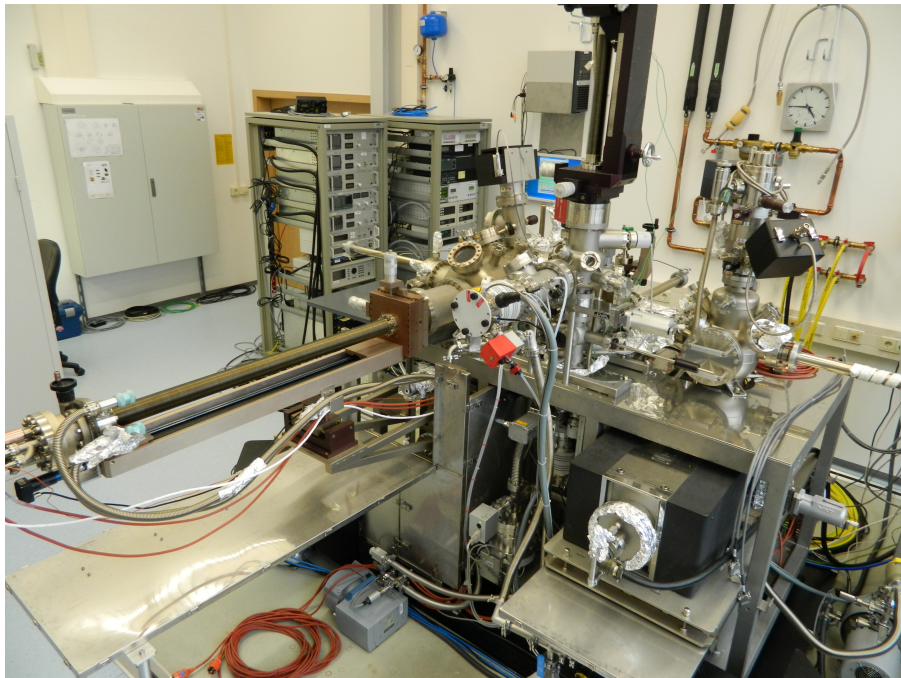


Figure 2.2: photo of the MBE setup.

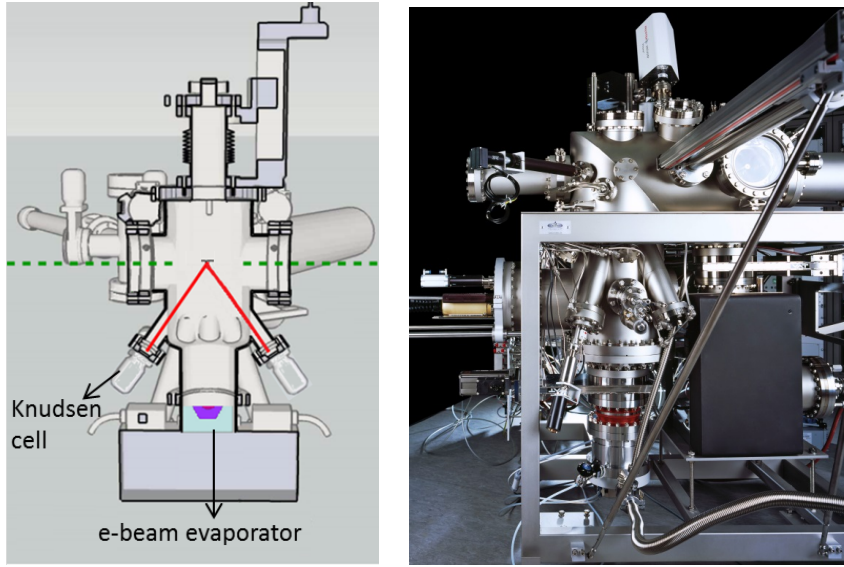


Figure 2.3: (a) Schematic diagram of the growth chamber and (b) Photo of the growth chamber.

30° pointing at the sample surface normal. While the e-beam crucibles have normal angle respect to the sample surface. Furthermore, the GC is hosted with two shutters that can be positioned in front of the sample to protect the surface during the Knudsen cells heating. The manipulator supports a heater so that the sample can be heated up to 1000°C . The thermocouple located in the substrate heater near to the substrate allows to measure the temperature at the sample. The manipulator can be rotated by 360° around one axis.

The main purpose of the MBE system is the thin film deposition and structural as well as chemical characterization. The samples, which are prepared in the MBE system, need to be transferred through air for further measurements. Upon exposure to air, the sample will be oxidized or contaminated. Therefore, the effect of time also was studied for FeRh thin films. During the course of this work three different sample holders: $4 \times 4\text{mm}^2$, $5 \times 5\text{mm}^2$ and $10 \times 10\text{mm}^2$ were used. Since the probe of ferromagnetic resonance set up has $4 \times 4\text{mm}^2$ size, the samples which prepared by using $10 \times 10\text{mm}^2$ and $5 \times 5\text{mm}^2$ sample holders were cut to $4 \times 4\text{mm}^2$.

2.1.2 Sputtering

The most typical approach to grow FeRh thin films is sputtering from an FeRh alloy target with different composition (e.g. Fe₅₁Rh₄₉ [2], Fe₅₀Rh₅₀ [3], Fe₄₇Rh₅₃ [4]). For this study, several samples of FeRh thin films have been deposited by means of magnetron sputtering. Equiatomic sputtered FeRh thin films are used to examine the effect of the preparation methods on the dynamic and static magnetic properties. In the fundamental sputtering process, the material to be deposited (target) is bombarded with energetic ions produced in glow discharge plasma. Due to the momentum transfer from the impacting ions to the target, atoms are removed. These atoms go across through the discharge area and ultimately deposit on a substrate. As a result of ion bombardment secondary electrons are generated from the target surface (and sputtering of target atoms). These electrons have an essential role in sustaining the plasma. Magnetron sputtering is employed in many application areas successfully, mainly in surface engineering and microelectronics, for the preparation of films. The main benefits of this method to prepare thin films are that it is easy to control the composition of thin films by using alloy targets of different compositions and also having high deposition rates at the substrate compared to MBE. Additionally, by sputter deposition can produce films with new physical and useful properties e.g. nanocrystalline films [5, 6]. A schematic sketch of a typical, simple magnetron sputtering system is illustrated in Fig. 2.4.

2.2 Preparation of FeRh thin films

In this study FeRh thin films were grown by MBE with thicknesses range 4-40 nm on MgO (001) single-crystal substrates. Slight variations in the sample preparation, e.g. annealing the substrate, can lead to differences in the film composition, i.e. in the Rh concentration and therefore to a different magnetic behavior. It is well established that Fe can be grown on MgO(100) substrates epitaxially. In order to the large mismatch approximately 0.66% with the lattice constants of MgO(100) [7] it is not possible for Rh. While the mismatch between the bulk B2 FeRh lattice and the MgO lattice is much smaller (about 0.3%). In the first step to grow FeRh thin films the MgO substrates were rinsed with

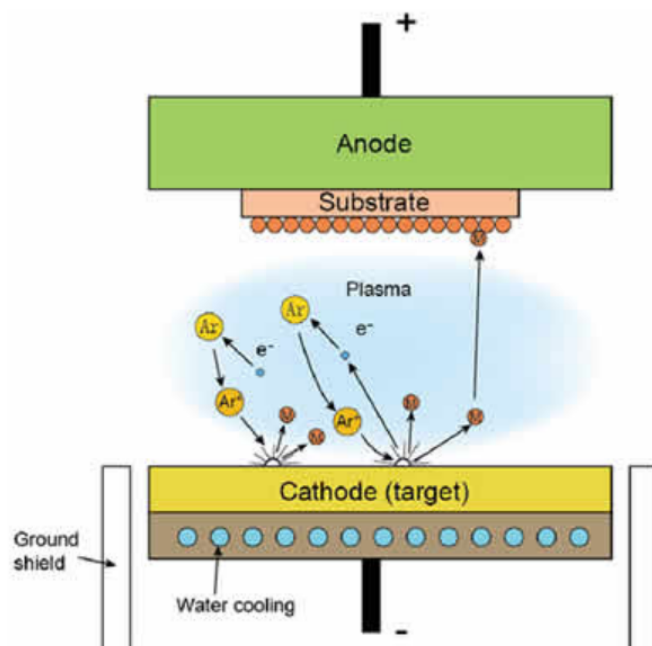


Figure 2.4: Schematic of a simple sputtering system [8].

isopropanol, mounted in the load lock and baked by heating lamp up to 393 K for 4 hours to avoid the contamination of GC. After that, samples were transferred through the cross and transfer chambers into the GC and placed onto the manipulator for growth of FeRh thin films. In this section, the effect of MgO substrate preparation on the epitaxial growth and magnetic behavior of equiatomic FeRh thin films is studied. For this, two different approaches were used to prepare the MgO substrates. First, the substrate was annealed at 873 K for 2h, then at 1073 K for 2h and finally at 1123 K for 4h under stable conditions in UHV. While for another approach the MgO substrate annealed at 873 K for 8 hours prior to the FeRh deposition. Fe₅₀Rh₅₀ thin films nominally with 40 nm thickness were deposited on the both substrates and annealed under the same conditions.

During equiatomic FeRh thin film growth, QCM shows relatively higher Rh evaporation rate for the same number of Fe and Rh evaporated atoms. It is because of higher Rh atom weight. As mentioned already a QCM was placed next to the sample and exposed to the flux of the evaporated Fe and Rh atoms. It was used to control the evaporation rate in the GC and thickness of thin films. During the growing, Fe atoms rate was $0.6 \text{ \AA}^2/\text{sec}$ and $0.8 \text{ \AA}^2/\text{sec}$ was for

Rh atoms. The temperature for Knudsen cell was 1479 °C to get the favorite rate of Fe atoms. On the other hand, high currents between 80 to 90 mA were applied directly in the e-beam for Rh evaporation. The film thickness also was determined using X-ray reflectivity measurement (XRR) which will be discussed in the next few pages. By the flux calibration, the shutters opened and growing process started. After the preparation an annealing process was performed to create the chemically ordered B2 phase of FeRh thin films. For first category of substrates, the films were heated up from room temperature to 873 K/1073 K and finally to 1123 K. Under stable conditions the samples stayed at these temperatures for 2h/2h and 4h, respectively. While for second category of substrates the maximum annealing temperature for thin films was 973 K to avoid of FeRh penetration to the MgO substrate and duration of annealing was 2h. The following sections describe the experimental techniques which have been used to characterize the magnetic and structural properties of bulk and thin film forms of FeRh, which includes: FeRh composition (stoichiometry) (Section 2.4), structural characterization (Section 2.5) and magnetic properties of FeRh system (Section 2.6).

2.3 Ion irradiation

Ion irradiation is a powerful technique in materials science. In particular, ion irradiation technique offers a quantitative control of the degree of chemical disorder simply by adjusting the ion fluence applied, while the penetration depth of the disordered phase can be adjusted by the ion-energy. This process is used to modify or even change the chemical, electrical and magnetic properties of the target materials [9]. Directing a broad ion beam onto a surface causes, strongly dependent on the mass ratio between ions and target atoms, ion irradiation on the one hand and surface erosion on the other hand. The magnetic properties can be adjusted by chemical disordering through the optimizing parameters, such as concentration, defect type and distribution in target materials which induced ferromagnetism. One of the method to generate disorder in the thin films is to expose the chemically ordered alloy as a target to energetic ions. In this case collision cascades are produced by the ions knock target atoms from their

ordered sites and the associated vacancies are distributed randomly through the atomic thermal diffusion at room temperature. As it is shown in Fig. 1.9 a good example is irradiation of Fe₆₀Al₄₀ thin film which atomic displacements can induced a large increase in the saturation magnetization. In this condition the ordered structure thereby undergoes a transition into a metastable solid solution [10]. Through the collision, the incident energetic ions transfer a part of their energy to the target. The stopping force is given by:

$$S(E) = \frac{dE}{dr} \quad (2.1)$$

E is the kinetic energy of the incident particle, and r is the path length. The $S(E)$ describes the average rate of the energy transferred to the target upon each scattering process probabilities. $S(E)$ can be employed to investigate the target properties. Prior to ion implantation, the Stopping and Range of Ions in Matter program (SRIM-2011) was used to simulate the distribution of Ne ions inside the FeRh sample as well as overall damage created vacancies. SRIM-2011 is a Monte-Carlo code that provides theoretical projections of the energies and depth profiles [11].

Fast ions when it enter a solid may collide either with the atomic nuclei or the electrons of the solid. The nuclear collisions are consider to be elastic, although they might be accompanied by energy transfer in the system of electrons as it will be shown below. The collision with electrons are often called inelastic are responsible of ionization or excitation events. For both nuclear and electronic collisions, the most basic method is the binary elastic interaction of two point charges as sketched in Fig. 2.5. The target particle has zero velocity in the laboratory system (LS) any thermal velocity is negligible compared to the ion energy range of interest ($\gg 1$ eV).

In the collision process, the projectile and the recoil particle determined by asymptotic scattering angles Θ and φ , respectively. Since the total momentum of the system is conserved, the kinematics are characterized in the centre-of-mass system (CMS) with the deflection angle ϑ in the CMS. Thereby the two-body system can be reduced to the kinematics in term of single particle with the

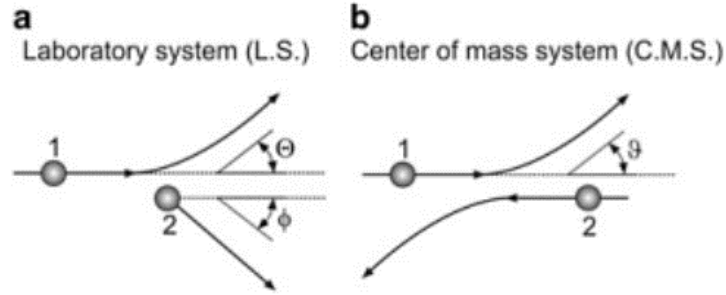


Figure 2.5: *Elastic scattering in the laboratory system (a) and the centre-of-mass system (b). The moving charged particle is indexed by 1, the target particle by 2 [24].*

reduced mass

$$\mu = \frac{m_1 m_2}{m_1 + m_2} \quad (2.2)$$

where m_1 and m_2 indicate the masses of the moving projectile and the target particle, respectively and the reverse transformation is given by

$$\vartheta = \Theta + \arcsin\left\{\frac{m_1}{m_2} \sin\Theta\right\} \quad (2.3)$$

Equation 2.3 shows the existence of a maximum LS scattering angle in case of $m_1 \geq m_2$.

With continuous irradiation, target atoms are constantly displaced, and repeatedly displaced at sufficiently high ion fluence. This theory was explained by using reference [24]. In case of neglecting the crystalline effects, the total number of displacements per unit volume rises linearly with the ion fluence and the displacements per atom of the irradiated volume can be written as:

$$dpa = \frac{\gamma\Phi}{\rho} \quad (2.4)$$

Where γ is the total number of displacements per incident ion per unit penetration and φ is fluence and ρ is atomic density. The required fluence can be calculated from Equation 2.4 by assuming $dpa=1$ (which all sample atoms experience at least one time displacement) and SRIM gives γ as shown in Fig. 3.29(b).

Some fundamental parameters about ion irradiation should be determined:

- Lattice binding energy (LBE)
The energy that each atom of the recoiling target loses (LBE) while it leaves its original lattice site and recoils in the target.
- Threshold displacement energy (TDE)
In a solid, TDE is the energy that is required to dislocate an atom from its original site to generate a defect [12].

Upon ion irradiation, if the transferred energy to the target atoms is higher than TDE, the target atoms can leave their lattice sites and therefore generate defects. These knocked atoms can collide with other atoms in target and displace them. This sequence of displacements and collision is called "collision cascade" which generally produce damage during ion irradiation in target.

2.4 Compositional Characterization

2.4.1 Rutherford Backscattering Spectrometry

It has been known in FeRh systems that the magnetic phase transition depends on the composition enormously [13, 14, 15]. Rutherford Backscattering Spectrometry (RBS) uses a stream of high-energy ionized He particles for investigation the thin film composition and thickness. RBS in the channeling geometry can provide complementary information on crystalline order in thin films. The direction of the incident He⁺ beam alignment has a key role to investigate the disorder degree in the sample. The difference between the backscattering signal while the incident beam is randomly oriented (I_{random}) and when it aligned along the high-index crystalline direction ($I_{channeling}$), is calculated as: $\chi_{min} = I_{channeling}/I_{random}$ [16].

It can take advantage of RBS depth resolution to distinguish the disorder at the film surface, substrate interface, film and bulk. Fig. 2.6 shows the schematic diagram of RBS set up. The surface barrier detector, is normally mounted in a back scattering angle θ of 170° from the incident beam. The probe particles in this case are 1.7 MeV He⁺. As the incident charged particles enter the target matrix some of them will encountered the Coulomb force from target nuclei which deflects their origin path. These collisions are control via the Rutherford

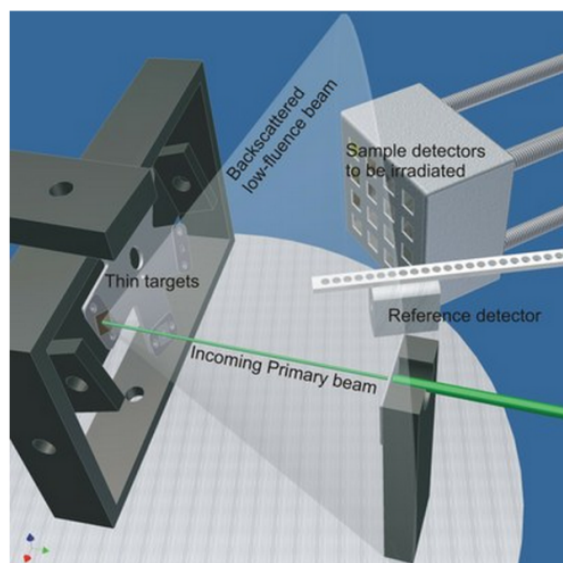


Figure 2.6: Schematic diagram of RBS set up [17].

cross section. During this process a small but adequate number of the deflected incident ions are backscattered toward the detector. The SIMNRA software is used to simulate the experimental measurements. By fitting the experimental and simulated curve the composition and thickness of samples can be extracted.

2.4.2 Auger Electron Spectroscopy

Auger Electron Spectroscopy (AES) is a technique which allows to identify the quantitative elemental as well as chemical state information from surface in a solid. In this study, AES was used to check characterize the thin film growth FeRh deposited by MBE technique. The generation of Auger electron phenomena is discussed by using reference [18]. In a typical AES measurement, the target is irradiated with a high-energy electron beam (approximately 3 keV) by an electron gun. For an AES measurement the average penetration depth of analysis is about 5 nm.

As it is shown in Fig. 2.7 the electrons or x-rays with a kinetic energy of a few keV bombard a sample surface which may collide with an electron in the inner level (K level) and knock it outside of the atom (Fig. 2.7(a)). In this condition an electron from L level occupied the vacancy in the K level to get the stable state. During this process extra energy which is equal to the different energy

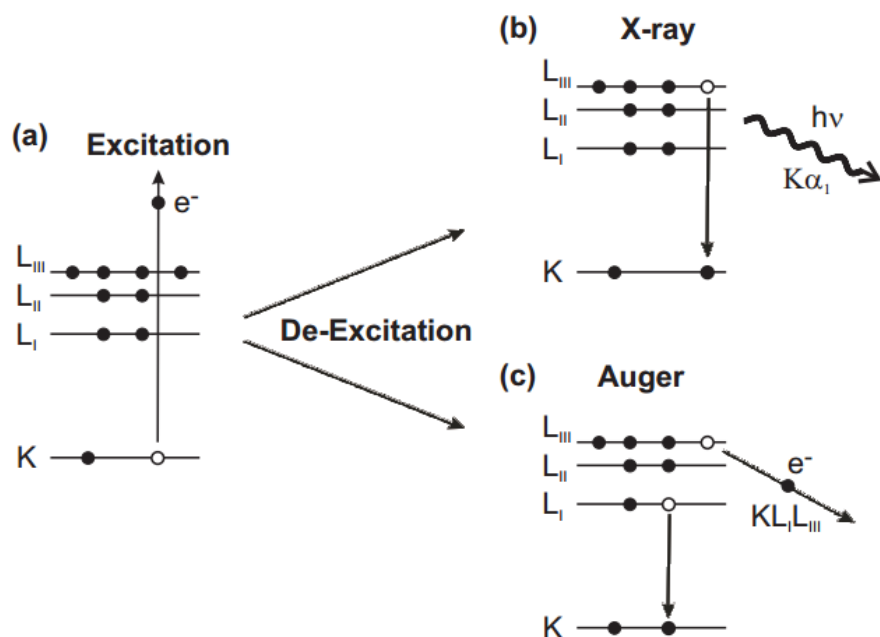


Figure 2.7: Schematic diagram of the processes associated with the Auger process. An electron is ejected from the inner K-shell of the atom (a). The resulting electron gap (b) is affected by an electron from a higher energy level (L-shell) filled and emission of Auger electron(c). Figure has been modified from reference [19].

between K and L level is produced. This energy can be emitted from the atom either by forming X-ray and emitting energy (Fig. 2.7(b)) or an electron in the L level gets the energy and is ejected (Fig. 2.7(c)). The ejected electron is called Auger electron. The energy of an Auger electron is not exactly equal to the difference energy between K and L, as some part is used to make the jump outside the atom. Each kind of atom has unique value for Auger electron and is about 10 to 3000 eV. Since by this energy an electron can only pass a few nm through the solid without losing energy, Auger electron is emitted from a region directly below the surface of a solid. Therefore Auger microprobe is an appropriate instrument for surface analysis.

It is required to slowly remove material from the surface area to investigate the variation of composition with depth below the surface region of a sample. It can be fulfilled by simultaneously exposing the surface of the sample to a flux of an ion. This ion bombardment leads to sputtering of material from the surface. During the measurement the Auger spectra is continuing recorded and

monitored for analyzing. This technique that gives information about variation of composition with depth below the surface is called Auger Depth Profiling.

2.5 Structural Characterization

2.5.1 X-ray diffraction

High resolution X-ray diffraction (XRD) is a powerful technique to investigate crystallinity and orientation of thin film. This method involves the using X-rays to identify the lattice parameters, lattice misfit, film/substrate orientation. In this research, the main geometry is a Bragg-Brentano geometry that employs a planar sample with incident Cu_K X-rays. In this geometry diffraction is from the out-of-plane oriented layers for thin film and substrate. The angle between diffracted and incident beam is proportional to the layer spacing. In principal, this geometry is used to gain rapid data with a small detector solid angle. The approach to define in-plane crystallographic for a thin film is more complicated which can be produced by adding a number of one-dimensional scans into a two-dimensional contour. The so-called “four circle geometry” is shown in Fig. 2.8. These circles refer to the four angles (χ , Φ , 2θ and Ω) that describe the relationship between the crystal lattice, the incident ray and detector. X-ray in the atoms can interact with electrons through both elastic and inelastic processes. If the sample has periodic atom arrangement and ordered lattice the measurements show sharp peaks which indicates the crystal structure. The condition for diffraction is given by Bragg’s Law:

$$2d \sin \theta = n\lambda \quad (2.5)$$

where: d = Interatomic spacing (nm)

λ = Wavelength of incoming radiation (nm)

θ = Angle of incident X-ray radiation (degrees)

n = Order of reflection (taken as one)

The lattice constant can be calculated by using d obtained from the Equa-

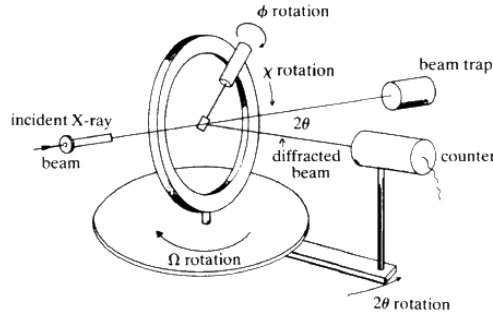


Figure 2.8: Schematic of 4-circle diffractometer [20].

tion 2.5. The position of the oscillations also defines the lattice constant, while the so-called 'Laue oscillations' and by following equation can be related to the thickness:

$$I \propto (\sin(2\pi N d \sin(\theta)/\lambda)) / (\sin(2\pi d \sin(\theta)/\lambda)) \quad (2.6)$$

where N is the number of diffracting thin film planes, and d is the spacing between planes [21]. This method is appropriate for thin films with smooth surface while using a conventional lab diffractometer. On the other hand, the X-ray reflectivity (XRR) measurement technique was carried out in this study to analyze X-ray reflection intensity curves from X-ray beam to determine thin film thickness. By using Bragg equation for two peaks the sample thickness can be calculated.

2.5.2 X-ray Reflectivity

X-ray reflectivity (XRR) is a technique often applied to thin film specimens as a means to measure the growth of the sample. It is capable for obtaining information such as layer thicknesses and interfacial roughness. By firing a beam of X-rays at a grazing angle onto the sample of interest, the reflection of these X-rays may be collected and then can calculate the scattering length density (SLD). SLD rises with the intrinsic scattering power and the physical density. For X-rays, the scattering arises from the electron density, whereas for neutrons, the scattering arises from the nuclear scattering lengths. SLD can be computed

from the scattering lengths and material densities. Specifically:

$$SLD = \frac{\sum_{i=1}^N b_i}{V_m} \quad (2.7)$$

where b is the scattering length contributions, N number of atoms within the unit cell, and V_m volume of the unit cell [22]. This equation can be used for ordered atom (crystalline) and also random arranged atoms (amorphous material) whereas V_m is the molecular volume.

Fig. 2.9 shows an example of a typical XRR curve (blue). Visible are Kiessig fringes, interference of the X-rays that reflect from the thin film interfaces in the sample. It displays as a decaying wave. From this it may be inferred that the interfaces are smooth, but otherwise quantitative analysis required fitting of the curve (red). By assigning values for layer roughness and thickness, a fit may be created [23].

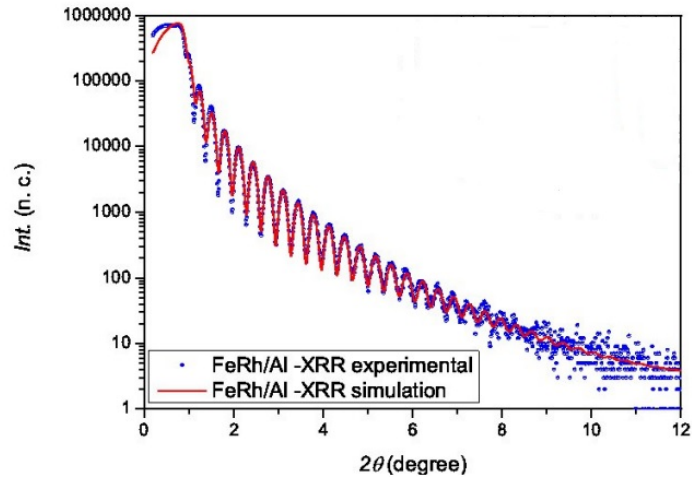


Figure 2.9: Example of a typical X-ray reflectivity curve with a fit applied [23].

2.6 Magnetic characterization

The following section determines the techniques which used in this study to measure static and dynamic magnetic properties of FeRh samples.

2.6.1 SQUID-magnetometer

Two different types of magnetometers have been employed to study volume-averaged magnetization: 1) a Superconducting Quantum Interference Device (SQUID - MPMS) magnetometer and 2) a Vibrating Sample Magnetometer (SQUID - VSM). These tools are different in measurements methods as well as the magnetic moment detection sensitivity, but both of them supply analogous information. Overall, a MPMS magnetometer is sensitive to small magnetic moments as (1×10^{-8} emu at 2500 Oe) and a VSM can identify larger magnetic moments more quickly ($< 10^{-6}$ emu with 1 second averaging capabilities) [24], [25].

This segment begins by explaining the main properties of a MPMS magnetometer and it is followed by describing functions of a VSM set up. The MPMS magnetometer carries out high sensitivity magnetization measurements through a complete sample volume. It is mainly important especially for investigating the magnetic properties of thin films which have less amount of material than bulk samples. The measurement in MPMS can accomplish in the range of 5 to 300 K and from 300 to 850 K with a precision of approximately 0.01 K and rates up to 10 K/min. Fig 2.10 illustrates a schematic diagram of MPMS set up [24], [25]. The MPMS magnetometer employed in this thesis involves three main components: superconducting detection coils, a superconducting magnet and a SQUID connected to the detection coils.

During the course of this thesis the new SQUID-VSM set up has been added to improve the magnetic measurements. In comparison SQUID-VSM has three advantages with respect to SQUID-MPMS. The helium liquid consumption in VSM is around 5 L per day that is much less than MPMS. On the other hand, by keeping same sensitivity the measurement speed in VSM is 5-6 times quicker than MPMS. In the end, cooling down in VSM from room temperature to 5 K takes less than 30 mins. Fig. 2.11 shows a basic process of detection for SQUID-

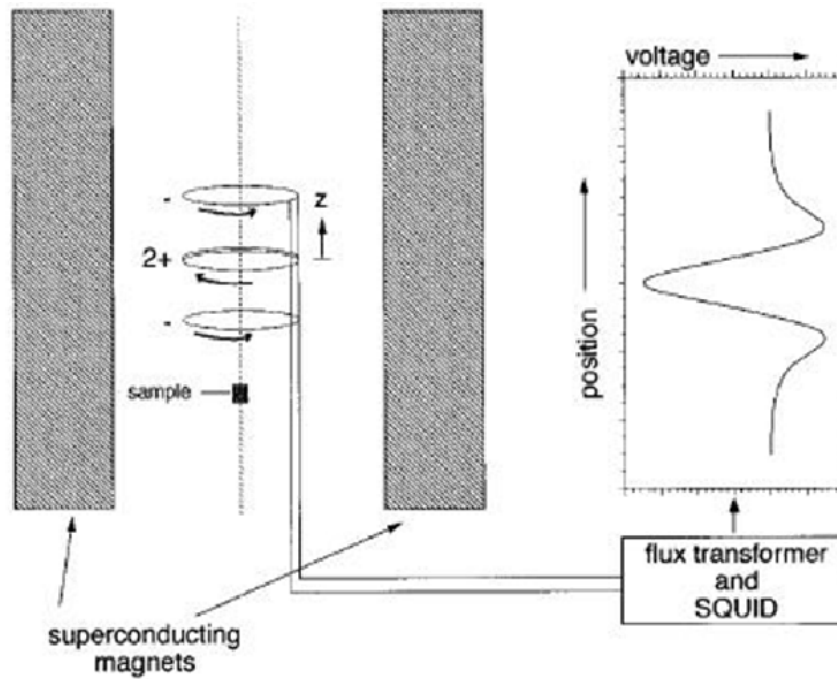


Figure 2.10: Schematic diagram of SQUID-MPMS set up [25].

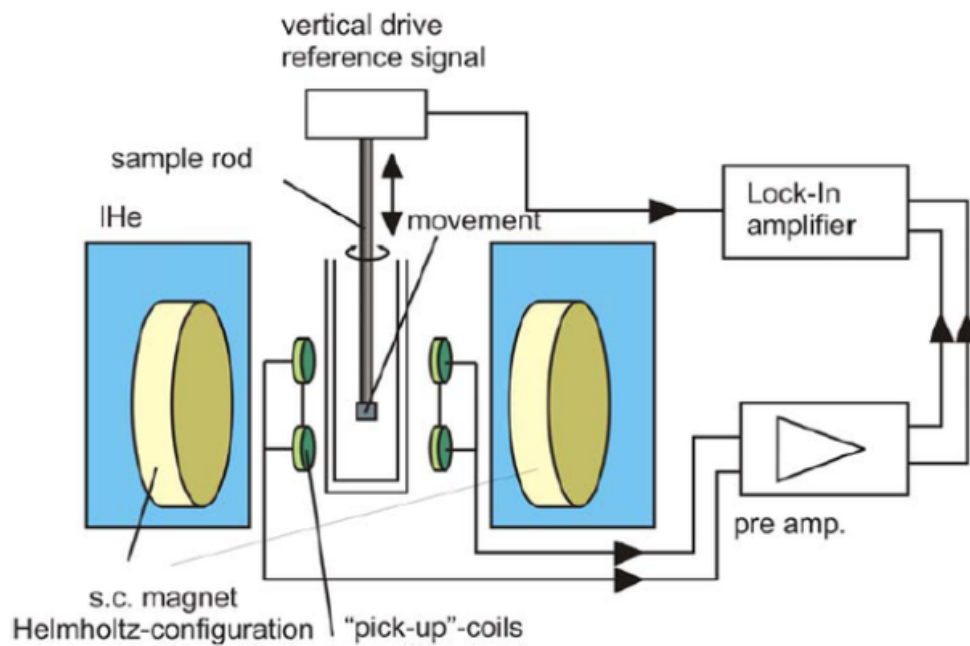


Figure 2.11: Schematic diagram of Quantum Design SQUIC-VSM system. The VSM measures the magnet moment by moving the sample between two pick-up coils [26].

VSM. In the VSM set up a second-order gradiometer has been located in the superconducting detection coils. The counter wound outer loop in the setup has main role to cancel the effect of linear magnetic field gradients. Thereby only the current induced via disturbances of consistent uniform magnetic field is measured. The position of the outer loop is in the center part of the detecting coils. This measured current should be convert to voltage which can be described by following equation:

$$V(t) = AB^2 \sin^2(\omega) \quad (2.8)$$

In this equation A is a scaling factor relating to the magnetic moment, B is the amplitude of vibration and ω is vibration frequency. A lock in amplifier is employed to separate the signal measuring at 2ω due to the $\sin^2(\omega) = 1/2 - 1/2(\cos 2\omega t)$ equation.

The data interpretation can be affected by some parameters such as vibration amplitude and frequency, measuring time, sample holder and sample geometry which are explained here. As a result of equation 2.8 the voltage depend on the vibration amplitude quadratically. Therefore, if the measured signal is weak the vibration amplitude must be increased. Concerning the vibration frequency, the copper detection coil vibrating sample magnetometers can be compared with SQUID-VSM. For VSM setup the variation of magnetic flux does not directly produce a signal. While it is employed to generate an input signal for the lock in amplifier to protect the signal from the tool artifacts. The frequency of vibration does not have any influence on the modifying the signal to noise ratio and also the signal strength. In case of presence a strong noise in the lab such as: mechanical or electromagnetic resonances, frequency adjustment can be useful to compensate the noise.

The time of measurement should be considered as an effective parameter when the measurement is very sensitive. On condition that the measured signal is less than $1 \times 10^{-9} \text{ emu}$ it is necessary to measure each data point over 100 seconds. While practically, the accuracy is about $1 \times 10^{-8} \text{ emu}$. Therefore if the signal is larger than $1 \times 10^{-8} \text{ emu}$, only 0.25 seconds per point is needed to have an accurate measurement [27]. Typical in this study it took 4 seconds to detect one data point. To have a precise measurement it is better to calibrate

the set up by measuring the sample holder which sometime makes an error in the measurement. There are two different kinds of sample holder, brass and quartz. In spite of the brass sample holder is easier to use, the quartz sample holder has more efficient for the sensitivity measurements. Another parameter which should be checked is sample geometry. In order to detect the correct data, geometry of the sample should be point-like. The size of sample bigger than reference sample causes more magnetic flux which is generated from the ends of sample. On the other hand, the sample which is smaller than reference makes higher response curve and produces a stronger magnetic moment. In this condition the counterwound detection coils remove the extra flux to decrease the magnetic moment.

2.6.2 Ferromagnetic Resonance

Ferromagnetic resonance (FMR) is a powerful technique to study the magnetization dynamics properties of an ensemble of atoms through the energy absorption of electromagnetic wave in the range of microwave frequency [28]. The essential difference between the static and dynamic of magnetization is the time scale while by applying an external magnetic field the magnetic system is perturbed. The equation of motion determines which precession occurs during the perturbation and it is depend on the sample properties.

To introduce the theoretical concept of magnetic dynamic it has worth to start with a simple model. All magnetic materials have magnetic moments μ . For a free atom μ is related to the total angular momentum \mathbf{J} . It is add of the orbital and spin angular momentum:

$$\mathbf{J} = \mathbf{L} + \mathbf{S} \quad (2.9)$$

According to the Pauli's exclusion principle, for two electrons which have overlapping wave functions, the lowest energy achieved while they have asymmetric wave functions. The exchange energy in the Heisenberg model with nearest neighbor spin S_i and S_j for two electrons can be expressed by:

$$E = -\frac{1}{2} \sum_{i < j} J_{ij} \mathbf{S}_i \mathbf{S}_j \quad (2.10)$$

Here J_{ij} is exchange integral. For ferromagnetic ordered $J_{ij} > 0$ which spin interactions lead parallel alignment. Due to the torque on the magnetic moment, applying an external magnetic field H leads to Zeeman splitting of the atomic energy levels. These differences between energy levels can be given by:

$$\Delta E_{ij} = g\mu_B \Delta m_{ij} \mu_0 H \quad (2.11)$$

In this equation, g is the Lande g-factor which the z-component of the total angular momentum can be declare in terms of g- factor [29, 30]. The required energy to transfer from state i to j is equal to $\Delta E_{ij} = \hbar\omega_{ij}$. \hbar is the reduced Planck constant. This energy can be supplied by resonant absorption of microwave energy. Because of the strict selection rules the transitions between states which $\Delta m_{ij} \neq \pm 1$ are forbidden. The torque induced by applied external magnetic field leads \mathbf{M} to precess around local \mathbf{H} so that the rate of changing \mathbf{M} is perpendicular to the plane crossed by \mathbf{M} and \mathbf{H} . Hence resonance condition can be fulfil by:

$$\omega = \gamma\mu_0 H \quad (2.12)$$

Where $\gamma = g | e | / (2m_{e-})$ which contains the electron mass m_{e-} and charge e . In a ferromagnetic ensemble, by substituting the external magnetic field by the effective field (\mathbf{H}) in Equation 2.12 the intrinsic ferromagnetic interactions which taking place during resonance can be explained [30, 31]. \mathbf{H} includes the internal field due to the anisotropy energy as well as the applied magnetic field. In this system the magnetization can change and start to precess by resonant excitation of transitions in the Zeeman multiplets or by tilting the effective field from the magnetization direction. This motion can be explained by the Landau-Lifschitz equation:

$$\frac{d\mathbf{M}}{dt} = -\gamma\mu_0 \mathbf{M} \times \mathbf{H}_{\text{eff}} \quad (2.13)$$

This equation shows the time dependency of changing \mathbf{M} induced by applied external magnetic field. As it is shown in Fig. 2.12(a) the precession of the

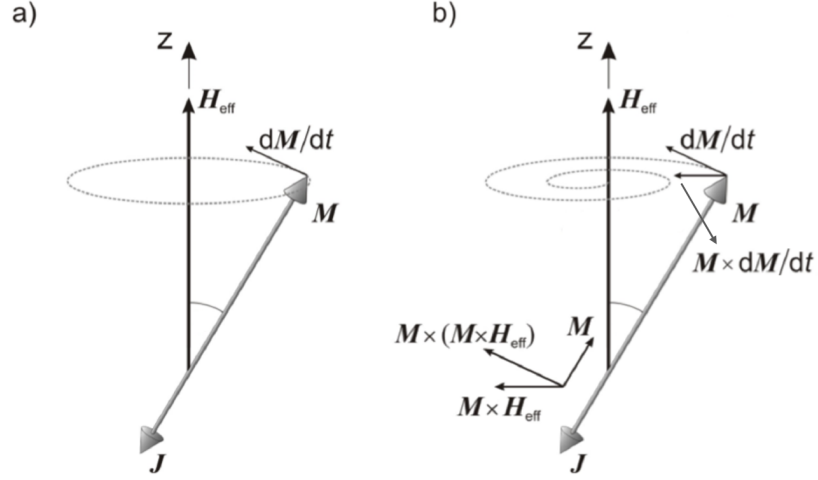


Figure 2.12: Precessional motion of magnetization around an effective field H_{eff} . (a) an undamped motion, (b) the magnetization pursues a helical pass described by Equation 2.15 .

angular momentum and the magnetic moment are clockwise and counterclockwise, respectively. It is because of the electron charge negative sign.

In this circumstance the magnetic moment precesses for infinity around the applied magnetic field at the constant angle which contradicts the reality. Landau and Lifschitz solved the problem by adding a damping component to Equation 2.13 which is pointing toward the equilibrium position (effective field). Since the length of \mathbf{M} is conservative the combination of $[\mathbf{M} \times \mathbf{H}_{eff}]$ and $[\mathbf{M} \times (\mathbf{M} \times \mathbf{H}_{eff})]$ vectors can describe the trajectory of the magnetic moment tip. Therefore Equation 2.13 can be written by new formulation [31]:

$$\frac{d\mathbf{M}}{dt} = -\gamma\mu_0\mathbf{M} \times \mathbf{H}_{eff} - \frac{\lambda_{LL}}{M_s^2}\mathbf{M} \times (\mathbf{M} \times \mathbf{H}_{eff}) \quad (2.14)$$

In this equation $\lambda_{LL} = 1/T$ which T is relaxation time. In this formula for large damping, precession is very fast. Therefore, Gilbert in 1955 [32] introduced a phenomenological as well as dimensionless damping term (α) to avoid of this problem:

$$\frac{d\mathbf{M}}{dt} = -\gamma\mu_0\mathbf{M} \times \mathbf{H}_{eff} - \frac{\alpha}{M_s}\mathbf{M} \times \frac{d\mathbf{M}}{dt} \quad (2.15)$$

Which is known as the Landau-Lifschitz-Gilbert (LLG) equation. By applying the damping term the magnetic moment tip purses a helical motion (see Fig. 2.12(b)). Under resonant excitation the damping term can be compensated by applying the microwavefield which leads to a precession of the magnetic moment at the eigenfrequency of the system. Usually the derivative of the microwave absorption is measured in the FMR set up. Lorentzian lineshape function is an appropriate model to determine the resonance position (H_{res}) as well as linewidth (ΔH_{res}) from the measured curve. As it is depicted in the Fig. 2.13 H_{res} and ΔH_{res} are defined at half maximum and peak-to-peak of the measured curve, respectively. Here H_{res} can be affected by some parameters such as: g-factor, anisotropy parameters, angles and magnetization while ΔH_{res} is proportional to the damping term.

In practical two techniques exist to fulfil the resonance condition: field and frequency swept techniques. In the field sweep technique a constant frequency is used while the external magnetic field is sweeping. In another technique, the microwave frequency is sweeping in the fixed external magnetic field. Fig. 2.14 illustrate the schematic diagram of the conventional X-band FMR experimental

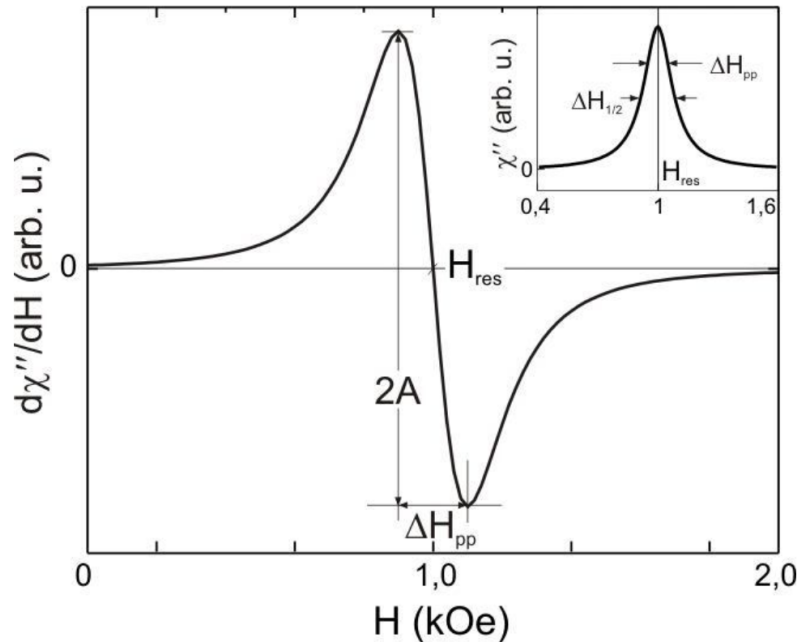


Figure 2.13: The measured curve has Lorentzian lineshape (insets) and the derivative of the microwave absorption. The magnetic field is swept [33].

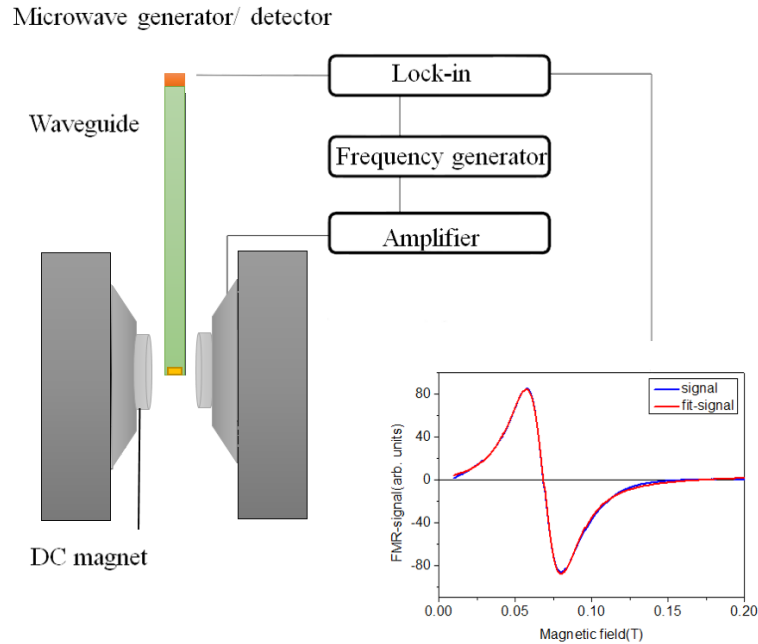


Figure 2.14: *The conventional X-band FMR set-up. The sample is located in the center of an external magnetic field which sweeps from 0 up to 2.1 T. A typical FMR line-shape is shown in the inset.*

set up which is in combination with a N_2 -based cryostat/heater. In this set up a sinusoidal wave of certain frequency f_{rf} is produced by a gun diode and spreads in a waveguide. The electromagnet generates the external magnetic field H and the end of waveguide is located between the electromagnet and yoke. The magnetic field is swept from 0 to maximum available value through the resonance condition while the rf-field is responsible to excite the sample magnetization. In this approach the diode detector probes the change of the wave energy which is reflected by the magnetic system via external magnetic field. Since the Signal-to-Noise ratio (SNR) in this technique is not sufficient to detect the sample signal, to allow a lock-in amplification the magnetic field is modulated. In principal the resonance condition is define by the relative direction of the sample magnetization and applied magnetic field H .

For the high-frequency description of the magnetic system especially g-factor and damping mechanism, the frequency dependent technique for measuring FMR can be used under UHV conditions [32, 34]. By this method the effects of exchange coupling and also inhomogeneous magnetization of a substance can be

characterized [35]. The scheme of frequency depend setup is depict in Fig. 2.15. “Thick (green) line: digital communication, dashed (red) line: analog signal, thin (orange) line: mw signal. A glass-to-metal adapter (G) is mounted to the main UHV chamber, while an electromagnet (B) can be positioned around it. A pair of coils (M) is mounted to modulate the external field. A mw synthesizer is connected via a circulator (C) to a mw feedthrough. The reflected mw power can be measured at the Schottky diode (SD) connected to a lock-in amplifier. The optimum measurement position is marked by the black square (P). The sample is fixed on the sample holder (S) “ [36]. Practically, the field swept technique is easier to use but it is limited to a thin frequency range. For a broad band microwave method in combinatrion with the Vector Network Analyzer (VNA): VNA-FMR approach can be used for both field and frequency sweep measurements.

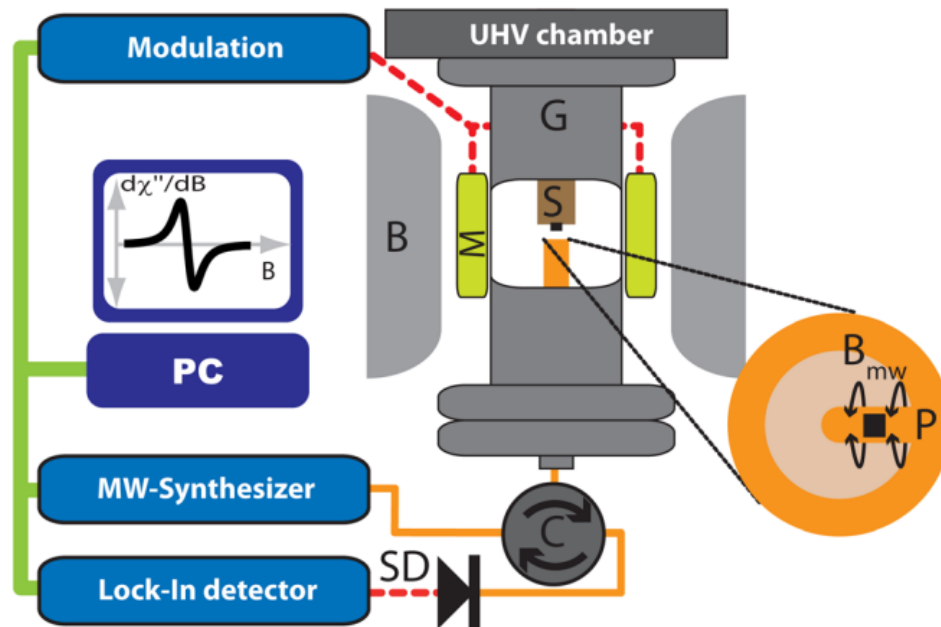


Figure 2.15: Schematic diagram of FMR set up in combination with a UHV system [36].

Bibliography

- [1] MBE setup manuscript, created by createc.
- [2] S. Maat, J. U. Thiele and E. E. Fullerton, “Temperature and Field hysteresis of the antiferromagnetic-to-ferromagnetic phase transition in epitaxial FeRh films”, *Physical Review B*, **72**, 214432, (2005).
- [3] S. Inoue, N. N. Phuoc, J. Cao, N. T. Nam, H.Y. Y. Ko and T. Suzuki, “Structural and magneto-optical properties of FeRh thin films”, *Journal of Applied Physics*, **103**, 07B312, (2008).
- [4] C. Stamm, J. U. Thiele, T. Kachel, I. Radu, P. Ramm, M. Kosuth, J. Minar, H. Ebert, H. A. Duerr, W. Eberhardt and C. H. Back, “Antiferromagneticferromagnetic phase transition in FeRh probed by x-ray magnetic circular dichroism”, *Physical Review B*, **77**, 184401, 2008.
- [5] M. Ohring, “The Materials Science of Thin Films”, 2nd ed.(Academic Press Inc., San Diego, 179401, (2002).
- [6] J. Musil and J. Vlcek, “Magnetron sputtering of films with controlled texture and grain size“, *Materials Chemistry and Physics*, **54**, 116 (1998).
- [7] K. Kato, Y. Abe and K. Asak, “Epitaxial Growth of (001)Rh Thin Film on (001)MgO Single-Crystal Substrate by Sputtering“ , *Japanese Journal of Applied Physics*, **44**, 7605, (2005).
- [8] Available in: <http://www.directvacuum.com/sputter.asp>.
- [9] R. S. Ohl, “Properties of ionic bombarded silicon”, *Bell System Technical Journal*, 31:104 122, (1952),

- [10] R. Bali, S. Wintz, F. Meutzner, R. Hübner, R. Boucher, A. A. 'Unal, S. Valencia, A. Neudert, K. Potzger, J. Bauch, F. Kronast, S. Facsko, J. Lindner, and J. Fassbender, "Printing Nearly-Discrete Magnetic Patterns Using Chemical Disorder Induced Ferromagnetism", *Nano Lett.*, **14**, 435-441 (2014).
- [11] J.F. Ziegler, J.P. Biersack, U. Littmark, "The Stopping and Range of Ions in Solids", Pergamon Press, New York, (1985).
- [12] J. Mayer M. Nastasi and J. Hirvonen, "Ion-Solid Interactions - Fundamentals and Applications", Bell System Technical Journal, Cambridge University Press, (1996).
- [13] J. M. Lommel, "Role of oxygen in obtaining complete magnetic first order transitions in FeRh films", *Journal of Applied Physics*, **40**, 1466-1467, (1969)
- [14] J. M. Lommel, "Magnetic and Electrical Properties of FeRh Thin Films", *Journal of Applied Physics*, **37**, 1483-1484, (1966).
- [15] J. M. Lommel, J. S. Kouvel "Effects of Mechanical and Thermal Treatment on the Structure and Magnetic Transitions in FeRh", *Journal of Applied Physics*, **37**, 1483-1484, (1966).
- [16] T. C. Kaspar, M. E. Bowden, "Structural characterization of epitaxial Cr_xMo_{1-x} alloy thin films", *J. Phys.: Condens. Matter*, **24**, 095001, (2012).
- [17] Available in: <https://www.jyu.fi/fysiikka/en/research/accelerator/abasedmat/research/characterizations/rbs>.
- [18] M. Prutton and M. El. Gomati, "Scanning Auger Electron Microscopy", University of York, York, UK, (2006).
- [19] Available in: <http://www.jeol.co.jp/en/science/am.html>. Auger Electron Ejection from an Atom.
- [20] Available in: <http://serc.carleton.edu/details/images/8400.html>

-
- [21] B. E. Warren, "X-ray Diffraction", Addison Wesley, Reading, MA., (1969).
- [22] L. A. Feigin and D. I. Averhun, "Structure Analysis by Small-Angle X-Ray and Neutron Scattering", New York, (1987).
- [23] C. L. Graiet, M. Vries, M. McLaren, R. Brydson, M. Loving, and C. Marrows, "Sputter growth and characterization of metamagnetic B2-ordered FeRh epilayers", J. visualized experiments, **80**, 8 (2013).
- [24] Available in: <http://www.qdusa.com/products/versalab.html>, 2013.
- [25] M. Loving, "Understanding the magnetostructural transformation in FeRh thin films", PhD Thesis, Northeastern University, (2014).
- [26] Available in: <http://wangli.info/vsm.html>
- [27] J. Stohr, and H. König, "Determination of Spin-Moment and Orbital-Moment Anisotropies in Transition-Metals by Angle-Dependent X-Ray Magnetic Circular-Dichroism", Physical Review Letters, **75**, 3748-3751, (1995)
- [28] B. Heinrich, "Radio frequency techniques-ferromagnetic resonance in ultrathin film structure", In Heinrich and J. A. C. Bland, editors, Ultrathin magnetic structure II. Springer Verlag, Berlin, (1994).
- [29] S. V. Vonsovskii, editor, "Ferromagnetic Resonance", Pergamon Press (1966).
- [30] K. Baberschke, "Investigation of Ultrathin Ferromagnetic Films by Magnetic Resonance", in "Handbook of Magnetism and Advanced Magnetic Materials", H. Kronmüller and S. S. Parkin, editors, John Wiley and Sons, Ltd. (2007).
- [31] L. Landau and E. Lifshitz, "On the theory of magnetic permeability in ferromagnetic bodies", Phys. Z. Sowjetunion , **8**, 153 (1935).
- [32] T. L. Gilbert, "A phenomenological theory of damping in ferromagnetic materials ", IEEE Trans. Magn. **40**, 3443 (2004).

- [33] Available in: <http://www.physik.fu-berlin.de/einrichtungen/ag/ag-kuch/research/techniques/fmr>.
- [34] I. Barsukov, F. M. Römer, R. Meckenstock, K. Lenz, J. Lindner, S. Hemken to Krax, A. Banholzer, M. Korner, J. Grebing, and M. Farle, “Frequency dependence of spin relaxation in periodic systems”, *Phys. Rev. B*, **84**, *140410(R)* (2011).
- [35] J. Lindner and M. Farle, “Magnetic anisotropy of heterostructures”, in *Advances and Perspectives in Spinstructures and Spintransport* (Springer, Berlin, **40**, *45-96* (2008)).
- [36] F. M. Römer, M. Moller, K. Wagner and et al, “ In situ multifrequency ferromagnetic resonance and x-ray magnetic circular dichroism investigations on Fe/GaAs(110): Enhanced g-factor“, *Appl. Phys. Lett.* **100**, *092402* (2012).

Chapter 3

Results and discussion

3.1 FeRh phase transition

An interesting feature of the FeRh system is that its magnetic and structural phase transition can be tuned in a variety of ways. In this section the parameters influenced the magnetic and structural properties of the FeRh alloy are discussed. The FeRh thin films prepared in the present work grew by means of MBE with thickness range of 5-40 nm. The first step to study the phase transition is to determine the phase transition temperature T_{tr} which is obtained by measuring the magnetization or the magnetic moment as a function of temperature. The result of this measurement is called the M-T curve, where the temperature is raised up to a value greater than T_{tr} (heating branch) and then lowered back to the initial temperature (cooling branch). Two phase transition occur during the heating of FeRh sample AFM-FM transition at T_{tr} and FM-PM transition at Curie temperature T_c .

3.1.1 Influence of annealing temperature

In this section, the magnetic phase transition dependence on the annealing process in $\text{Fe}_{50}\text{Rh}_{50}$ thin film with 35 nm thickness is investigated. RBS measurement was carried out with 1.7 MeV He^+ ions using to investigate the sample composition as shown in Fig. 3.1. The structure of the FeRh thin film annealed at 873 K, 973 K and 1123 K temperatures was determined by using XRD measurements and is depicted in Fig. 3.2. Since the sample annealed at 873 K was measured in a different XRD setup, its reference curves do not overlap with

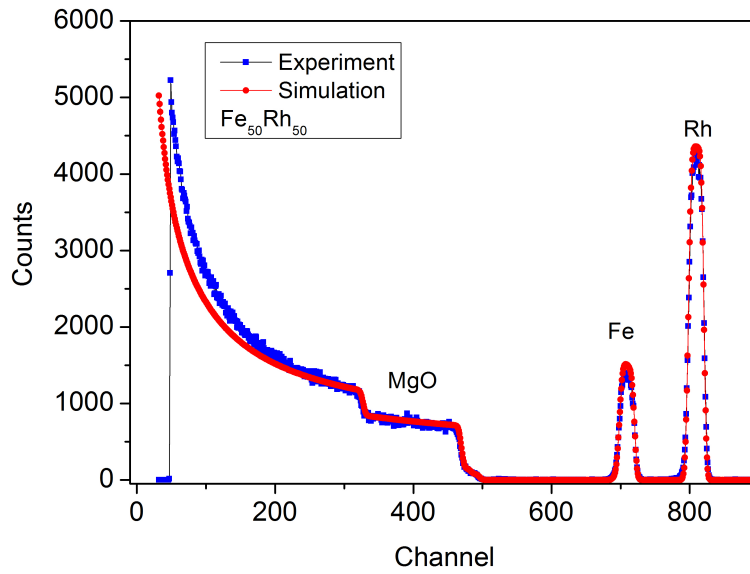


Figure 3.1: RBS measurement data and simulation of a 35 nm FeRh thin film. The composition is $Fe_{50}Rh_{50}$.

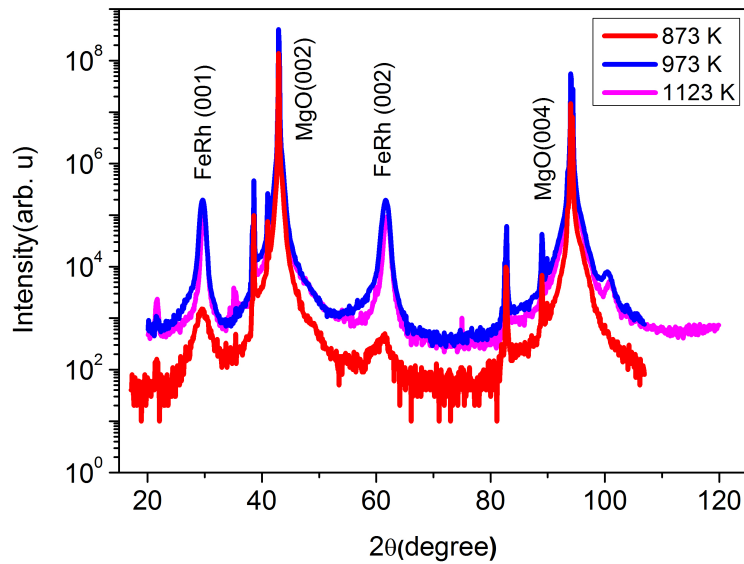


Figure 3.2: XRD patterns of $Fe_{50}Rh_{50}$ thin film on MgO substrate annealed at different temperatures.

the samples annealed at 973 K and 1123 K. Strong (001) and (002) FeRh peaks indicate that well oriented samples were obtained onto MgO(100) substrate after annealing above 873 K. These results indicate that a narrow orientation distribution of FeRh lattice and also better ordered growth of FeRh on MgO substrate can be obtained for samples annealed at 1123 K. Fig. 3.3 shows the measurement temperature dependence of magnetization at 150 Oe of FeRh thin film annealed at different temperatures. The as-grown sample does not reveal phase transition in temperature range 5-400 K because it has fcc structure, as reported by Lommel and Kouvel [1]. The influence of annealing temperature on the phase transition broadening is shown in Fig. 3.4 for samples annealed at 873, 973 and 1123 K. The magnetization measurements determine that the transition hysteresis becomes narrower, by increasing annealing temperature. This is likely because of improving the compositional inhomogeneity, chemical-order and reduced crystalline defects due to annealing the samples at higher temperature.

It is found that the AFM-FM phase transition temperature increases with increasing annealing temperature. The FeRh thin film annealed at 973 K and

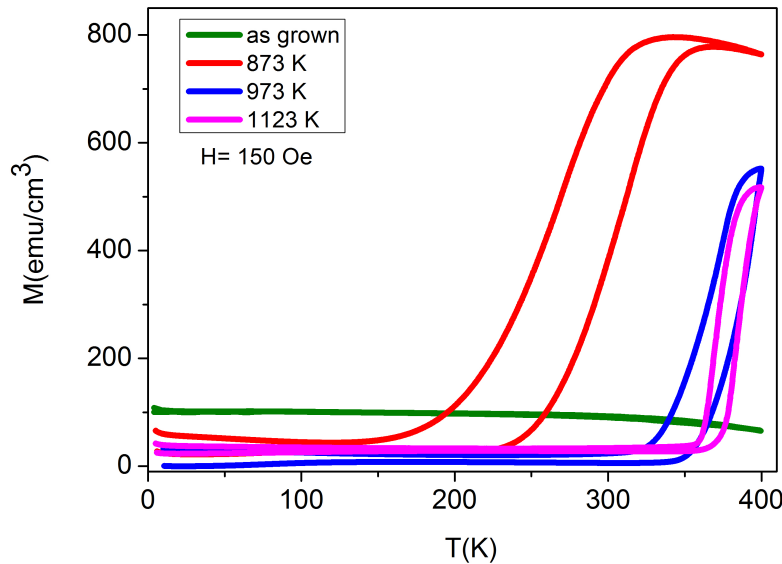


Figure 3.3: *Temperature dependence of magnetization at 150 Oe of $Fe_{50}Rh_{50}$ thin films annealed at different temperatures.*

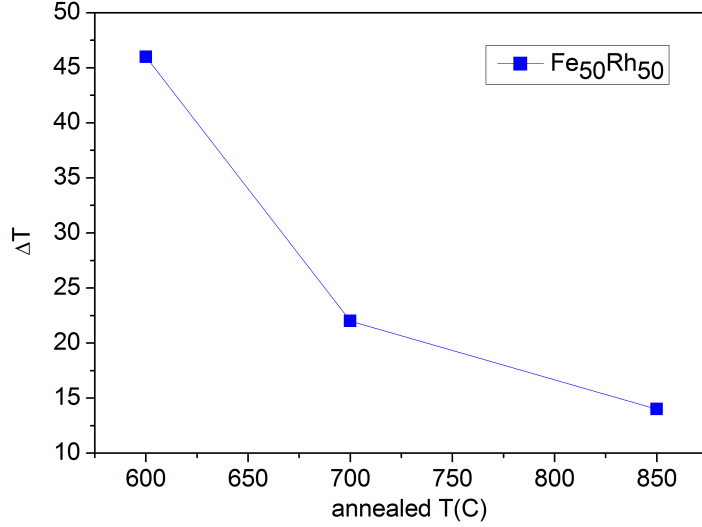


Figure 3.4: ΔT dependent annealing temperature for equiatomic FeRh thin film measured at an applied magnetic field of 150 Oe.

1123 K displays a sharp AFM-FM transition and small thermal hysteresis, which is similar to that in bulk FeRh ordered alloy crystals. Minor $M(T)$ loops were measured for 973 K and 1123 K annealed sample because of temperature limitation up to 400 K. Fig. 3.5 shows in-plane measured M-H loops of the FeRh thin film at (a) 5 K and (b) 400 K. The hysteresis loops at 5 K show the existence of residual magnetization at low temperature. Note that M-H loops measured at 400 K shows the lower M_s for the sample annealed at 1123 K than the sample annealed at 973 K, probably because the measurement temperature was limited to 400 K and the T_{tr} is higher for 1123 K annealed sample. The hysteresis loops during transition show an obvious opening at a higher magnetic field, although a slight asymmetry is found at an opposite field in the loops. The opening in the M-H loops occurs likely because of the combination of the weak magnetic anisotropy of AFM phase and the soft FM phase and also the magnetic-field-induced AFM-FM phase transition in FeRh thin film.

In summary, with increasing annealing temperature the AFM-FM transition temperature increases, while the thermal hysteresis width decreases. This may be because a high-temperature annealing process reduces the compositional fluc-

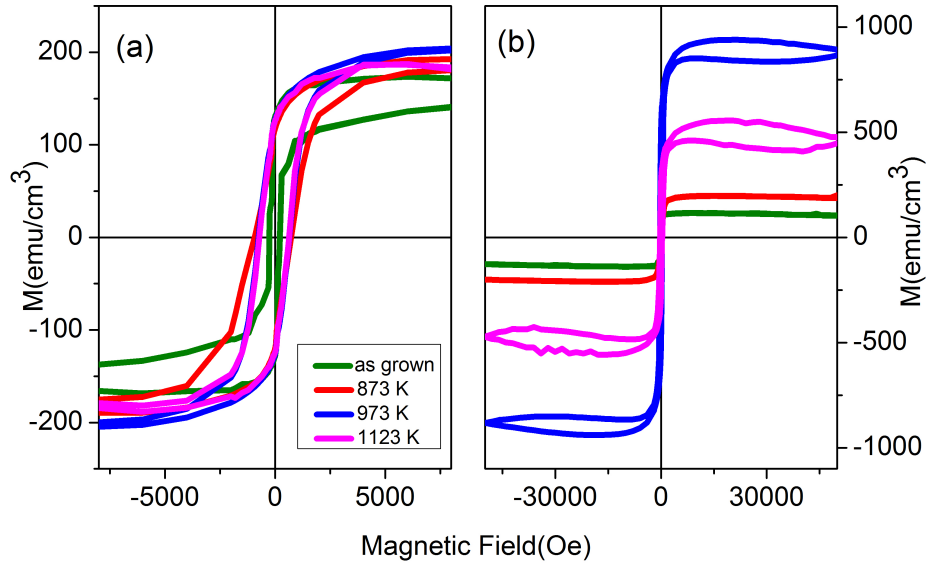


Figure 3.5: *M-H loops measured in the plane of $Fe_{50}Rh_{50}$ thin film (a) at 5 K and (b) at 400 K. The samples were annealed at different temperatures.*

tuation in the films. The M-H loops of the FeRh thin film annealed at 973 K and 1123 K display an opening at high magnetic fields which is indicative of the presence of both AFM and FM states during the phase transition.

3.1.2 Thickness-dependence

In the following section the influence of the film thickness on the magnetic properties and the magnetic configuration will be investigated. For this purpose $\text{Fe}_{50}\text{Rh}_{50}$ thin films with different thickness were grown on MgO substrate annealed at 600/800/850 ° for 2/2/4 h by means of MBE. Fig. 3.6 shows temperature-dependent magnetization (M-T) for 5, 9, 26 and 35 nm thick FeRh thin film in the presence of a magnetic field of 150 Oe. Note that 9 and 26 nm thick samples were measured by SQUID-MPMS that the measurement temperature was limited to 380 K. All of thin films clearly display the phase transition from AFM to FM phase. As visible in Fig. 3.6 by decreasing thickness T_{tr} decreases particularly for samples with thickness below 10 nm. The more sharp AFM to FM transition is observed for thicker films, which is in agreement with work [2] where the sharp phase transition was reported only for FeRh thin films with thickness above 14 nm. On the other hand the transition becomes much broader for the FeRh thinner films. This broadening is associated to the grain size reduction in the thinner films [3].

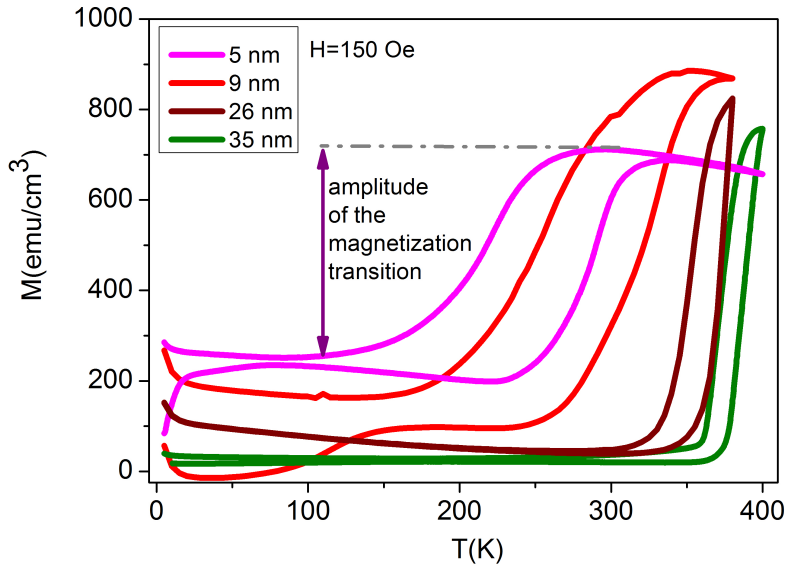


Figure 3.6: Temperature dependent magnetization of thin films with various thickness measured at an applied field of 150 Oe.

When the thickness decreases from 9 nm to 5 nm, the grain size decreases significantly, which corresponds to the significant increase in the transition width and residual magnetization (M_{rs}) as shown in Fig. 3.6. This can be understood from the surface/interface effect as the surface area increases with decrease of the grain size. For ultrathin films with a thickness of 10 nm or below, a large M_{rs} is generally observed which the origin has not yet been completely understood [4]. The instability of the AFM structure when the amount of the site-exchange defect density exceeds a threshold of 0.8%/f.u. (f.u.: formula unit) [5] and also a formation of the FM Fe-rich α' -phase and the paramagnetic Rh-rich γ -phase due to slow diffusion rate of Rh in the thin films are suggested [3]. In particular, M_{rs} is more visible for thin FeRh sample with thickness below 10 nm because of the small difference between M_{rs} and amplitude of the magnetization transition. From Fig. 3.7 one can extract another piece of useful information from the M-T measurements by plotting the thickness dependence the phase transition temperature. It is visible that the phase transition temperature decreases with decreasing FeRh thin film.

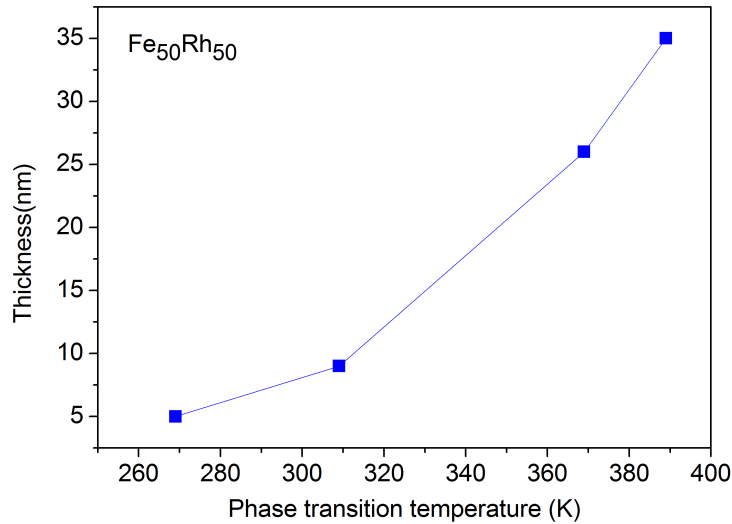


Figure 3.7: *FeRh thin film thickness dependent phase transition temperature measured at an applied magnetic field of 150 Oe.*

Fig. 3.8 shows the magnetization curves of the same samples measured at 5 K. It is noticeable that the coercivity decreases with decreasing film thickness. Magnetization saturates at a field of less than 1500 Oe. Fig. 3.9 gives the saturation magnetization of the films obtained at 5 K. It is obvious that M_s increases as the thickness decreases from 9 nm to 5 nm. This implies that in FeRh thin films, the lattice mismatching induced stress should not be a main factor for formation of the FM phase, since the stress must delay the onset of AFM-FM transition, i.e., there should be an increase in the T_{tr} instead of the decrease observed here. This magnetization reduction is ascribed to the grain size induced FM instability and the magnetic moment reduction of Fe and Rh spins at the interface. When the thickness decreases the grain size decreases significantly which corresponds to the significant increase in the transition width and M_{rs} [3]. The AFM-FM transition is observed at a thickness as low as 5 nm.

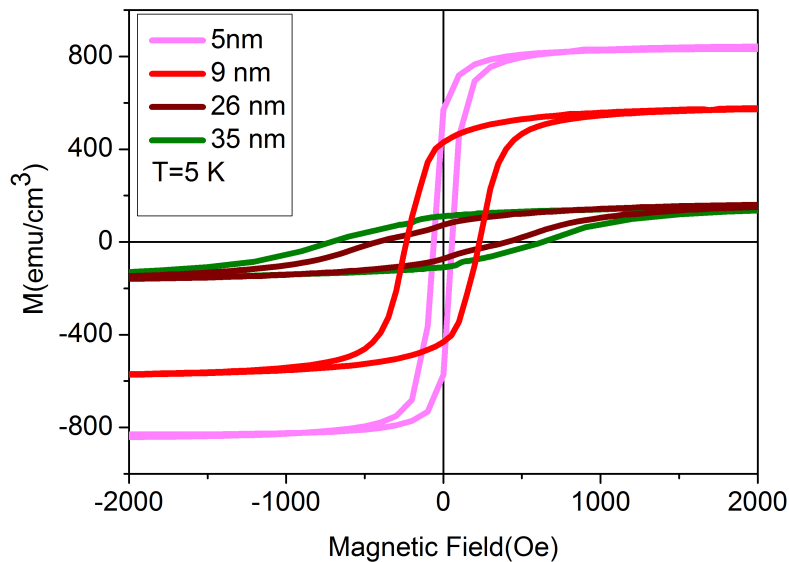


Figure 3.8: Magnetization curves measured at 5 K for various thicknesses, showing large residual magnetization increase when the thickness of film is reduced to less than 9 nm.

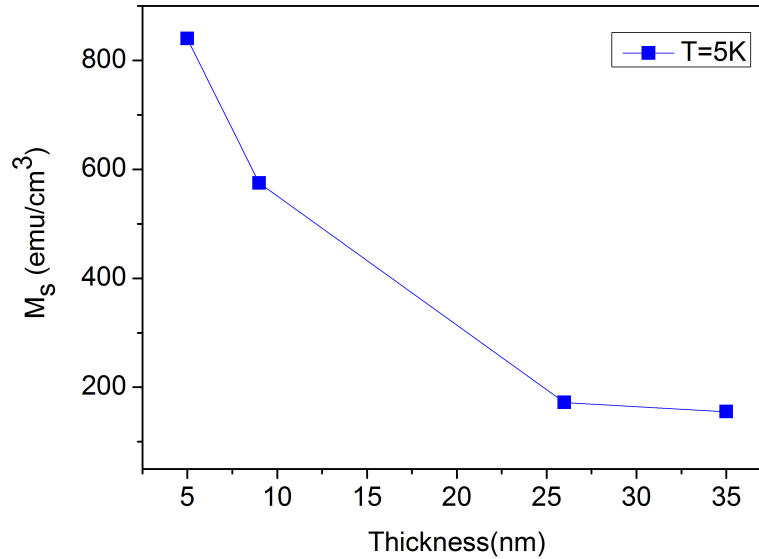


Figure 3.9: Saturation magnetization M_s obtained at 5 K, showing different M_s variations when the film thickness is reduced from 26 to 9-5 nm .

Fig. 3.10 depicts XRR measurement (blue) and fitted (red) for an FeRh film, with expected thickness of 35 nm. Fig. 3.11 shows Scattering Length Density (SLD) through XRR fitting by using GenX software package. SLD calculation shows a gradient near the interface of the FeRh thin film and MgO substrate which shows more Rh concentration in this region and low Rh concentration in the inner layers. The evaluation of the low energy AES measurement for 34 nm thick $\text{Fe}_{50}\text{Rh}_{50}$ with 4 nm Rh capped layer is shown in Fig. 3.12 . The ratio between the AES signal of Fe and Rh as a function of depth is shown in Fig. 3.13. It shows a drop of the Fe/Rh ratio by 5% at the interface between MgO and film with about 3-4 nm thick Rh-rich region. The bulk part of the film has almost homogeneous composition. Above of the Rh-rich region there is very thin Fe-oxide region. Both measurements confirm the formation of mixture of the equiatomic region and Rh-rich region at the interface of two different samples. Therefore can be suggested that the Rh-enrichment in the interface between sample and substrate is a general property of the FeRh system. Altogether, it can be said that the magnetization measurements show the AFM phase becomes more and more unstable as the thickness decreases and T_{tr} shifts to lower

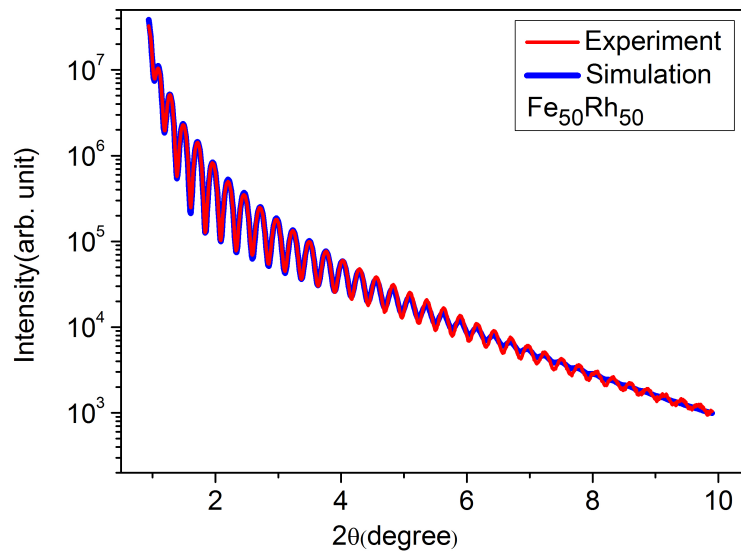


Figure 3.10: *Experimental and simulated fit for an X-ray reflectivity curve for an FeRh film with 35 nm thickness.*

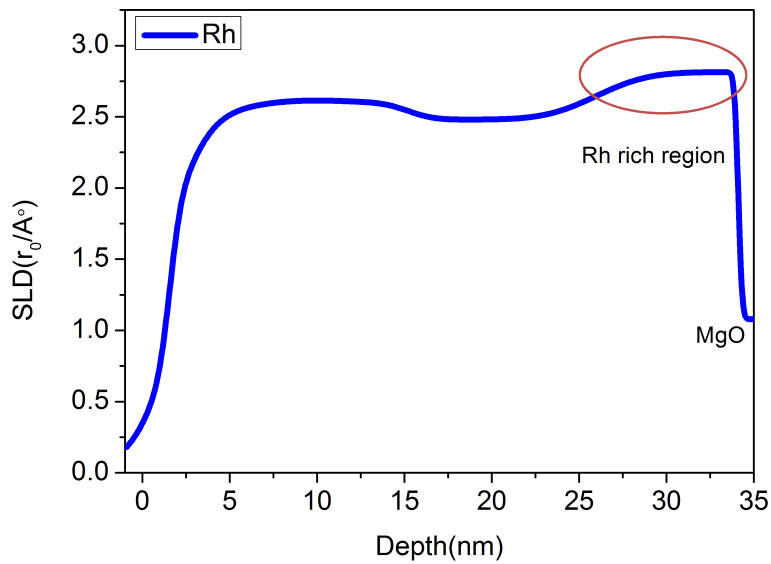


Figure 3.11: *Scattering length density (SLD) profile of Rh concentration in Fe₅₀Rh₅₀ with 35 nm thickness and by using XRR data was calculated by Dr. E. Josten.*

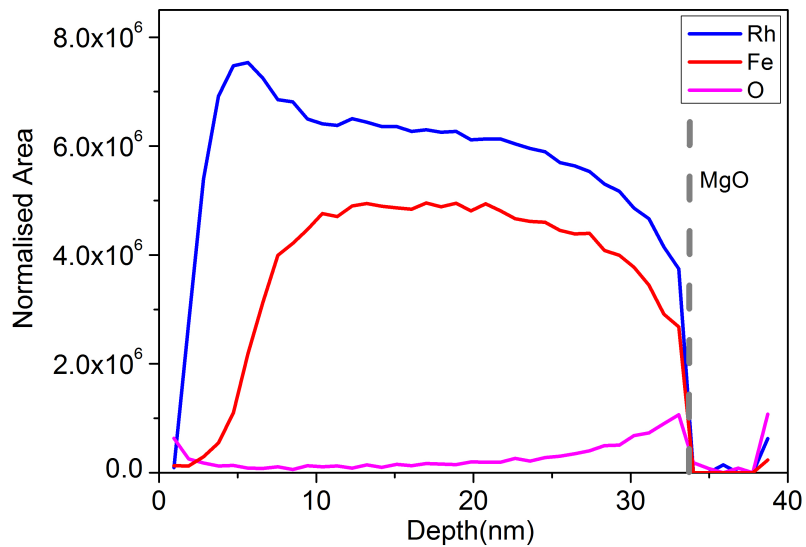


Figure 3.12: Evaluation of the low energy AES measurement for 34 nm thick $Fe_{50}Rh_{50}$ with 4 nm Rh capped layer measured by Dr. S. Facsko.

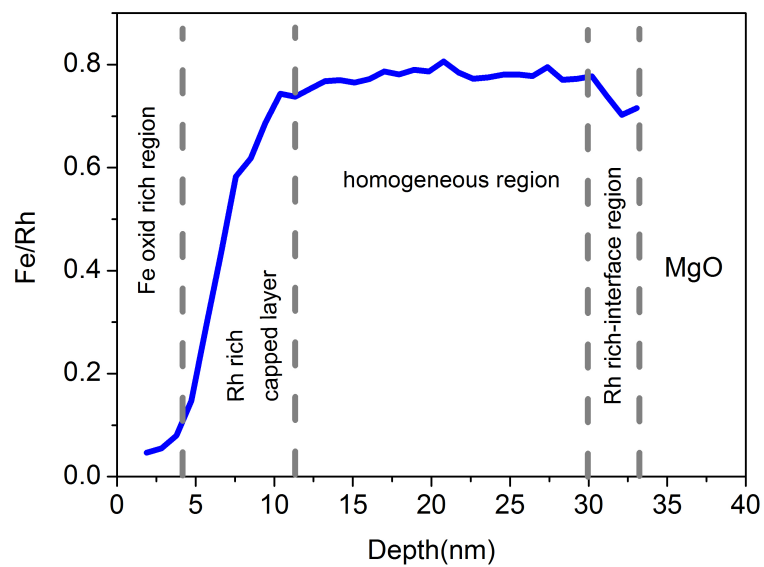


Figure 3.13: The ratio between the AES signals of Fe and Rh as a function of depth for 34 nm thick $Fe_{50}Rh_{50}$ with 4 nm Rh capped layer.

temperatures. The FM phase could be stabilized by a magnetic field when the FeRh film thickness is reduced below 10 nm. Moreover, the lattice mismatching and grain size have dominant roles to shift the T_{tr} and also formation of M_{rs} below the phase transition.

3.1.3 Effect of chemical composition

The magnetic properties of $\text{Fe}_x\text{Rh}_{100-x}$ with $44 \leq x \leq 55$ grown on MgO (100) substrates as a function of composition and annealing temperature were systematically studied in this section. The samples studied in this section were the thin films of FeRh with nominally 40 nm thickness. The list of samples and magnetic properties are summarized in table. 3.1

To determine how the phase transition depends on iron and rhodium content, FeRh thin films were grown by different composition under the same conditions. Fig. 3.14 depicts the temperature dependence of magnetization for (a) as-grown samples, (b) annealed at 873 K and (c) annealed at 973 K under an applied magnetic field of 150 Oe at the temperature range from 5 to 400 K. The as grown thin films with $44 \leq x \leq 53$ composition are nonmagnetic because of their fcc structure, as discussed in the previous section. However for $x=55$ composition, thin film behaves ferromagnetic. For annealing temperature at 873 K, thin film with $44 < x < 50$ compositions, show only poor signal of AFM-FM transition while sample with $x=50$ shows phase transition at about 300 K. The samples with $x > 50$ behave as ferromagnetic across in the temperature range from 5 to 400 K (Fig. 3.14(b)). For annealing temperature at 973 K similarly thin films

Table 3.1: List of the FeRh thin films with 40 nm thickness and different composition annealed at 973 K.

| Sample No | Fe % | Rh % | T_{tr} (K) | M_s (at 5K) | M_s (at 400K) |
|-----------|------|------|--------------|---------------|-----------------|
| 1 | 44 | 56 | – | 220 | 470 |
| 2 | 46 | 54 | – | 240 | 525 |
| 3 | 50 | 50 | 385 | 155 | 945 |
| 4 | 51 | 49 | – | 845 | 955 |
| 5 | 52 | 48 | – | 890 | 965 |
| 6 | 53 | 47 | – | 1010 | 968 |
| 7 | 55 | 45 | – | 1130 | 985 |

with $44 < x < 50$ composition, show partial phase transition. As visible from Fig. 3.14(c) the $\text{Fe}_{50}\text{Rh}_{50}$ thin film annealed at 973 K shows AFM-FM phase transition at 375 K. For samples with $51 \leq x \leq 52$ a clear sign of AF phase is already observed at lower temperatures. For samples with $x > 52$ there is no evidence of phase transition and thin film behaves as ferromagnetic.

The magnetic phase diagram of the $\text{Fe}_x\text{Rh}_{100-x}$ system in Fig. 3.14 showed that slight differences in the Fe concentration lead to drastic changes of the magnetic behavior, in particular for Fe concentrations around $x \sim 52$.

Fig. 3.15 (a) and (b) shows the saturation magnetization of the same samples measured at 5 K and 400 K, respectively. Magnetization saturates at a field of less than 5000 Oe. For as-grown samples M_s increases monotonously as the Fe composition increases from 44 to 55 %. For samples annealed at temperature 873 K, M_s increases as Fe concentration increases up to 50 percentage in FeRh thin film, while for $x > 50$, there is a slight decrease in M_s for both temperatures 5 and 400 K. Similarly to the as-grown samples, for samples annealed at 973 K M_s increases as the Fe composition increases. At 5 K the magnetization (M_s) increases sharply with increasing Fe concentration $x > 50$, while for 400 K the growth of M_s is not such significant. In conclusion, the first-order phase transition occurs over the range of $44 \leq x \leq 50$ of $\text{Fe}_x\text{Rh}_{100-x}$ thin films. The phase transition from AFM to FM takes place for samples annealed at 873 K and at 973 K. The composition range of thin films which exhibit the transition is wider, as compared to bulk [6] and will be discussed later. Note that T_{tr} decreases with increasing Fe concentration for heating as well as cooling processes.

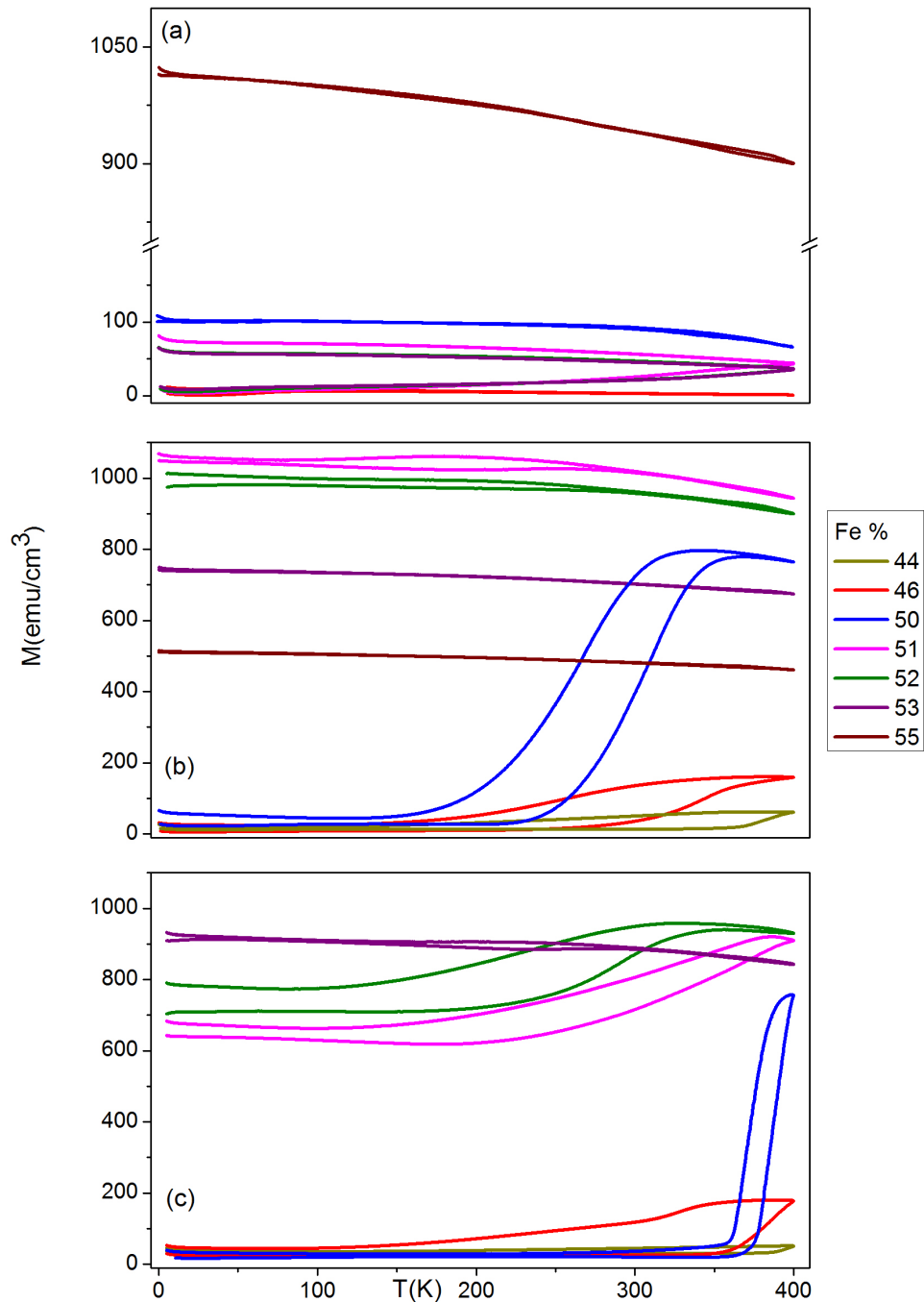


Figure 3.14: Temperature-dependent magnetization of $\text{Fe}_x\text{Rh}_{100-x}$ thin films in the composition range of $44 \leq x \leq 55$ under the magnetic fields of 150 Oe (a) as-grown, (b) annealed at 873 K and (c) annealed at 973 K.

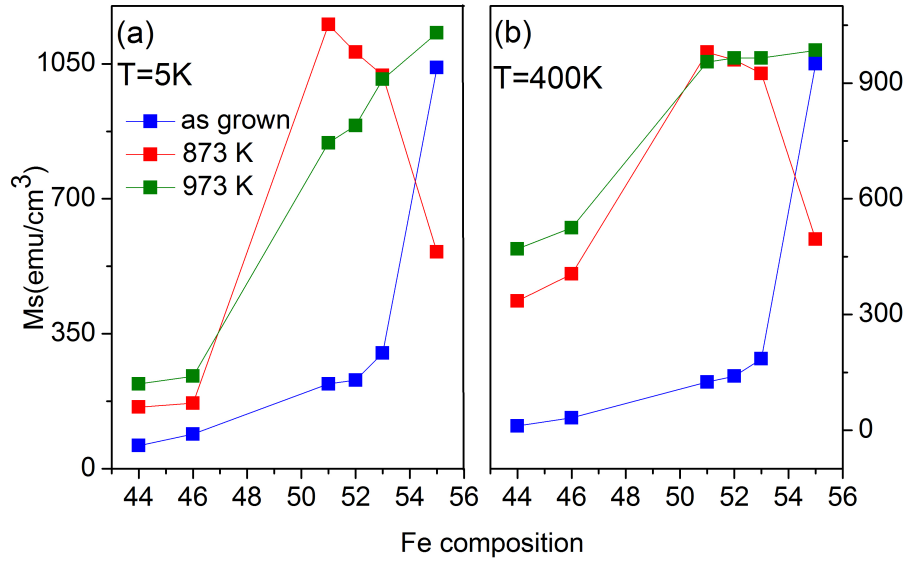


Figure 3.15: Saturation magnetization of as-grown, 873 K and 973 K annealed FeRh thin films measured at (a) 5 K and (b) 400 K.

3.1.4 Magnetic field dependence

Since the first-order magnetic phase transition is expected to be sensitive to magnetic field applied during the course of transition a careful experiment was performed in present study. The magnetic field was being applied during heating and cooling, the magnitude of which was changed from 150 Oe to 60 kOe. For the $\text{Fe}_{50}\text{Rh}_{50}$ thin film with 35 nm thickness magnetization-temperature curves with different applied magnetic fields, 150 Oe, 10, 20, 40 and 60 kOe are shown in Fig. 3.16. The external magnetic field is applied along the film plane. It is found that the magnetization-temperature curves are shifted to a lower temperature as the applied field is increased. The evaluation of the T_{tr} with increasing an applied magnetic field shows a similar trend as compared to reference [6]. This suggests that the external magnetic field favors the alignment of magnetization and stabilization of FM phase. Therefore AFM-FM T_{tr} shifts to lower temperature.

The magnetic behavior of virgin MgO substrate is shown in Fig. 3.17 which demonstrates that the negative slope in the FeRh M-T curve is a result of a

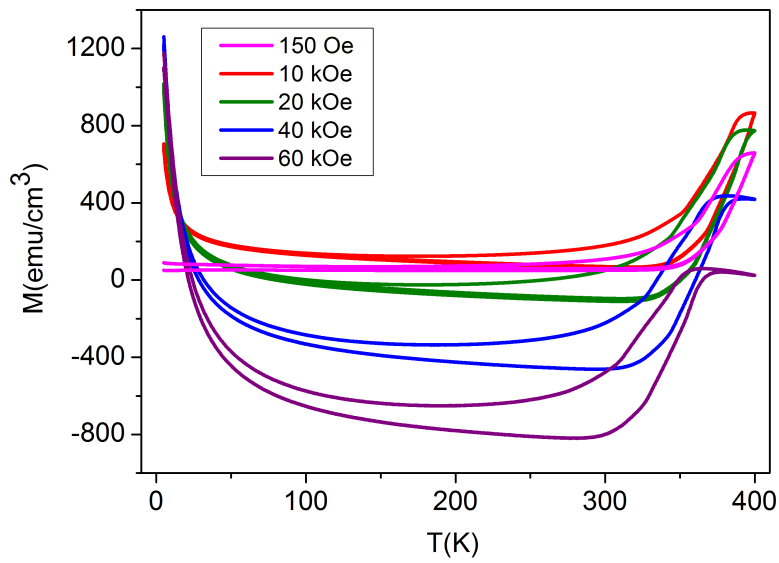


Figure 3.16: Temperature-dependent magnetization of $\text{Fe}_{50}\text{Rh}_{50}$ thin films under the applied in-plane magnetic fields of 150 Oe, 10, 20, 40, and 60 kOe, respectively.

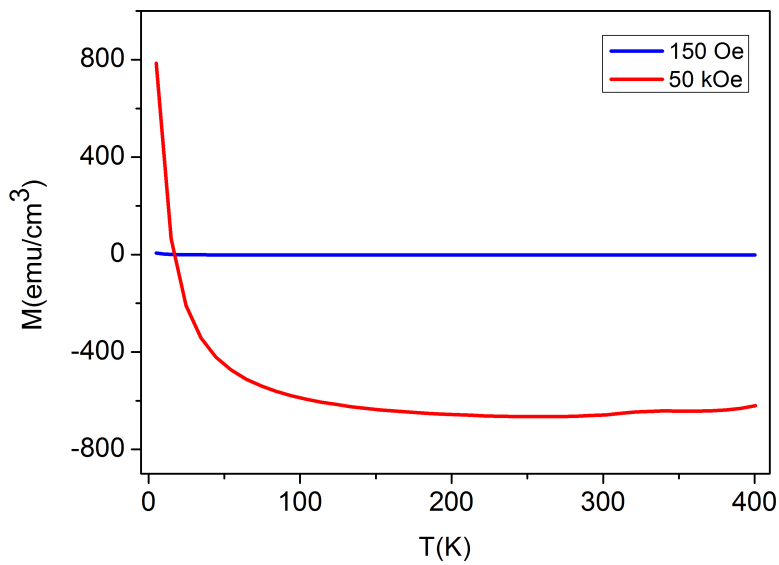


Figure 3.17: Temperature-dependent magnetization of virgin MgO substrate under the applied magnetic fields of 150 Oe and 50 kOe.

strong diamagnetic background from the MgO substrate impurities. Note that by increasing the applied magnetic field the contribution of the background signal increases dramatically.

3.2 Ferromagnetic resonance

As mentioned already, the first order magneto-structural phase transition for FeRh system evolves via nucleation and growth of both, FM and AFM phase across the transition. To get insight to details of the transition process, it is desirable to investigate the nucleation and growth of both phases within the first order phase transition. This, however, requires methods that are capable of separating the responses from the different regions or that are susceptible to different local magnetic environments. Conventional magnetometry suffers in this context from not being able to resolve such differences, especially for ultra-thin films which exhibit a much broader phase transition with a huge offset in the AFM phase [3]. Experimental methods that are based on exciting the magnetic system are advantageous in this aspect, since the dynamic response between AFM and FM regions (or FM regions in contact to AFM ones and vice versa) can lead to significant differences in the signal. A method well suited to investigate magnetic thin films with different local magnetic properties is FMR. It is interesting to note that in spite of the recent extensive interest on the FeRh alloy system, up to now very few studies have been carried out by means of FMR through a narrow interval temperature [7].

In this section the width and position of the FMR resonance line as a function of temperature dependent across the phase transition in ordered polycrystalline FeRh thin films, which were grown on MgO substrates by MBE and magnetron sputtering are study. In addition frequency dependent-resonance field is probed in the FM phase at a constant temperature. In particular, the nucleation and growth of AFM and FM phases in the matrix of the FeRh thin films is probed during heating and cooling and compared to magnetometry data obtained from the same samples up to the T_c . It is interesting to investigated the magnetic response of thin films with thickness below 10 nm add of films with thickness of about 33 nm. Since a requirement for implementing the FeRh system into the

field of nanomagnetism is that meso- or nano-structures of FeRh retain their properties with respect to the first order phase transition. Investigating the thin film limit is one step towards this aim and has been assumed to rather less extend in literature [3]. As it is visible in Fig. 3.18 temperature-dependent magnetization for non-capped Fe₅₀Rh₅₀ shows an opening during heating and cooling. It is likely due to the oxidation in the course of magnetization measurement at high temperature. Therefore, to study the FMR in FeRh system capped thin films were grown.

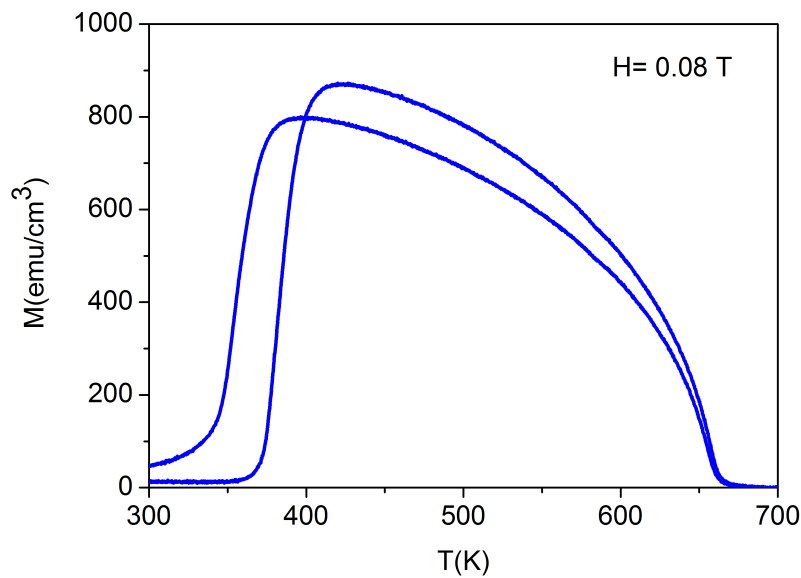


Figure 3.18: *Temperature-dependent magnetization of non capped Fe₅₀Rh₅₀ thin films at $H=0.08$ T upon heating and cooling.*

3.2.1 FMR study of FeRh thin film

In the following chapter static and dynamic magnetic properties of FeRh thin films with different thicknesses, prepared by MBE and sputtering methods are investigated as resulting from SQUID and FMR measurements. In the first a 33 nm thick thin film, which magnetically exhibits bulk-like properties is discussed. It was chosen for easy comparison to already known results, as this thickness regime is a commonly used in studies of sputtered FeRh film. For that 33 nm thick $\text{Fe}_{50}\text{Rh}_{50}$ (001) thin film was grown by means of MBE on MgO (001) single-crystal substrates. After annealing up to 1123 K the sample was capped with 4 nm Rh to avoid of oxidation. The composition of the thin films were determined via RBS and the crystal structure was studied by using XRD in a θ - 2θ scan as discussed already in the section 3.1.1.

In Fig. 3.19 (a) the saturation magnetization M_s as function of T curve for the 33 nm thick film in a temperature interval of 300-700 K is presented. In this wide temperature range all magnetic phases can be distinguished. Below the Curie temperature of $T_c = 670$ K the system becomes ferromagnetically coupled, until the antiferromagnetic phase transition starts at about $T_s = 435$ K. The hysteretic transition is completed at $T_e = 345$ K. For lower temperatures a small residual ferromagnetic response is left, which does not vanish even well below the transition temperature. As known from literature [8], atomic distances are crucial for magnetic coupling in FeRh, so the remaining ferromagnetism may be induced by interlayer strain origination from the interface to the substrate. The thin film exhibits a hysteretic variation of M_s as function of temperature, indicating the existence of the first order phase transition.

Due to the fact that SQUID magnetometry provides only access to the static integral saturation magnetization of the system the same sample pieces were used by means of FMR setup which described in chapter 2. In the following it will be explained the results from measurement performed on the 33 nm film and in the next section compare those with the 8 nm one. To start the measurements in a well-defined FM state, a high temperature of 602 K was chosen, as indicated by the pink dot in Fig. 3.19 (a). The corresponding FMR spectrum in Fig. 3.19 (b) shows a resonance signal at around 100 mT. It should be noted that due to modulating the external field the derivative of the absorption line is detected.

With increasing temperature the resonance fields approach the paramagnetic resonance field, being the resonance field for zero magnetization and anisotropy, while by reducing the temperature the linewidth extend and finally FMR signal disappears below the phase transition. Although the system according to the magnetometry results is in a FM phase at 602 K, the resonance line clearly exhibits an asymmetry in the signal shape. Comparing the signal shape to the high temperature measurement done on the 8 nm film (Fig. 3.23 (b)), this asymmetry can be attributed to a superposition of two independent FMR-signals at slightly different resonance fields. In fact, due to the much smaller linewidth in the thinner film (see Fig. 3.19 (b)), it is possible to unambiguously identify these two resonance lines. A fitting routine including two signals to the experimental data of the 33 nm film, a good agreement is observed (insets in Fig. 3.19(b)).

Note that in principle asymmetric resonance signals might also result from intrinsic deviations of the symmetric Lorentzian profile expected in ultrathin films. In case that the film thickness becomes larger than the penetration depth (skin depth) of the microwave in resonance deviations from a symmetric line-shape are obtained [9].

This penetration depth depends on microwave frequency, the conductivity of the material and-in our case even more importantly-on the magnetic permeability. The latter is proportional to the magnetic susceptibility which is the quantity actually probed by FMR. Thus, at constant frequency it strongly depends on the external magnetic field and on-resonance obtains much larger values than off-resonance. The strong absorption of microwaves on-resonance results in a significant reduction of the skin depth at FMR. For a bcc Fe film excited at a microwave frequency of 9 GHz the skin depth at FMR is about 40 nm [10]. Considering that our film are irradiated from both sides (the MgO substrate being practically transparent for microwaves) within the microwave cavity, and taking into account that two lines are obtained also for the 8 nm thick sample, an asymmetry due to inhomogeneous microwave distribution is rather ruled out. In turn the observation of two signals suggests that there are two areas of slightly different magnetic properties inside the film. For verifying this hypothesis, AES and XRR measurements were performed, which were shown in section 3.1.1. Both measurements consistently indicate the presence of a Rh-rich (% 5) region near the substrate interface having a thickness of about

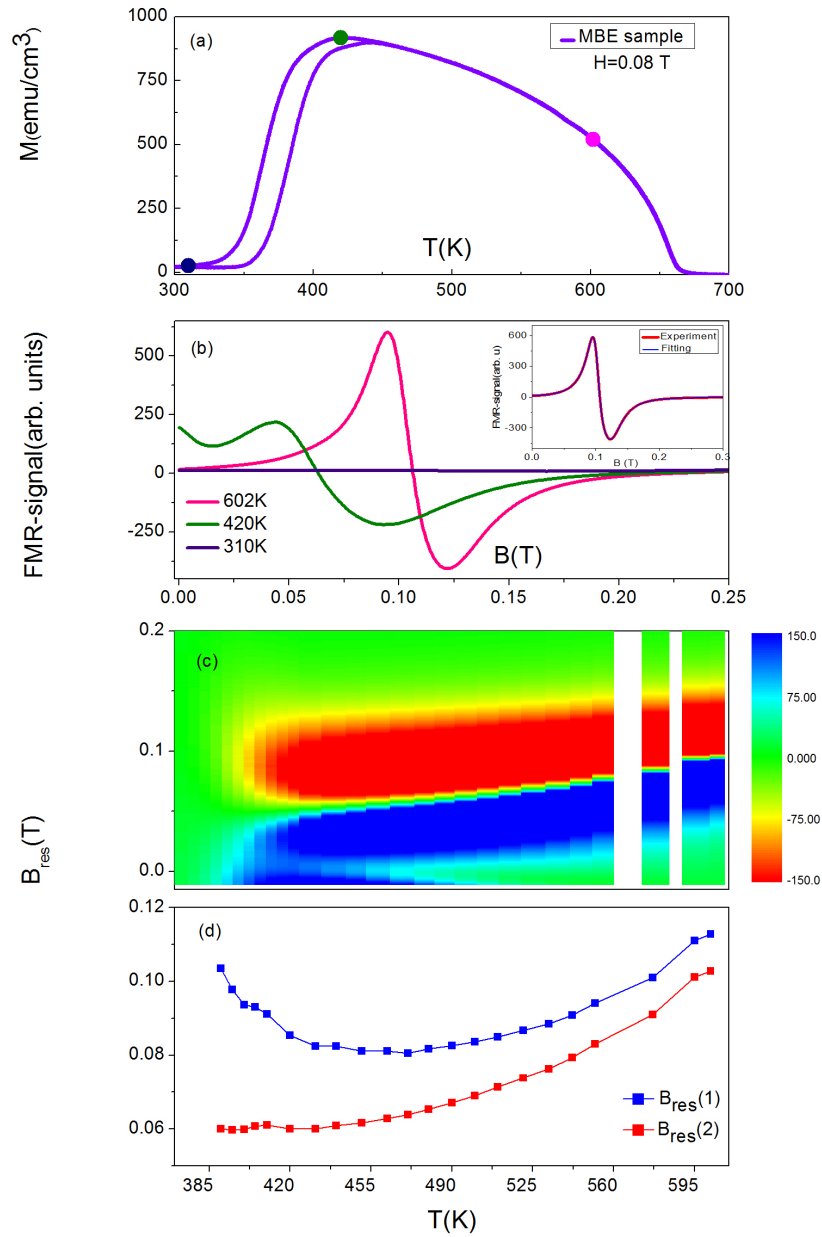


Figure 3.19: Static and dynamic magnetization measurement upon heating and cooling for $\text{Fe}_{50}\text{Rh}_{50}$ thin films with 33 nm thickness prepared by MBE. (a) SQUID measurement at 0.08T applied magnetic field in a temperature range from 300 to 700 K. (b) FMR spectrum as a function of temperature in AFM phase (violet) in phase transition region (green) and in FM phase (pink), inset: selected FMR spectra of the measurement (blue curve) and simulation (red curve) of the sample, (c) color-map for full phase diagram. (d) evolution of the position of the resonance line.

3-4 nm. As the magnetization in the FeRh system decreases by increasing Rh concentration [11], it can be identified the resonance at higher external fields to result from the interface mode. Assuming that the thickness of this Rh-enriched layer is the same for all samples, naturally explain the drastic change of the relative intensities of both signals as function of the film thickness (due to the smaller bulk contribution in the thinner films, the volume mode has more effect). The FMR measurements were continued by reducing the temperature stepwise to finally end up in the AFM phase as revealed from the magnetometry data. An overview is given by the color plot of Fig. 3.19 (c). Every vertical line in this figure corresponds to a FMR-spectrum measured at the respective temperature. The amplitude of the FMR-signal is displayed by the color code. A huge temperature (60 K) difference for the beginning of phase transition respect to the static measurement is clearly visible in this graph. It demonstrates that the dynamic properties probed by FMR react more sensitively to the presence of the AFM state by reducing temperature. The resonance fields which were determined by a fitting routine to the individual spectra at different temperatures are plotted in Fig. 3.19 (d).

For the 33 nm film at first it was focused on the mode that results from volume mode part and appears at lower external field values. It is obvious, that the resonance field shifts towards lower values by decreasing the temperature, until the amplitude of the signal vanishes completely around the phase transition region. By analyzing the temperature dependence with the help of the so-called Kittel-equation, for which in thin film geometry the resonance field only depends on the magnetization [9]

$$F = \frac{\omega}{2\pi} = \frac{\gamma}{2\pi} \sqrt{B(B + M_{eff})} \quad (3.1)$$

where F is frequency, B is applied external magnetic field, γ is gyromagnetic ratio and M_{eff} is effective magnetization. With ω being microwave frequency and the constant gamma (equation) the gyromagnetic ratio, obtain that for the 33 nm film the magnetization of the FM phase increases with decreasing temperature, as expected for an ordinary ferromagnet [12]. Even during the phase transition the value of the remaining magnetization probed by FMR is

not affected by the presence of the nucleating antiferromagnetic regions. The magnetization within the FM regions increases further for decreasing temperature which results in the continuous decrease in resonance field. This behavior is in good agreement with a model of the phase transition established in reference [7]. There, the phase transition is described as nucleation and growth of grains in a matrix. Corresponding to these experiment, i.e. decreasing the temperature from high towards lower values, growing AFM grains generated within a FM matrix. Assuming that the AFM regions cannot be excited at the microwave frequency and external field values available, the detectable FM volume shrinks drastically and as a consequence the FMR-signal amplitude decreases, until being below the detection limit of the setup.

In contrast, the mode having its origin at the interface region (and occurring at higher external field values) behaves in a different way. After reaching a minimum in resonance field the mode does not disappear, rather an increase in resonance field can be observed. As already discussed, the interface mode has its origin in the Rh-rich region, where an increased strain exists. This strain distorts the cubic B2 structure and influences the isotropic lattice expansion during phase transition. As shown already by magnetometry measurements a residual FM phase is left in the AFM regime. It has also been demonstrated in [13], where it was shown that the phase transition may completely suppressed in the region close to the substrate interface. Considering an ongoing phase transition (volume change) in the unstrained film areas, this will introduce additional strain to the FM part, which in turn influences its magnetization [14]. In continue a further indication of this scenario will provided. In case of the 8 nm film, even the volume mode shows a slight increase in the resonance field before disappearing. This is consistent with the results from magnetometry, which revealed an increased strain of the whole film showing up as residual magnetization. Due to this the volume mode does not behave like a genuine bulk mode anymore. The resonance field of the volume mode being a measure of the FM regions thus is not a good quantity to locate the phase transition.

By having a closer look to the color plot in Fig. 3.19 (c) an additional FMR-signal appears in a certain temperature range (390-490 K) at very small external fields. After appearing the amplitude of this signal increases, until both signals have a similar intensity (Fig. 3.19 (b) green line). The additional signal cab

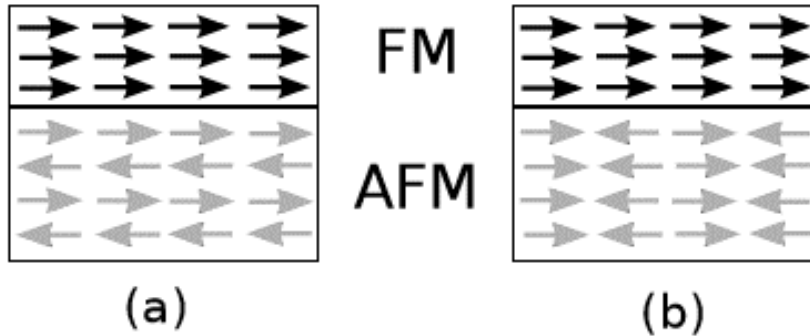


Figure 3.20: *The schematic diagram of AFM-FM interaction through the phase transition. (a) the interface coupling is FM (uncompensated interface) and (b) the interface coupling is AFM (compensated interface). Figure has been modified from reference [15].*

be ascribed to the result from an exchange bias effect, which arises after nucleation of AFM grains within the FM matrix [16]. As sketched in Fig. 3.20 there are two fundamentally different coupling configurations at the AFM-FM interface. In the case of compensated interfaces, there should be almost no effect on the resonance field position, because in sum no additional anisotropy is created (Fig. 3.20(b)). However, for uncompensated interfaces an unidirectional anisotropy is introduced to the system which changes the local field at the boundaries between FM and AFM regions (Fig. 3.20(a)).

The exchange bias phenomena can be discussed by intuitive model that is the most important model, relevant for the results of this study. In the FM phase above T_N all spins are completely aligned with the external magnetic field and the AFM is in a disordered state. Due to the no AFM effect on the FM, exchange bias is not observed in this state for hysteresis loop measurement. By reducing temperature below T_N in presence an external magnetic field, i.e. field cooling a ferromagnetic coupling generate at AFM-FM interface. The ferromagnetic coupling take place only in case of an uncompensated AFM-FM interface. When the external magnetic field is reversed, the FM spins reorient to trace the external magnetic field. Because of the strong AFM anisotropy, AFM spins will not rotate in the external magnetic field. However, the coupling at the interface creates a torque on the FM spins by the spins of AFM first monolayer. Due to the AFM torque on the FM spins, a higher applied external magnetic

field is needed to overcome the coupling between FM and AFM interface to saturate the FM spins in the opposite direction respect to the field cooling direction. It leads a shift of the hysteresis loop in the field axis towards negative fields. When the external magnetic fields reversed to the initial field cooling direction, the FM spins will rotate with the assistance of the extra field due to the FM-AFM internal field coupling. This internal field coupling leads the FM spins alignment with the external magnetic field at a smaller field. In turn adding this extra anisotropy field to the external field will shift the resonance position of the AFM-FM interface region towards lower field values. Therefore, the additional signal is a signature for the presence of the AFM phase. Compared to results from magnetometry the phase transition starts already at 490 K in FMR. This stems from the nucleation and grows of the AFM phase during cooling, letting the amount of uncompensated AFM-FM boundaries increase. Consequently, the signal intensity increases up to a certain point, where the fraction of the AFM phase becomes larger than the FM one. Beyond this point both signal intensities begin to decrease, before they disappear. Shortly after the appearance of the first AFM grains, they influence is also manifested by an increase of the resonance field of the interface mode. As discussed already some grains will nucleate near the interface layers and alter the strain. By further decreasing the temperature a larger area is affected by this additional strain, which results in a continuous change in resonance field.

The frequency dependence of the resonance field was used in order to investigate the magnetization behavior of the sample in the high temperature whereas system is completely in the FM phase. A broad band FMR set up was used to measure the resonance field in a frequency range from 7.8 up to 26.2 GHz. These frequency dependent measurements were performed at two fixed temperatures at $T=520$ K and $T=570$ K under UHV conditions and are shown in Fig. 3.21 and Fig. 3.22, respectively. The experiment results have been fitted with equation 3.1 to determine the g-factor. For the fitting, the magnetization was taken from SQUID measurement and therefore only g-factor was variable parameter. It was found that at 520 K g-factor is equal to 2.35 while at $T= 570$ K g-factor is equal to 2.37. The different value of g-factor at 520 and 570 K is because of the error during the measurements as well as the fitting process.

In Fig. 3.22 the fitting curve with $g=2.3$ has been compared with the fitting

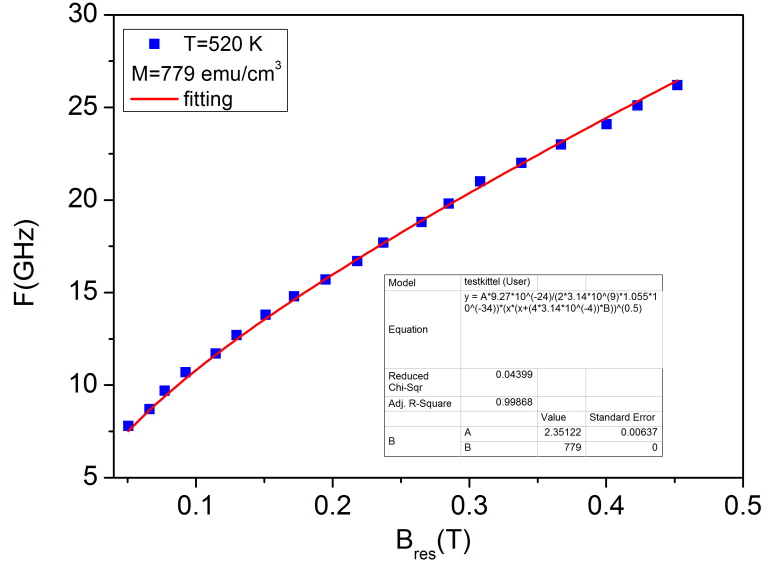


Figure 3.21: *In-plane resonance linewidth dependence of the frequency measured at 520 K, fitting curve show $g=2.35$.*

curve with $g=2.1$ which is for Fe atoms. Comparison of the curves reveals that g -factor for FeRh thin film at FM phase has higher value than Fe atoms. Since the frequency dependence of the resonance field has been measured in the FM phase, higher value of g -factor than Fe atoms reflects a strong orbital moment contribution μ_L/μ_S in the FeRh thin film which can be written as:

$$\frac{\mu_L}{\mu_S} = \frac{g - 2}{2} \quad (3.2)$$

Where μ_L and μ_S are orbital and spin magnetic moments, respectively [18].

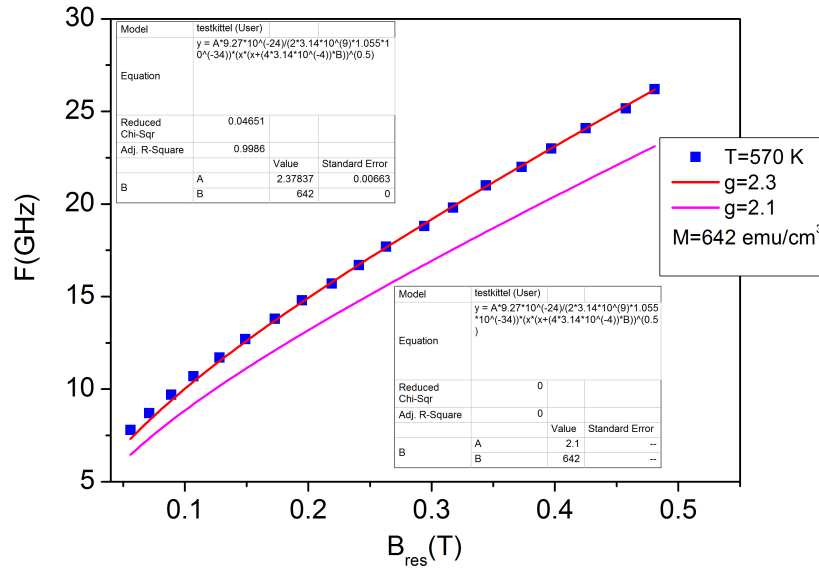


Figure 3.22: In-plane resonance linewidth dependence of the frequency measured at 570 K, fitting curve show $g=2.37$ and compared by $g=2.1$ curve.

3.2.2 Influence of thickness

For investigation of influence of thin film thickness on the static and dynamic response of FeRh system, 8 nm thick Fe₅₀Rh₅₀ thin film was grown on MgO single-crystal and capped by 5 nm Cr by means of MBE.

As same as thicker film the equivalent measurements on the 8 nm thin film were performed, shown in Fig. 3.23. The saturation magnetization M_s as function of T curve in a temperature interval of 160-700 K under an in plane oriented external magnetic field of 0.08 T is presented in Fig. 3.23(a). Note that different setups dedicated for temperatures either above or below ambient temperature were used. Qualitatively, both films, 33 nm thick and 8 nm thick exhibit a similar behavior. Similar to the thick film the thin film exhibits a hysteretic variation of M_s as function of temperature, indicating the existence of the first order phase transition.

Magnetization measurements were accomplished in a vibration sample magnetometer (VSM) under an applied external magnetic field up to 0.08T in a temperature range from 5 to 400 K and in a superconducting quantum inter-

ference device (SQUID) magnetometer under a same applied external magnetic field in a temperature range from 750 to 300 K. Since the direction of temperature sweep was not the same in the VSM and SQUID set ups, the magnetization curves do not overlap completely.

The most obvious difference between the thick and thin films is the temperature where the AFM-FM transition occurs is wider for the thin system. This effect has been already observed and explained in literature [3] as a not complete relaxation of the FeRh layer at the interface to the substrate. Another peculiarity of the 8 nm film as compared to the 33 nm one is the large residual magnetization ($M_s = 200$ kA/m) that remains at low temperatures after the phase transition. This observation provides an additional indication that the thin film differs from the expected behavior of the bulk phase diagram [3] for which in thermal equilibrium the whole system is expected to order antiferromagnetically for temperatures below the phase transition. The derivative of the absorption line in a temperature range from 177 up to 550 K measured, shown in Fig. 3.23(b) and indicated by the dots in Fig. 3.23(a). The interface model has more contribution because of the smaller bulk contribution of the 8 nm thin film. Fig. 3.23(c) shows the color-map of FMR spectrum for all temperature range measurement. Since the magnitude of the FM phase signals from the bulk contribution of the film and the interface mode are in the same order, both signals are clearly visible. On the other hand, volume mode is not visible because of the small saturation magnetization. The position of the resonance field as a function of temperature is displayed in Fig. 3.23(d). In agreement with the color-map plot, by increasing temperature where the FM phase nucleates, the resonance field decreases up to T_{tr} . In the magnetization saturation the resonance field has the lowest value. By further increasing temperature toward the second order phase transition leads to reduce the magnetization and consequently, resonance field increases (see equation 3.1) .

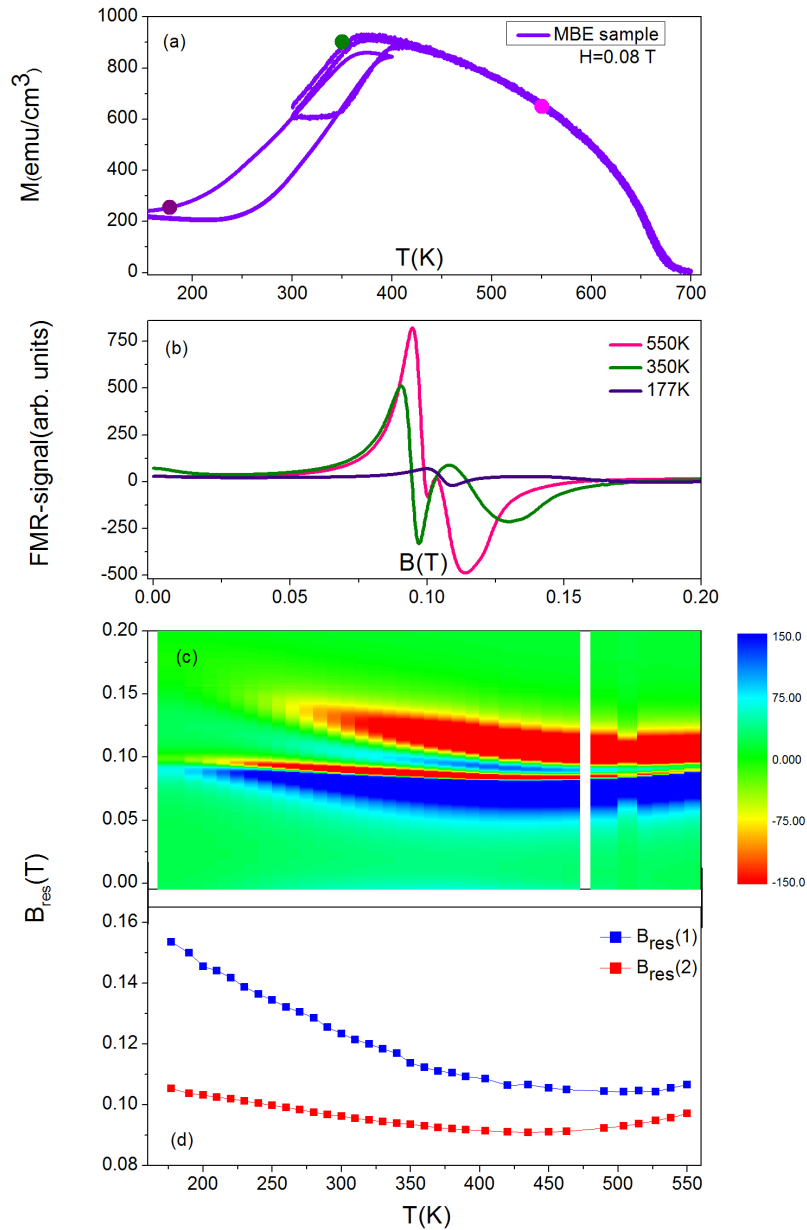


Figure 3.23: Static and dynamic magnetization measurements upon heating and cooling for $\text{Fe}_{50}\text{Rh}_{50}$ thin films with 8 nm thickness prepared by MBE. (a) SQUID measurement at 0.08 T applied magnetic field in a temperature range from 160 to 700 K . (b) FMR spectrum as a function of temperature in AFM phase (violet) in phase transition region (green) and in FM phase (pink). (c) color-map for full phase diagram. (d) evolution of the position of the resonance line.

3.2.3 Comparison of the growth techniques

To study the influence of growth condition on the static and dynamic response of FeRh system the equiatomic FeRh thin films with 33 and 8 nm thickness prepared by sputtering technique as well. Sputtered samples were capped by 2 nm Pd to avoid oxidation and are compared to MBE samples which have been discussed already, in magnetic point of view. MBE 33 nm and 8 nm thick samples capped by 4 nm Rh and 5 nm Cr layers respectively. The static magnetization of the samples was measured with a SQUID for an in-plane orientation of the magnetic field during heating and cooling. M-T curves for 33 nm equiatomic FeRh samples prepared by MBE and sputtered measured under an external magnetic field of 0.08 T are shown in Fig. 3.24. As is visible from Fig. 3.24 in the temperature range from 300 to 750 K both samples show a complete first order phase transition from AFM-FM at 382 K and 374 K and a second order phase transition from FM-PM at 670 K and 680 K for MBE and sputtered samples, respectively.

The sputtered samples show lower T_{tr} and higher T_c which can be ascribed to a slight deviation from the exact equiatomic stoichiometry lying within the error of RBS measurements. In Fig. 3.25 the typical FMR spectrum measured for the 33 nm thick is shown for MBE film and is compared to the spectra observed for the sputtered FeRh thin films. The spectrum is shown at $T=595$ K while the magnetic field H is oriented parallel to the film plane. Note that no variation of the resonance field for different in-plane orientations of the external dc-field H was observed. In Fig. 3.25 for all temperatures below T_c , the FMR spectrum is superposition of signals of typically 0.03 T peak-to-peak width. Since the extrinsic contribution of linewidth is associated with magnetic inhomogeneities within the sample and the anisotropy dispersion in the film, smaller linewidth for MBE sample shows higher magnetic ordering as well as the higher structural quality. Note that MgO substrate signals (signal from paramagnetic impurities) are visible at higher magnetic fields.

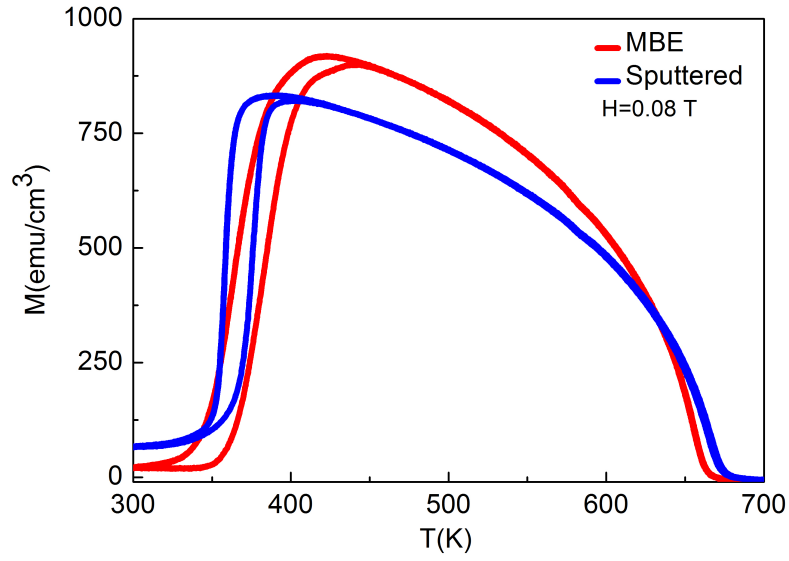


Figure 3.24: Comparison of the static magnetization curves at 0.08 T magnetic field for 33 nm thick MBE and sputtered $\text{Fe}_{50}\text{Rh}_{50}$ thin films.

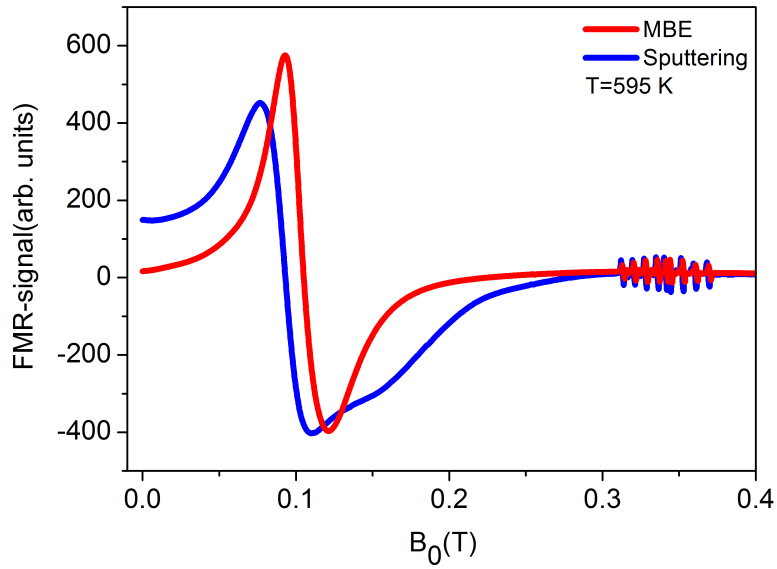


Figure 3.25: FMR spectra for 33 nm thick MBE and sputtered samples measured at 9.4 GHz and at 595 K which samples are in the FM phase.

The same approach has been pursued for the 8 nm thin films prepared by MBE and sputtering and are shown in Fig. 3.26. Both thin films clearly display the phase transition from AFM-FM phase. The phase transition for 8 nm thick sample has not been completed down to 300 K and show a minor thermal hysteresis loop (the complete range of magnetization properties was discussed in the previous section). In comparison with the 33 nm FeRh thin films (Fig. 3.24) a large thermal hysteresis loop is obvious. Fig. 3.27 shows FMR spectrum measured for Fe₅₀Rh₅₀ thin films with 8 nm thickness at 460 K where both samples are in FM phase. Two clear signals are detected for MBE sample while a different behavior is observed for sputtered sample. The different and almost flat signal indicate the structural defects, disorder and smaller grain size in the lattice of the sputtered thin film. In contrast, the MBE method by means of its lower growth rate and high purity leads to an increase of the magnetic homogeneity, structural quality and higher coverage rate of the substrate surface (coating). It has been known that FMR linewidth is very sensitive to the homogeneity of the anisotropy fields which is changed by crystal defects such as incomplete crystallization, twinning and stacking faults [19]. This can be explained by the surface/interface effect as the grain size decrease surface area increases.

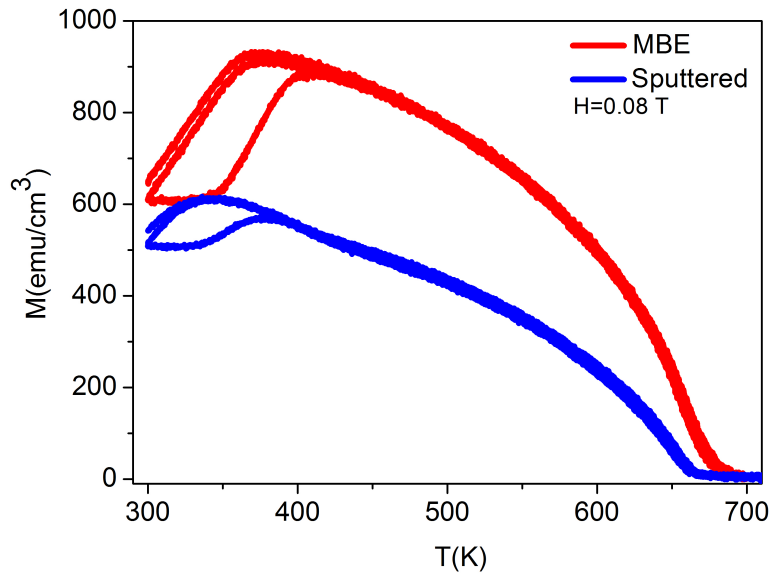


Figure 3.26: Comparison of the static magnetization curves at 0.08 T magnetic field for 8 nm thick MBE and sputtered $\text{Fe}_{50}\text{Rh}_{50}$ thin films.

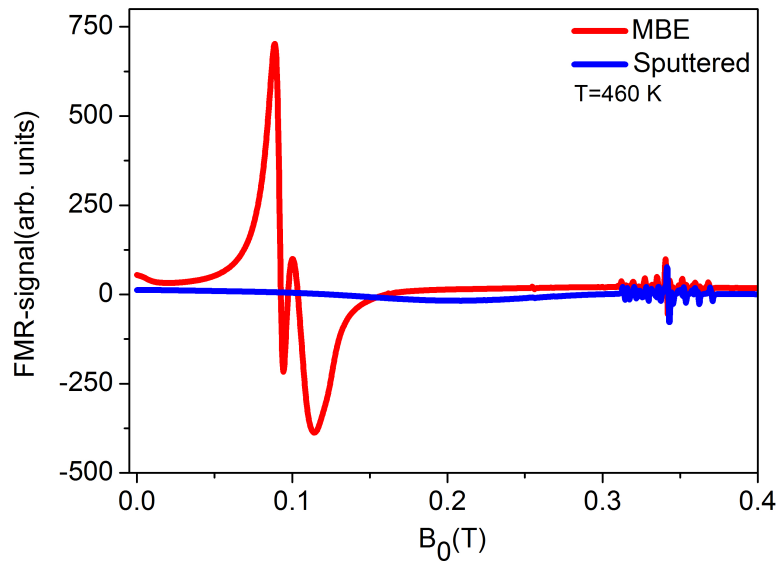


Figure 3.27: FMR spectra for 8 nm thick MBE and sputter samples measured at 9.4 GHz and at 460 K which samples are in the FM phase.

3.3 Ion irradiation

It has been known that magnetic properties of binary metallic alloy can depend sensitively on the arrangement of atoms in alloys, typically consisting of a 3d ferromagnetic metal with a non-magnetic metal [20]. Ion-beams are highly effective tools for randomizing the atomic arrangement in alloys, in a controllable way, and varying the nearest neighbour interactions between the magnetic atoms. Enormous changes in the saturation magnetization of certain alloys can be observed by varying the atomic arrangement. Recently, it has been reported that high-energy ion-beam irradiation induced a FM state in FeRh bulk sample (50 at.%) and in thin films at low temperatures at which the samples are normally AFM phase [21]. In order to investigate tuning the shape and transition temperature of the AF to FM phase transition in FeRh thin films by ion irradiation, equiatomic FeRh thin films were grown on MgO single crystal substrates and irradiated by low-energy/low fluence Ne^+ ion.

3.3.1 Sample preparation and characterization

In this section, the sample preparation method for growing FeRh thin films on MgO(100), characterization and stepwise implanted with Ne^+ at an energy of 20 keV are determined. Equiatomic FeRh thin films with a thickness of 35 nm have been deposited on MgO(001) single crystals from CRYSTEC/Berlin by means of MBE in UHV at a base pressure below 1×10^{-10} mbar.

The commercial MgO(100) substrates were prepared as same as discussed in the chapter 2. Aiming at polycrystalline films, deposition of FeRh was performed at room temperature followed by post annealing. Two separate sources were used to evaporate Fe and Rh and flux calibration has been applied using a quartz microbalance. Post annealing was performed up to 1123 K for 4h. The FeRh thin films composition was controlled by ex-situ RBS since composition has critical effect on the FeRh alloys magnetic response. Fig. 3.28 shows the RBS results obtained after annealing. The data is fit using a software (SIMNRA) for precise composition determination [22] and the it was found to be $\text{Fe}_{50}\text{Rh}_{50}$ with an uncertainty of around 1%.

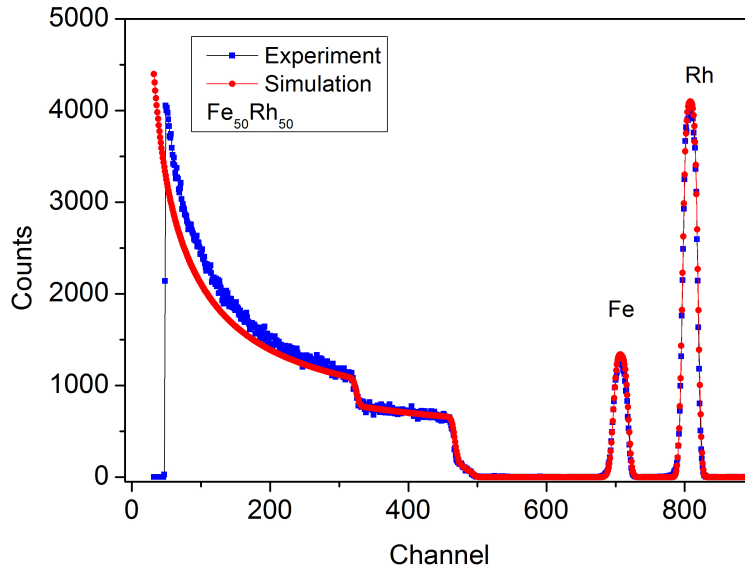


Figure 3.28: RBS of the as-prepared FeRh film. The composition was found to be $Fe_{50}Rh_{50}$ [23].

3.3.2 Tailoring the magnetism of FeRh thin films

In the first step a low-energy ion-beam irradiation process for the magnetic modification of FeRh thin film was investigated by using a focused ion beam system. The most convenient way to investigate the mass displacement after the collision cascade is to use computer simulation such as SRIM code. Prior to ion implantation, the Stopping and Range of Ions in Matter program (SRIM) was used to simulate the distribution of Ne ions inside the FeRh thin film lattice as well as overall damage created in terms of Iron, Rhodium and also vacancies. SRIM is a Monte-Carlo code that provides theoretical projections of the energies and depth profiles [22]. Implanted Ne profiles in FeRh sample for the incident energy of 20 keV are presented in Fig. 3.29 (a). The concentration profile inside the FeRh sample is shown to decrease gradually with thickness and to stop at a depth of ~ 400 Å. One quantitative parameter to characterize the amount of defect is the displacement per atom (dpa). The definition of dpa is the number of times that an atom in the target is displaced at a constant fluence. After magnetic and structural characterization, irradiation with 20 keV Ne^+ ions was

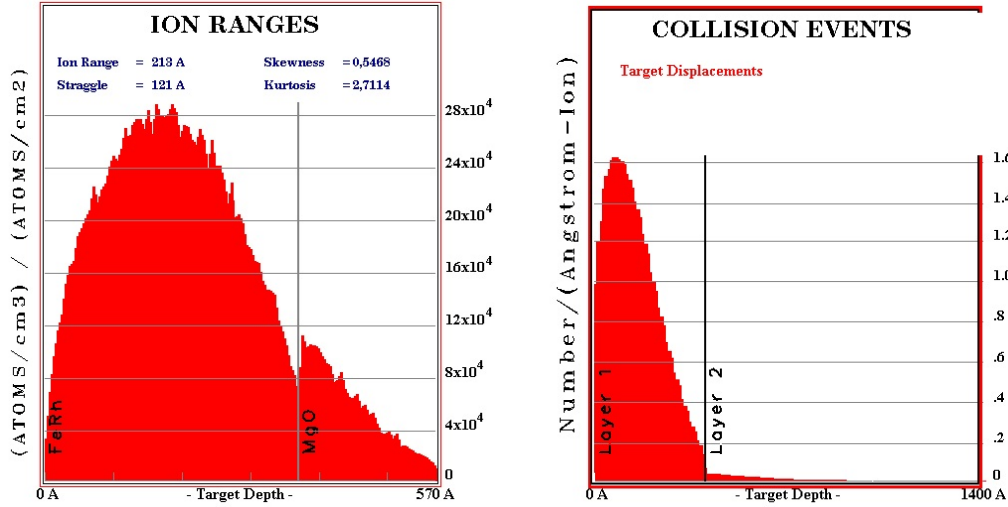


Figure 3.29: SRIM predictions [22] on the ion penetration and collision events with the present experimental conditions: Ne^+ at 20 keV on FeRh/MgO (35 nm) with an incidence angle of 0° . Left: distribution of the ion penetration. Right: distribution of atom displacement in the sample. As is visible, only a very small fraction of ions is deposited in the MgO substrate.

performed at room temperature with different total ion fluencies of 5×10^{12} , 7.5×10^{12} , 1×10^{13} , 2.5×10^{13} , 7.5×10^{13} ions/cm². Aiming to eliminate the AFM to FM phase transition, a control sample (with same thickness and composition) was irradiated with 3×10^{14} ions/cm². Using the SRIM calculation, 20 keV Ne^+ ion applied to locate the projected range of the implanted ions as well as the maximum dpa at 20 nm below the surface of the sample.

The magnetic properties of the samples were measured using a SQUID magnetometer for the as-grown sample as well as after each implantation step. For magnetization measurement sample was cooled down to 5 K at zero magnetic field. The magnetization-temperature loops were measured during heating from 5 K to 400 K under the applied magnetic fields of 150 Oe and cool down again under the same condition. Because of the thermomagnetic irreversibility made by deblocking of ferromagnetic domains or superparamagnetic clusters, curve split. The AFM to FM phase transition for as-grown film is located at about 375 K (Fig. 3.30). It is higher than 350 K the phase transition for equi-atomic FeRh thin film likely due to the deviation from the exact equi-atomic stoichiometry lying within the error of RBS measurements. Since the maximum accessible

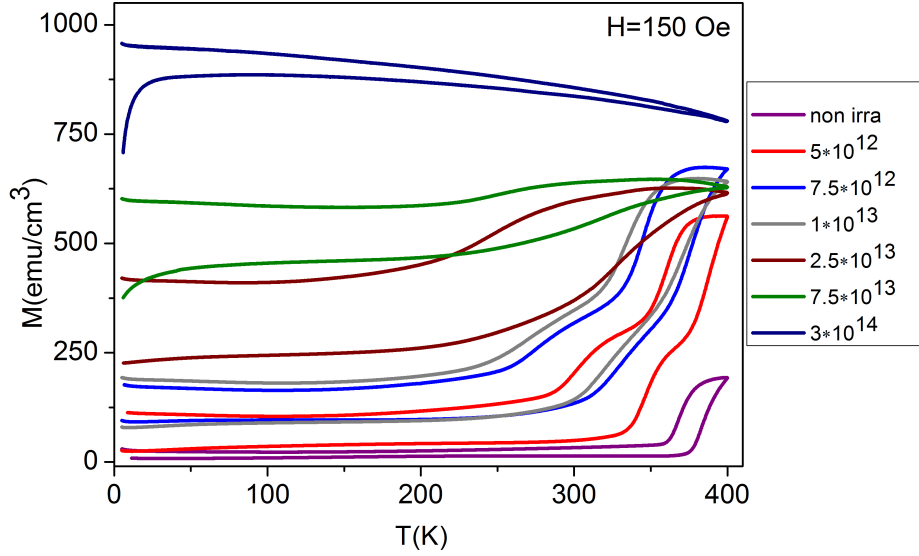


Figure 3.30: ZFC/FC thermomagnetic measurements recorded at a field of 150 Oe. The Ne^+ ion fluence applied at an ion energy of 20 keV is indicated in ions/cm² [23].

temperature in the SQUID setup was 400 K, minor thermal loops were measured. The temperature dependence of the magnetization of each sample is shown in Fig. 3.30. It is obvious that Ne^+ irradiation by fluence of 5×10^{12} ions/cm² leads to shift about 45 K in T_{tr} toward the lower temperature. Decreasing temperature again, however, leads to strong overlap of the phase transition loops. On the other hand, the splitting between the ZFC and FC curves in the low-temperature regime becomes more and more pronounced indicating an increasing ferromagnetic background induced by the ongoing chemical disordering, which is in agreement with other works [25, 21]. As Fig. 3.30 depicts by irradiation FeRh thin film the AFM-FM phase transition shifts toward lower temperature and completely eliminated at a fluence of 3×10^{14} ions/cm². In this case the FeRh thin film becomes ferromagnetic in the entire measured temperature range. Fig. 3.31(a) depicts that the transition temperature decreases almost linearly by increasing ion irradiation fluence while Fig. 3.31(b) shows the ion fluence dependence of the saturation magnetization. A striking effect is the fact that only a relatively low ion fluence of 3×10^{14} ions/cm² is necessary

in order to fully change the low-temperature magnetic properties from AFM to FM phase. It means that irradiation by 3×10^{14} ions/cm² fluence all sample atoms at least one time experience a displacement. In Fig. 3.32 the saturation magnetization as a function of dpa is shown. The SRIM calculation suggests that the elastic collision play the dominant role in determining the magnetic properties of the samples. It means that the irradiation-induced disorder of the atomic arrangement or irradiation-induced lattice defect [30].

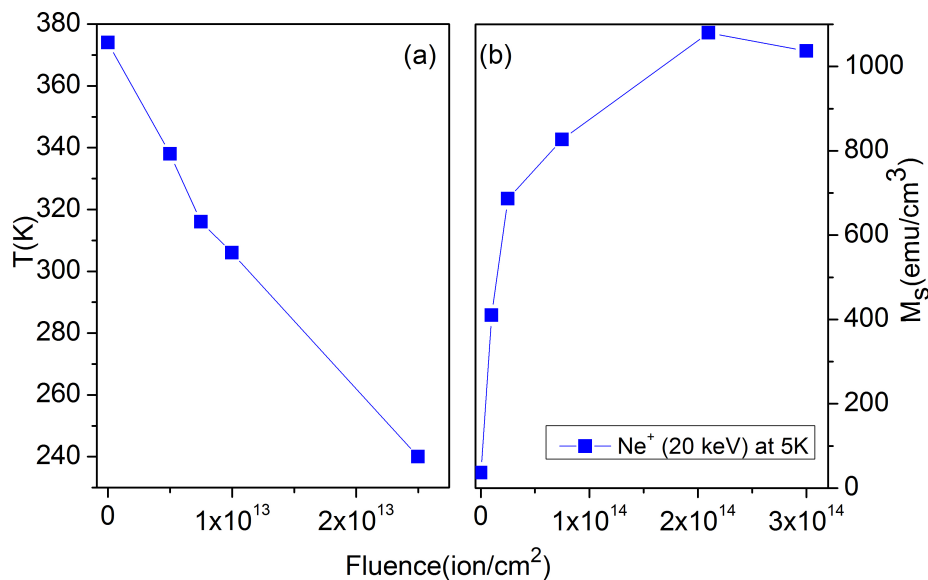


Figure 3.31: (a) The phase transition temperature as a function of fluence and (b) the fluence-dependent saturation magnetization measured at 5 K [23].

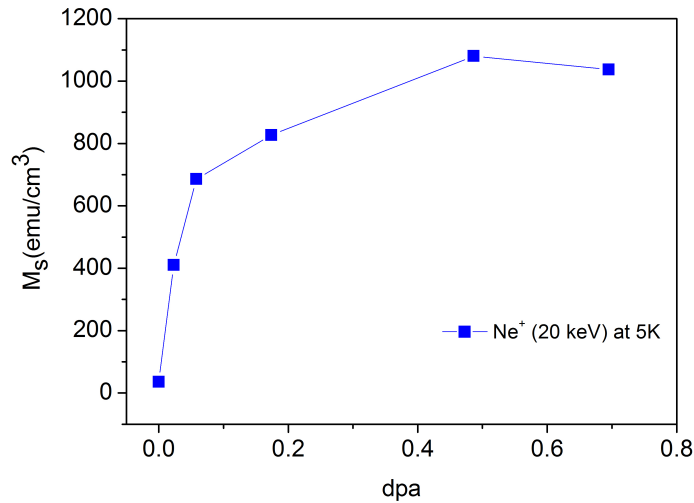


Figure 3.32: Evolution of the saturation magnetization with increasing dpa [23].

For our thin films, the increasing of the ferromagnetic signal by Ne^+ ion irradiation at 5 K is displayed in Fig. 3.33. As was expected by increasing ion irradiation fluence ferromagnetic back ground increases. In order to investigate the effect of irradiation on the film structure, the control sample was analyzed by XRD before and after implantation. Therefore, by employing $\text{Cu}_{K\alpha}$ radiation surce a θ - 2θ diffractometer, XRD pattern were measured in glancing angle geometry.

The incidence angle was kept above the critical angle ($\alpha_c = 0.42^\circ$) at 1 degree. Fig. 3.34 shows the XRD scans of both as-grown and irradiated samples (with 3×10^{14} ions/cm² fluences). Because of the relative amount of the lattice defects introduced in the B2 type phase by ion implantation the intensity of peaks decreased. The lattice defects introduced by ion irradiation can stabilize the ferromagnetic state in the B2 type FeRh compounds. It can be explained by either the increase of the lattice parameter due to the disordering or the change of the number of magnetic Fe atoms within their nearest neighborhood [26]. It is noticeable that the crystallite size (~ 20 nm) of thin film and the lattice constant (2.985 \AA) value were not changed by the implantation. Changing in the lattice parameter due to irradiation at higher fluencies ($> 1 \times 10^{15} \text{ cm}^{-2}$) and/or using other ions should be consider [27]. The intensity of the (001) B2

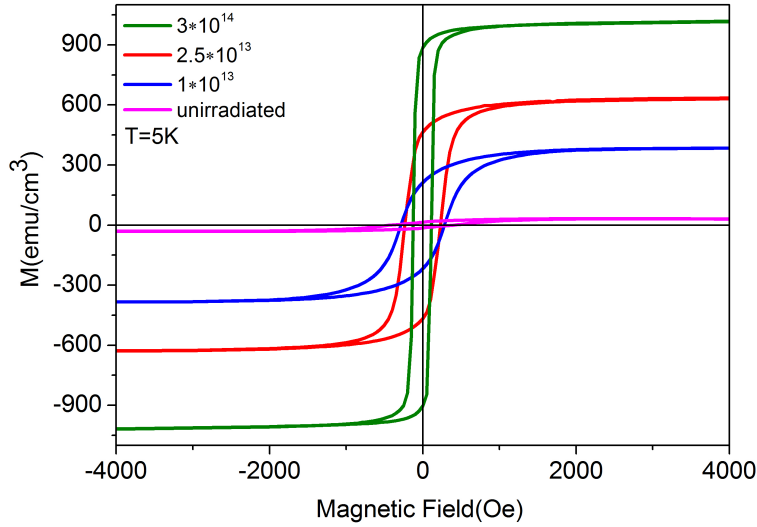


Figure 3.33: M - H curves at 5 K for the unirradiated sample and samples irradiated with a 20 keV Ne^+ ion-beam.

superstructure peak is stronger influenced than the peaks that are not sensitive to the chemical order. The order parameter can be qualitatively calculated by comparing the integrated intensity of the superstructured (100) peaks with that of the fundamental (200) peaks of the B2-type structure. This is normally defined as the long-range order parameter S [28, 29]. The S parameter decreases by more than 50%. The order parameter S reduced from about 90% to less than 50% by an error of about 10%. Since the implantation influenced the other diffraction peaks, a static Debye-Waller factor (defines the disorder introduced by the implantation in the complete unit cell) assess to about 0.2 \AA .

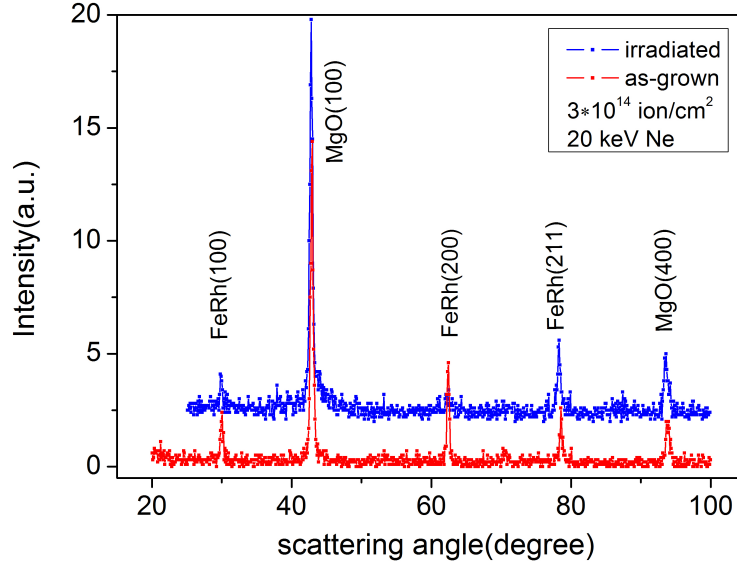


Figure 3.34: XRD diffraction pattern measured at an incidence angle of 1 degree of the control sample in the non-irradiated state (red), after Ne^+ irradiation at a fluence of 3×10^{14} ions/cm² (blue). The discrepancy at the (200) peak, as grown sample, is probably due to an influence of the substrate MgO (220) reflection. Figure reproduced from reference [23].

3.3.3 Effect of post irradiation annealing

Furthermore, the magnetic modification of the Ne^+ irradiated FeRh sample by thermal annealing is also examined. Equiatomic FeRh thin film of about 37 nm thickness was deposited on MgO substrate as same as explained before. For as grown thin film the $\text{Fe}_{50}\text{Rh}_{50}$ composition was confirmed by RBS measurement and analyzing SIMNRA program simulation. To calculate the favorable ion fluence first the atomic density of FeRh thin film was calculated by:

$$\rho_{(\text{FeRh})} = \frac{\rho\left(\frac{\text{g}}{\text{cm}^3}\right) N_A\left(\frac{1}{\text{mol}}\right)}{(\text{Fe}_{\text{weight}} + \text{Rh}_{\text{weight}})\frac{\text{g}}{\text{mol}}} \quad (3.3)$$

$$\rho_{(\text{FeRh})} = 3.4 \times 10^{22} \frac{\text{number atoms}}{\text{cm}^3} \quad (3.4)$$

here the mass density for FeRh thin films is $\rho = 9.1\left(\frac{\text{g}}{\text{cm}^3}\right)$ and $\text{Fe}_{\text{weight}} = 55.84\left(\frac{\text{g}}{\text{mol}}\right)$

$$Rh_{weight} = 102.9\left(\frac{g}{mol}\right)$$

By using Equation 2.4 for 20 keV Ne⁺ ion irradiation while dpa is equal to 1 the fluence can be calculated as:

$$\Phi = \frac{\rho(FeRh)}{tota\ disp} = \frac{3.4 \times 10^{22} \left(\frac{number\ atoms}{10^8\ A^\circ\ cm^2}\right)}{1.6 \left(\frac{number\ atoms}{A^\circ\ ion}\right)} \quad (3.5)$$

$$\Phi = 2.1 \times 10^{14} \left(\frac{ion}{cm^2}\right) \quad (3.6)$$

In this equation the total displacement per atom is SRIM simulation output. The dpa equal to 1 guarantees at least one collision and subsequently a movement for all atoms in the sample. After annealing, ion irradiation was performed to produce defects at room temperature. The magnetic properties were measured by VSM set up for the as prepared, irradiated sample and after each annealing step. Fig. 3.35 shows the displacement profile for 35 nm thick sample while Fig. 3.36 illustrates ZFC/FC curves. The figure indicates that for unirradiated film T_{tr} is 375 K. While the AFM to FM phase transition is almost removed at fluence 2.1×10^{14} ion/cm², i.e. the film becomes ferromagnetic in the complete temperature range. According to other studies, lattice defects in B2-type FeRh introduced by the ion beam irradiation cause the change in the magnetic state [29]. On the other hand, phase transition from AFM to FM appears after annealing as a result of erasing defects. During the thermal annealing, the irradiation-induced disorder B2 structure is thermally relaxed to ordered B2 structure, causing the change in magnetic state from FM to AFM state. It indicates that the number of lattice defects introduced by the excess irradiation decreases owing to the annealing. Therefore, the irradiation-induced magnetization can disappear through the annealing process. Further annealing thin film leads to shift of the phase transition to lower temperature by ~ 70 K. Since the lattice defects introduced by the ion beam irradiation were gradually removed by annealing, the magnetization was also significantly modified, which resulted in the shift of phase transition. To summarize, the present result shows that the combination of energetic ion irradiation and subsequent thermal annealing can be used as a useful tool to systematically control the magnetic state of FeRh films.

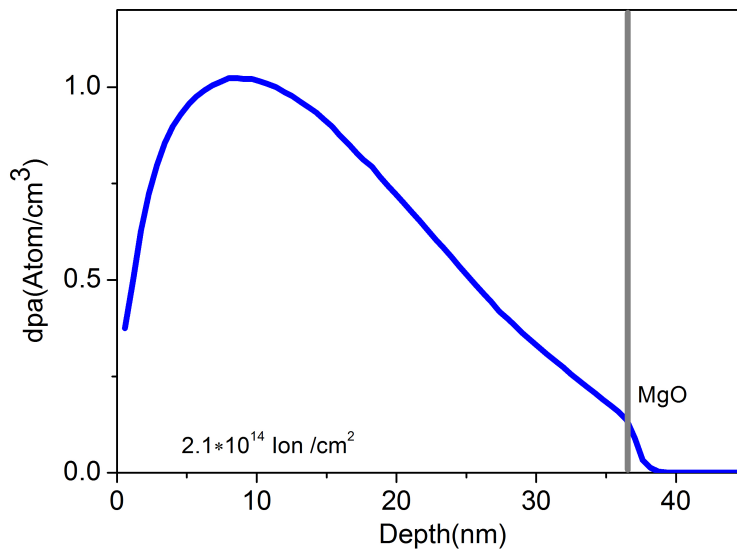


Figure 3.35: The dpa would be equal to 1 if sample irradiated by 20 keV Ne^+ ion irradiation with 2.1×10^{14} ion/cm² fluence.

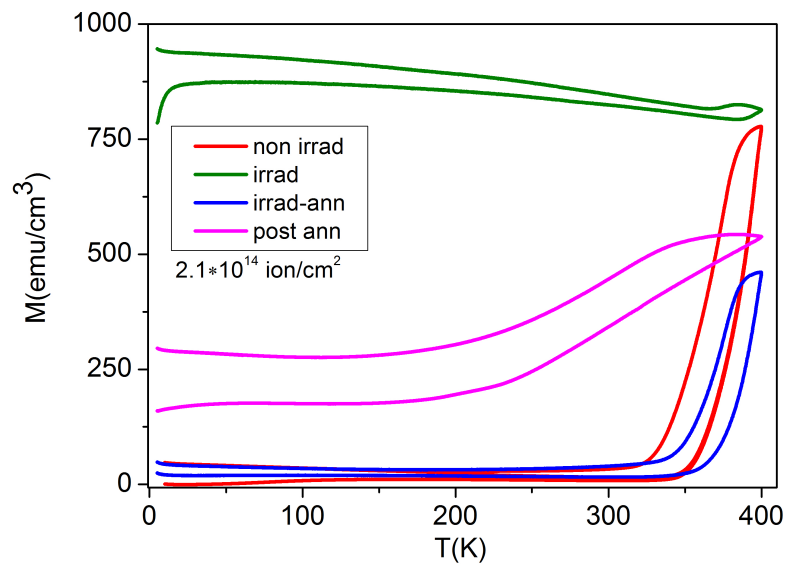


Figure 3.36: ZFC/FC thermomagnetic measurements for sample with 35 nm thickness recorded at a field of 150 Oe.

Bibliography

- [1] J. M. Lommel and J. S. Kouvel, “Effect of mechanical and thermal treatment on the structure and magnetic transition in FeRh“ J. Appl. Phys. **38**, *1263 (1967)*.
- [2] R. Fan, C. J. Kinane, T. R. Charlton, R. Dorner, M. Ali, M. A. de Vries, R. M. D. Brydson, C. H. Marrows, B. J. Hickey, D. A. Arena, B. K. Tanner, G. Nisbet, and S. Langridge, “Ferromagnetism at the interfaces of antiferromagnetic FeRh epilayers“, Phys. Rev. B **82**, *184418 (2010)*.
- [3] G. C. Han and J. J. Qiu, “Magnetic stability of ultrathin FeRh films“, J. Appl. Phys, **113**, *17C107 (2013)*.
- [4] I. Suzuki et al. “Stability of ferromagnetic state of epitaxially grown ordered FeRh thin films“, J. Appl. Phys, **105**, *07E501 (2009)*.
- [5] Y. Kaneta, S. Ishino, Y. Chen, S. Iwata, and Akihiro Iwase, “Theoretical Calculations for Magnetic Property of FeRh Inter-Metallic Compound with Site-Exchange Defects“, Jpn. J. Appl. Phys., Part 1 **50**, *105803 (2011)*.
- [6] S. Inoue, H. Ko, and T. Suzuki, “Magnetic Properties of Single-Crystalline FeRh Alloy Thin Films“, IEEE **44**, *468-8511 (2008)*.
- [7] E. Mancini, F. Pressacco, M. Haertinger, E. Fullerton, T. Suzuki, G. Woltersdorf, and C. H. Back, “Magnetic phase transition in iron-rhodium thin films probed by ferromagnetic resonance“, J. Appl. Phys, **46**, *245302 (2013)*.
- [8] V. L. Moruzzi, and P. M. Marcus, “Structural effects on the magnetic properties of FePd and FeRh“, Phys. Rev. B **48**, *16106 (1993)*.

- [9] C. Kittel, “ Ferromagnetic resonance“ , Le J. de Physique et le radium tome, **12**, 291 (1951).
- [10] Z. Frait and D. Fraitova, “Frontiers in Magnetism of Reduced Dimension Systems“ ed. by P. Wigen, V. Baryachtar and N. Lesnik , NATO ASI Series 3, Kluver Acad. Publ. **49**, 1998, 121-152 (1998).
- [11] P. E. M. Hofer and P. E. Cucka. “Magnetic Properties of Rh-rich FeRh alloy“, Journal of Physics and Chemistry, **27**, 1552-1555, (1966).
- [12] G. T. Rado and H. Suhi. eds. “Magnetism“, **2A**, Academic Press, (1965).
- [13] R. Fan, C. J. Kinane, T. R. Charlton, R. Dorner, M. Ali, M. A. deVries, R. M. D. Brydson, C. H. Marrows, B. J. Hickey, D. A. Arena, B. K. Tanner, G. Nisbet and S. Langridge, “Ferromagnetism at the interfaces of antiferromagnetic FeRh epilayers“, Physical Review B, **82**, 184418, (2010).
- [14] M. J. McLaren, M. A. de Vries, R. M. D. Brydson and C. Marrows, “Characterisation of Magnetic FeRh Epilayers“, Journal of Physics: Conference Series, **371**, 012031, (2012).
- [15] J. Nogues, I. K. Schuller, “Exchange bias“, J. Magn. Magn. Mater. **192**, (1999).
- [16] J. Barker, and R. W. Chantrell, “Higher order exchange interactions leading to metamagnetism in FeRh“ , Phys. Rev. B, **92**, 094402, (2014).
- [17] J. Nogues and I. K. Schuller, “Exchange bias“, J. Magn. Magn. Mater, **192**, 203-232, (1999).
- [18] Y. B. Band and Y. Avishai, “Quantum Mechanics with Applications to Nanotechnology“, first edition, Netherlands (2013).
- [19] L. Wei, P. Huang, Z. Chen H. Chenchong ,W. Yuxin, and Y. Biao, “Magnetization studies of first-order magnetostructural phase transition in polycrystalline FeRh thin films“, J. Appl. Phys, **45**, 435001 (2012).
- [20] E. Menendez, M. O. Liedke; J. Fassbender, T. Gemming, A. Weber, L .J. Heyderman, K. V. Rao, S. C. Deevi, S. Surinach, M. D. Baro, J. Sort, and J.

- Nogues, “Creation of sub-100 nm ferromagnetic dots by selective irradiation of a paramagnetic intermetallic alloy“, *SMALL* **5**, 229-234 (2009).
- [21] K. Aikoh, S. Kosugi, T. Matsui, and A. Iwase, “Quantitative control of magnetic ordering in FeRh thin films using 30 keV Ga ion irradiation from a focused ion beam system“, *J. Appl. Phys.* **109**, 07E311 (2011).
- [22] M. Mayer, SIMNRA User’s Guide, Report IPP 9/113, Max-Planck-Institut für Plasmaphysik, Garching, Germany, (1997).
- [23] A. Heidarian, R. Bali, J. Grenzer, R. A. Wilhelm, R. Heller, O. Yildirim, J. Lindner, K. Potzger, “Tuning the antiferromagnetic to ferromagnetic phase transition in FeRh thin films by means of low-energy/low fluence ion irradiation“, *Nucl. Instr. Meth. Phys. Res. B*, **358**, 251-254 (2015).
- [24] B. Schmidt and K. Wetzig, “ Ion Beams in Materials Processing and Analysis“, New York Dordrecht London, (2013).
- [25] N. Fujita, S. Kosugi, Y. Sa Saitoh, Y. Kaneta, K. Kume, T. Batchuluun, N. Ishikawa, T. Matsui, and A. Iwase, “Magnetic states controlled by energetic ion irradiation in FeRh thin films“, *J. Appl. Phys.* **107**, 09E302 (2010).
- [26] J. Nogues, E. Apinaniz, J. Sort, M. Amboage, M. d’Astuto, O. Mathon, R. Puzniak, I. Fita, J. S. Garitaonandia, S. Surinach, J. S. Munoz, M. D. Baro, F. Plazaola, and F. Baudelet, “Volume expansion contribution to the magnetism of atomically disordered intermetallic alloys“, *Phys. Rev. B* **74**, 024407 (2006).
- [27] O. D. Roshchupkina, T. Strache, J. McCord, A. Muecklich, C. Baetz, and J. Grenzer, “Structural modifications of thin magnetic Permalloy films induced by ion implantation and thermal annealing“, *Acta Mater.* , 278-284 (2014).
- [28] B. E. Warren, “ X-Ray Diffraction“, Dover Publ. Inc., New York, (1990).
- [29] V. Cantelli, J. von Borany, A. Muecklich, Z. Shengqiang, and J. Grenzer, “Influence of energetic ions and neutral atoms on the L10 ordering of FePt films“, *Nucl. Instrum. Meth. B* **257**, 406-410 (2007).

- [30] N. Fujita, S. Kosugi, Y. Saitoh, and et al, “Quantitative control of magnetic ordering in FeRh thin films using 30 keV Ga ion irradiation from a focused ion beam system“, *J. Appl. Phys*, **107**, *09E302 (2010)*.
- [31] X. Ou, A. Keller, M. Helm, J. Fassbender, and S. Facsco, “Reverse Epitaxy of Ge: Ordered and Faceted Surface Patterns“, *J. Phy. Rev. Lett.* **111**, *016101 (2013)*.

Chapter 4

Summary and outlook

The main objectives of this thesis are to understand and control the magnetic and structural response of the FeRh system as a function of extrinsic and intrinsic parameter variation. From the perspective of applied science, it is interesting to investigate correlations between the magnetic behavior and functional effects observed in the FeRh system. To determine the influence of parameters modification on the magnetic response of FeRh thin films different pathways were explored to tune the magnetic and structure response of FeRh alloy which are summarized below:

1. The correlation between annealing temperature and T_{tr} of FeRh thin films was studied by measuring M-T curve. The results of the magnetization measurements show that the annealing temperature has a significant influence on:
 - T_{tr} increases with increasing annealing temperature, while the thermal hysteresis width decreases.
 - High-temperature annealing process reduces the compositional fluctuation in the thin films.
2. Effect of thickness on the magnetic behavior was studied by growing equiatomic FeRh thin films with different thickness. The results show that by decreasing film thickness the first order phase transition temperature reduces and also the transition becomes much broader for the FeRh thinner films. The AFM-FM phase transition was observed for samples with thickness below 10 nm.

3. Effect of chemical composition on the magnetic response of $\text{Fe}_x\text{Rh}_{100-x}$ thin films over the $44 \leq x \leq 52$ composition range was investigated. M-T curve measurements show that for the Fe-rich samples, the effect of α' -phase impurities could dominate such that it cause T_{tr} to decrease significantly. The magnetization measurements provide additional information such as: The FeRh thin films show the first-order phase transition only at $44 \leq x \leq 50$ composition interval.

To enhance the understanding of the dynamic and static of the first order phase transformation in FeRh thin films, 33 nm and 8 nm thick equiatomic FeRh thin films by means of MBE and sputtering techniques were prepared. Our results show that the phase transition can be monitored through the FMR measurements also AFM and FM contribution can be separated by it. The comparison of magnetic moment, and the position of the resonance, allowed us to describe qualitatively the nucleation and the growth of the magnetic domains during the first-order phase transition. Results obtained by FMR measurements demonstrate that AFM-FM phase interaction produces a signal even in high temperature and, consequently, the AFM phase exists after phase transition which cannot be detected by the static measurements. The FMR measurements reveal that the two phases are formed in FeRh thin films, Rh-rich on the substrate interface and $\text{Fe}_{50}\text{Rh}_{50}$ phases. The effect of two phases, which have different composition, is more visible for thinner sample due to the less bulk contribution. Both phases in the sample generate FM signals in high temperature and due to superposition of two closely positioned modes the FMR spectrum is asymmetric. In the next step the static and dynamic response of 33 and 8 nm thick samples which prepared by MBE and sputtering were compared. For thick samples, FMR spectrum shows that by using MBE can grow well ordered FeRh thin films with small FMR linewidth. While for thinner samples, no signal was detected for sputtered sample likely because of different interface properties and high magnetic inhomogeneity which increase the linewidth. Finally, the frequency dependence of the resonance position was measured for 33 nm thick MBE sample. This measurement confirms the strong orbital moment contribution for FeRh system.

It is well-known that the energetic ions can be used as a new tool for the quanti-

tative control of the magnetic state of FeRh alloy. For the final part of this work, tuning the shape and transition temperature of the AFM to FM phase transition in FeRh thin films were investigated by means of low-energy/low fluence Ne⁺ ion irradiation. The application of 20 keV Ne⁺ ions at different fluencies leads to broadening of the AFM to FM phase transition as well as a shift in the T_{tr} towards the lower temperatures with increasing ion fluence. Moreover, the FM background at low temperatures generated by the ion irradiation leads to pronounced saturation magnetization at 5 K. Complete erasure of the transition, i.e. FM ordering through the whole temperature regime, was achieved at a Ne⁺ fluence of 3×10¹⁴ ions/cm². It does not coincide with the complete randomization of the chemical ordering of the lattice.

From the application point of view, equiatomic FeRh thin film can be used for fabrication of nanostructural magnetic objects which is of essential importance for the functioning of devices such as patterned data storage media and magnetoresistive random access memories. It could be studied by the patterning of nanostructural magnetic structures by using of the large increase in the saturation magnetization of Fe₅₀Rh₅₀ thin films caused by precise atomic displacements. Patterning of magnetic areas could be performed by using e-beam lithography in the form of stripes which can be separated by some nanometer wide spacers. In this state the magnet/non-magnet/magnet structure displays a reprogrammable AFM and FM states configurations in zero field.

Publications

Articles

- "Tuning the antiferromagnetic to ferromagnetic phase transition in FeRh thin films by means of low-energy/low fluence ion irradiation" , A. Heidarian, R. Bali, J. Grenzer, R. A. Wilhelm, R. Heller, O. Yildirim, J. Lindner, K. Potzger, Nucl. Instr. Meth. **358**, 251-254 (2015).
- "Static and dynamic magnetization across the first order phase transition in FeRh thin film", S. Stienen, A. Heidarian, S. Salamon, T. Thomson, K. Potzger, J. Lindner, Phys. Rev. B, in submission, (2015).
- "Ferromagnetic insulating and reentrant spin glass behavior in Mg doped $\text{La}_{0.75}\text{Sr}_{0.25}\text{MnO}_3$ Manganites", P. Kameli, H. Salamati, A. Heidarian, J. Non-Crystalline Solids. **355**, 917 (2009).
- "Structural, Magnetic and Electrical Properties Of Mg Doped $\text{La}_{0.75}\text{Sr}_{0.25}\text{MnO}_3$ Manganite", P. Kameli, H. Salamati, A. Heidarian, International Conference on Magnetic Materials, (ICMM), AIP Conference Proceeding **163**, (2008).

Talks and posters

- "Static and dynamic magnetization across the first order phase transition in FeRh thin films", Spring Meeting of the German Physical Society (DPG), Berlin, Germany (2015).
- "Ferromagnetic resonance across the phase transition in FeRh thin films" , IEEE International Magnetics Conference (INTERMAG), Dresden, Germany (2014).

- "Ferromagnetic resonance in FeRh thin films through the magnetic phase transition", Spring Meeting of the German Physical Society (DPG), Dresden, Germany (2014).
- "Magnetic and Structural Properties of Equiatomic FeRh thin films", Joint European Magnetic Symposia (JEMS), Rhodes, Greece (2013).
- "Investigation of the magnetic properties of equiatomic FeRh thin films", IEEE Summer School on Magnetism, Assisi, Italy (2013).
- "Simple lattice model for complex systems" , Institute of Physical Chemistry, Polish Academy of Science, Warsaw, Poland (2011).
- "The effect of Mg Doping on the Structural and Magnetic properties of $\text{La}_{0.75}\text{Sr}_{0.25}\text{MnO}_3$ Manganite", Annual Iranian Conference of Physics, Yasoj University, Yasoj, Iran (2010).

In case of talks and posters only self-presented contributions are listed.

Acknowledgments

I would never be able to finish this thesis without invaluable support of several persons. In particular I want to thank:

- Prof. Dr. Jürgen Faßbender for giving me the chance to follow my research at the HZDR and the support
- Prof. Dr. Thomas Thomson for the excellent collaboration as well as for refereeing my dissertation
- Dr. Kay Potzger for the great support and professional supervision. He was always very much concerned about the progress of the project and provided a very pleasant working atmosphere.
- Dr. Jürgen Lindner for lots of interesting discussions and support during the FMR part of my research
- Dr. Rantej Bali and Dr. Sven Stienen for fruitful discussions and lots of support in writing process
- Dr. Ciaran Fowley and Dr. Anna Semisalova for critically reading and correct the draft version of my thesis manuscript
- Andreas Henschke for the excellent and quick technical support in every situation
- Dr. Rene Hübner for the TEM investigations
- Andrea Scholz for the XRD measurements
- Dr. Richard Arthur Wilhelm for graciously instructing me in the use of the RBS setup

- Dr. Kilian Lenz for giving me an introduction in FMR and opportunity to use the FMR set up
- Dr. Roman Boettger for the ion irradiation
- Dr. Attila Kakay and Julia Osten for useful discussion and having funny time in our office
- Thomas Marzi for support and help during FMR measurement
- Yuriy Aleksandrov for FMR measurements
- Yu tian Wang, Oguz Yildirim and Soma Salamon for magnetometry
- Dr. Alina Maria Deac for networking and support
- Dr. Florian M. Römer for frequency dependency FMR measurements
- Manuel Langer, Ewa Kowalska, Thu Trang Trinh and Daniel Blaschke who have been great fiends

In addition, I would like to thank all members of the FWIN division for the nice outdoor activity that have been organized.

At last, I would like to express a sense of gratitude and love to my wife and my parents for their endless love to me and their support to my doctoral study in Germany.

Erklärung

Hiermit versichere ich, dass ich die vorliegende Arbeit mit dem Titel "Study of the Static and Dynamic Magnetization across the First Order Phase Transition in FeRh Thin Films" ohne unzulässige Hilfe Dritter und ohne Benutzung anderer als der angegebenen Hilfsmittel angefertigt habe; die aus fremden Quellen direkt oder indirekt übernommenen Gedanken sind als solche kenntlich gemacht. Die Arbeit wurde bisher weder im Inland noch im Ausland in gleicher oder ähnlicher Form einer anderen Prüfungsbehörde vorgelegt.

Die Dissertation wurde am Helmholtz-Zentrum Dresden-Rossendorf unter der wissenschaftlichen Betreuung von Prof. Dr. Jürgen Faßbender angefertigt.

Ich erkenne die geltende Fassung der Promotionsordnung der Fakultät Mathematik und Naturwissenschaften an der Technischen Universität Dresden an.

Dresden,

10.11.2015

Alireza Heidarian